

Springer Transactions in Civil
and Environmental Engineering

Padmanabha Vivek
T. G. Sitharam

Granular Materials Under Shock and Blast Loading

 Springer

Springer Transactions in Civil and Environmental Engineering

Editor-in-Chief

T. G. Sitharam, Department of Civil Engineering, Indian Institute of Science,
Bangalore, Karnataka, India

Springer Transactions in Civil and Environmental Engineering (STICEE) publishes the latest developments in Civil and Environmental Engineering. The intent is to cover all the main branches of Civil and Environmental Engineering, both theoretical and applied, including, but not limited to: Structural Mechanics Steel Structures Concrete Structures Reinforced Cement Concrete Civil Engineering Materials Soil Mechanics Ground Improvement Geotechnical Engineering Foundation Engineering Earthquake Engineering Structural Health and Monitoring Water Resources Engineering Engineering Hydrology Solid Waste Engineering Environmental Engineering Wastewater Management Transportation Engineering Sustainable Civil Infrastructure Fluid mechanics Pavement engineering Soil dynamics Rock mechanics Timber engineering Hazardous waste disposal Instrumentation and monitoring Construction management Civil engineering construction Surveying and GIS Strength of Materials (Mechanics of Materials) Environmental geotechnics Concrete engineering timber structures.

Within the scopes of the series are monographs, professional books, graduate and undergraduate textbooks, edited volumes and handbooks devoted to the above subject areas.

More information about this series at <http://www.springer.com/series/13593>

Padmanabha Vivek · T. G. Sitharam

Granular Materials Under Shock and Blast Loading



Springer

المنارة للاستشارات

Padmanabha Vivek
Impact Physics Department
Fraunhofer Institute for High-Speed
Dynamics, Ernst-Mach-Institut (EMI)
Freiburg, Baden Württemberg, Germany

T. G. Sitharam
Department of Civil Engineering
Indian Institute of Science
Bangalore, Karnataka, India

ISSN 2363-7633

ISSN 2363-7641 (electronic)

Springer Transactions in Civil and Environmental Engineering

ISBN 978-981-15-0437-2

ISBN 978-981-15-0438-9 (eBook)

<https://doi.org/10.1007/978-981-15-0438-9>

© Springer Nature Singapore Pte Ltd. 2020

This work is subject to copyright. All rights are reserved by the Publisher, whether the whole or part of the material is concerned, specifically the rights of translation, reprinting, reuse of illustrations, recitation, broadcasting, reproduction on microfilms or in any other physical way, and transmission or information storage and retrieval, electronic adaptation, computer software, or by similar or dissimilar methodology now known or hereafter developed.

The use of general descriptive names, registered names, trademarks, service marks, etc. in this publication does not imply, even in the absence of a specific statement, that such names are exempt from the relevant protective laws and regulations and therefore free for general use.

The publisher, the authors and the editors are safe to assume that the advice and information in this book are believed to be true and accurate at the date of publication. Neither the publisher nor the authors or the editors give a warranty, expressed or implied, with respect to the material contained herein or for any errors or omissions that may have been made. The publisher remains neutral with regard to jurisdictional claims in published maps and institutional affiliations.

This Springer imprint is published by the registered company Springer Nature Singapore Pte Ltd.

The registered company address is: 152 Beach Road, #21-01/04 Gateway East, Singapore 189721, Singapore

المنارة
للإستشارات

Dedicated

*To the most precious person in my life, whom
I haven't met yet...*

To my child in the womb...

—Padmanabha Vivek (2019)

Preface

Granular materials like soil are exposed to extreme loading conditions during explosion, dynamic compaction, earthquake, etc. The extreme loading will generate shock waves, which in turn produce high strain effects on the soils, which results in large deformations. Although sand bags are widely used as a blast mitigating medium in civil and military applications, fundamental mechanism during the impact of shock/blast wave on sand is not well understood. One of the main reasons is that experiments performed using explosives are very tedious and uncontrolled. This book will present some of the significant research works carried out to understand the fundamental dynamic behaviour of granular materials, in particular cohesionless sand, when subjected to shock and blast wave loading. This study proposes to use an impulsive equipment like shock tube for geotechnical problems which involve high strain rate and large deformations. Shock tubes are controlled laboratory equipment which are widely used in the area of impact engineering and aerodynamic research. The contents of the book are mainly divided into three parts based on the type of loading imparted to the granular materials: shock wave loading (step pulse), air-blast loading (Friedlander wave) and buried-blast loading. The dynamic response of the granular material was investigated using advanced diagnostic methods like high-speed photography, digital image correlation, acoustic emission and impulse pendulum measurements. Much effort has been made to study the stress wave propagation in granular medium and its direct consequences on the vibrational response upon air-blast, buried-blast and shock wave impact using triaxial accelerometers and fast-response pressure transducers. The peak pressure attenuation and peak particle velocity inside the granular deposits are represented as a function of scaled blast distance for different blast intensities. Also, a three-dimensional finite element analysis of the blast–granular material interaction is simulated using ABAQUS/Explicit and the results are complemented with the experiments.

This book presents general principles on shock waves and blast waves. Very few literatures are available on high strain rate testing methods for granular materials. The motivation to write this book was to give a detailed procedure and testing methods to understand the behaviour of granular materials under shock loading and

blast loading. This book will be very helpful for early stage researcher in the field of impact engineering. The information regarding the experimental setup used is outlined in detail, which will help the fellow researchers to extend the research further. This book will present a comprehensive review of the available testing methods in a controlled laboratory environment, along with the necessary diagnostic measurements for material characterization. Landmine simulator has been designed and built by the first author for low-to-medium blast intensity. A table-mount small-scale shock tube is used in the simulator. Most of the experimental research works related to blast studies are not in the public domain; this book will help researchers working in the area of blast and impact engineering. Important empirical relationships are derived for influencing parameters (PPV, PPS and K_a in terms of Mach number and scaled blast distance), which will help in the design of Blast Protection systems. Comprehensive experimental results are made available in the book for validating various codes and numerical simulations.

All the experiments presented in this book were performed by the first author as part of his Ph.D. work under the guidance of the second author. The shock tube experiments were performed at Laboratory for Hypersonic and Shock Wave Research (LHSR), Department of Aerospace Engineering, Indian Institute of Science, Bangalore, and the granular material testing and characterization were performed at Soil Mechanics Laboratory, Department of Civil Engineering, Indian Institute of Science, Bangalore. We acknowledge the efforts of colleagues and non-technical staffs in LHSR and Soil Mechanics Laboratory.

We also thank the funding agencies like DST, Government of India, and International Bilateral Cooperation Division, Indo-German (DST-BMBF) Cooperation in Civil Security Research (F. No. IBC/FR6/BMBF/CSR/R-03/2015).

Freiburg, Germany
Guwahati/Bangalore, India

Padmanabha Vivek
T. G. Sitharam

Structure of the Book

The book consists of eight chapters. In Chap. 1, a brief introduction to different types of explosions and the importance of Blast Protection system using granular materials are presented. Chapter 2 is exclusively dedicated to the experimental test facility to study the effects of extreme events in the laboratory, in particular shock tubes. The details of the operation of different type of shock tubes are also mentioned. Chapter 3 gives the details about the diagnostic and measurement techniques used for the laboratory-scale experimental study. Different types of granular materials considered for the study and their physical and engineering properties are presented. The chapter includes the discussions on the initial experiments carried out using the three types of shock tubes: diaphragmless shock tube (DST), vertical shock tube (VST) and table-mount shock tube (TST).

This book is mainly centred on the type of loading the granular material samples (in particular, sand) are subjected to. Hence, based on the type of loading imparted to the targets, the chapters are grouped into three categories: shock loading (Chap. 4), air-blast loading (Chaps. 5 and 6) and buried-blast loading (Chap. 7).

Chapter 4 of the book focuses on generating shock loading on the granular sample like sand and glass beads which are essentially used as a shock mitigating material. Diaphragmless shock tube experiments are performed to evaluate the shock attenuation behaviour of geomaterials (sand and geotextile fabric). The details presented in this chapter are published in Geotextile and Geomembrane (Vivek and Sitharam 2017; <https://doi.org/10.1016/j.geotexmem.2017.01.006>). Chapter 5 deals with experiments involving simulated air-blast wave on the sand deposits. The attenuation and vibrational response for dense and loose sand deposits are analysed in detail. For more details on the experiments and test results, readers can refer to (Vivek and Sitharam 2018; <https://doi.org/10.1016/j.ijimpeng.2018.01.003>). Chapter 6 explores some applications and the possibilities of using dimensional analysis procedure to evaluate the real-scale blast effects on the underground structures like pipelines from shock tube experiments. The scaling procedure employed in the present chapter is published in the International Journal of Physical Modelling in Geotechnics (Vivek and Sitharam 2017; <https://doi.org/10.1680/jphmg.16.00070>). In Chap. 7, buried-blast loading experiments are performed using

table-mount shock tube (TST). The kinematics of the sand ejecta and the impulse transferred to the target are explored in detail. The contents of this chapter are published in the International Journal of Impact Engineering (Vivek and Sitharam 2017; <https://doi.org/10.1016/j.ijimpeng.2017.02.017>). Chapter 8 lists out three major geotechnical applications where shock waves are used.

Contents

1 Introduction to Extreme Loading Conditions: Shock, Blast and Impact	1
1.1 Explosions	1
1.1.1 Blast Environments	3
1.2 Shock Wave and Blast Wave Profile	6
1.3 Blast Protection System	7
References	9
2 Fundamental of Shock Waves and Shock Tube	11
2.1 Introduction	11
2.2 What Are Shock Waves?	13
2.3 Ideal Shock Tube Theory	13
2.4 Shock Tube Workings Principles	16
2.4.1 Modes of Operation	16
References	19
3 Measurement, Diagnostic Techniques and Initial Shock Tube Experiments	21
3.1 Measurement and Instrumentation	21
3.1.1 Measurement Sensors	21
3.1.2 High-Speed Visualization Techniques	24
3.2 Shock Tubes Used for Experimental Investigation	26
3.2.1 Diaphragmless Shock Tube (DST)	27
3.2.2 Vertical Shock Tube (VST)	30
3.2.3 Table-Mount Shock Tube (TST)	33
3.3 Scaling Laws and TNT Equivalence	35
3.4 Natural and Synthetic Granular Materials	38
3.4.1 Coarse Sand	38
3.4.2 Fine Sand	40

3.4.3	Glass Beads	40
3.4.4	Supplementary Materials	40
3.5	Test Bed Preparation	41
3.6	Summary	43
	References	44
4	Attenuation of Shock Wave Through Granular Materials	45
4.1	Introduction	45
4.2	Previous Studies on Shock-Granular Interaction	46
4.3	Experimental Test Program	47
4.4	Attenuation of Shock Wave Due to Presence of Wire Mesh	51
4.5	Attenuation of Shock Wave Through Sand Medium	52
4.6	Shock Wave Interaction with Geotextile Layer	55
4.7	Influence of Geotextile Layer on the Sand Barrier System	57
4.8	Summary	64
	References	65
5	Granular Material Responses to Air-Blast Wave Loading	67
5.1	Introduction	67
5.2	Previous Studies on Air-Blast Impact on Granular Medium	68
5.3	Shock Tube Simulated Air-Blast Experimental Series	70
5.3.1	Test Chamber and Instrumentation	70
5.3.2	Digital Image Correlation (DIC) System	72
5.3.3	Blast Wave Characterization and Experimental Test Program	73
5.4	Air-Blast Wave-Induced Stress Wave	76
5.5	Stress Wave Propagation and Attenuation	79
5.6	Air-Blast Wave-Induced Vibration	83
5.7	Blast Wave-Induced Displacement and Strain Fields	89
5.8	Summary	91
	References	93
6	Response of Embedded Structures in Granular Material to Air-Blast Wave Loading	95
6.1	Introduction	95
6.2	Previous Studies	96
6.3	Experimental Setup	96
6.3.1	Test Chamber and Instrumentation	96
6.3.2	Blast Wave Characterization	97
6.4	Experimental Results	100
6.4.1	Response of Sand Deposits and Buried Pipe	100
6.5	Dimensional Analysis	101
6.6	Numerical Simulation and Discussion	105
6.7	Limitation	108

6.8	Summary	108
	References	108
7	Granular Materials Responses to Buried-Blast Loading	111
7.1	Introduction and Previous Studies	111
7.2	Experimental Setup	113
7.2.1	Test Chamber and Sample Preparation	114
7.2.2	Instrumentation	116
7.2.3	Experimental Program	119
7.3	Experimental Results	119
7.3.1	Pressure–Time History Around Blast-Sand Interaction	119
7.3.2	Sand Ejecta	121
7.3.3	Pressure and Impulse Measurement	125
7.4	Discussion and Limitation	129
7.5	Summary	131
	References	131
8	Role of Shock Waves in Geotechnical Applications	133
8.1	Introduction	133
8.2	Alternative to Hydraulic Fracturing	133
8.2.1	Problems Involved with Hydraulic Fracturing	134
8.2.2	Shock Wave Fracking	134
8.3	Shock-Wave-Assisted Pile Driving	136
8.3.1	Development of Laboratory-Scale Shock-Pile-Driving System	137
8.4	Increasing Yield of a Depleted Borewell	138
8.4.1	Methodology and Preliminary Field Trials	139
8.5	Summary	140
	References	141

About the Authors

Dr. Padmanabha Vivek is currently working as a Postdoctoral Researcher in Impact Physics Department at Fraunhofer Institute for High-Speed Dynamics, Ernst-Mach-Institut (EMI), Freiburg, Germany and Geology Department, University of Freiburg, Germany. He has also worked as a Postdoctoral Research Associate in the Department of Civil Engineering Indian Institute of Science, Bangalore (IISc) after completing his PhD from the same Institute. His research interests include studying the shock response of geomaterials material, fracture and fragmentation of rocks and granular materials, energy geotechnics and impact geomechanics. He is a member of the International Shock Wave Institute (ISWI), International Society for Rock Mechanics (ISRM), International Geosynthetics Society, and the Indian Geotechnical Society (IGS). He holds 1 patent and has authored 11 research publications in reputed journals and conferences.

Prof. T. G. Sitharam is the Director, Indian Institute of Technology Guwahati (on deputation) and Professor of Civil engineering at IITG, Guwahati, Assam, India. Formerly, he was KSIIDC Chair Professor in the area of Energy and Mechanical Sciences and Senior Professor at the Department of Civil Engineering, Indian Institute of Science, Bangalore (IISc). He was the founder Chairman of the Center for Infrastructure, Sustainable Transport and Urban Planning (CiSTUP) at IISc, and is presently the Chairman of the AICTE South Western Zonal Committee, Regional office at Bengaluru. He is presently the President of the Indian Society for Earthquake Technology (ISET). Prof Sitharam is the founder President of the International Association for Coastal Reservoir Research (IACRR). He has been a Visiting Professor at Yamaguchi University, Japan; University of Waterloo, Canada; University of Dalhousie, Halifax, Canada; and ISM Dhanbad, Jharkhand, and was a Research Scientist at the Center for Earth Sciences and Engineering, University of Texas at Austin, Texas, USA until 1994. He is a fellow of many societies and has received many awards to his credit. He has an h-index of 39 and I-10 index of 103 with 4540 citations.

Nomenclatures

d_{50}	Sieve size with 50% by mass passing
C_u	Soil coefficient of uniformity
C_c	Soil coefficient of curvature
e_{max}	Maximum void ratio of sand
e_{min}	Minimum void ratio of sand
RD	Relative density
P_e	Equilibrium pressure
K_a	Coefficient of attenuation
SoD	Stand-off distance
DoB	Depth of burial of pipe/blast
OD	Outer diameter of pipe
ID	Inner diameter of pipe
T	Thickness of pipe
EI	Stiffness of pipe/sand
E_s	Elastic modulus of sand
ρ_s	Dry density of sand
φ	Friction angle of sand
W	Weight of the equivalent TNT
R	Distance of target from the surface explosion
H	Altitude of the explosion in air from ground surface
Z	Scaled distance
I	Positive impulse of blast wave
Ms	Mach number: ratio of object speed to local sound speed in the medium of propagation
P_s	Peak overpressure
P_5	Peak-reflected pressure
P_4	Rupture pressure diaphragm/driver gas pressure
P_2	Incident shock pressure
P_{a1}	Ambient atmosphere/driven gas pressure
t_d	Positive phase duration

b	Decay parameter
λ	Scaling coefficient
δ	Residual deflection of the pipe
ε	Strain experienced by the pipe
I_{max}	Maximum impulse imparted to pendulum

Chapter 1

Introduction to Extreme Loading Conditions: Shock, Blast and Impact



1.1 Explosions

During an explosion, sudden amount of energy gets released that causes a rapid increase in heat and pressure. In this process, chemical energy stored in the explosive is instantaneously converted into kinetic energy, sound energy and thermal energy. When a solid/liquid explosive is detonated (TNT, RDX, PETN, nitro-glycerine, etc.), a detonation wave (detonation velocities range from 1500 to 9000 m/s, pressures range from 10 to 30 GPa and temperatures of about 3000–4000 °C) is formed in the explosive, which rapidly converts the solid/liquid phase of the explosive into high-temperature and high-pressure gaseous products, which are visible as a radiant fireball (Aune 2017; Cormie et al. 2009), as shown in Fig. 1.1. These gaseous products expand rapidly and compress the local surrounding medium (air or water or soil), generating shock waves (Long et al. 2010). The radially expanding pressure waves from the centre of explosion coalesce to form a steep shock front, which travels at supersonic velocity (rate of travel of shock wave is faster than the speed of sound in the same medium). The shock front is the leading element of the shock wave, across which there is an extremely rapid rise in pressure, temperature and density. A shock wave is also observed in various events which involve high pressure and high rate of deformation like earthquake, drilling and blasting, pile driving and dynamic compaction, material forming process, etc.

A shock wave which originates from an air-blast is commonly referred to as blast wave. For an explosion in air, the expanding shock wave excites the gas molecules in the surrounding medium, and the imparted energy is manifested as a strong gas flow called 'blast winds'. The transient blast winds with considerable dynamic pressure follow the leading shock front. The combination of shock front and blast wind constitutes the blast wave and is responsible for most of the damages. The damages generally caused due to the blast wave are known as primary blast effects (Krehl



Fig. 1.1 Detonation of a TNT explosive at the ground surface, shock wave is seen expanding radially ahead of the fireball (photograph credits: Defence Research and Development Canada © Her Majesty the Queen in Right of Canada, as represented by the Minister of National Defence, 2015)

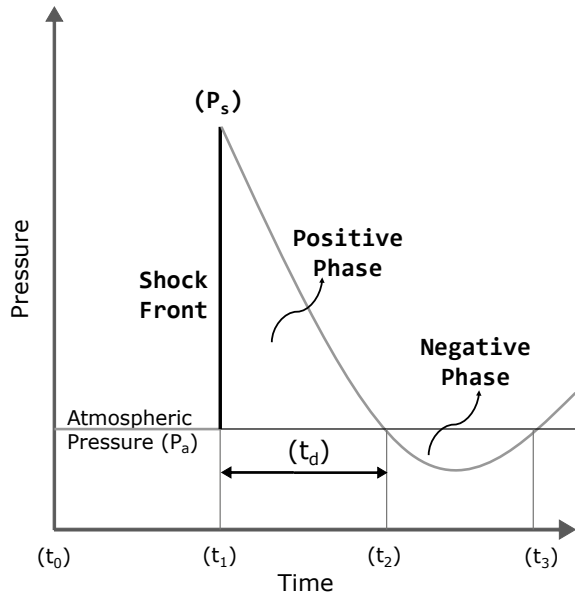
2008). Initially, the blast wave will be travelling at supersonic velocity, as the blast expands the peak pressures of the blast wave diminish with distance and velocity reduces from supersonic to the velocity of sound in the propagating media.

For a free-field explosion, the characteristic shape of a blast wave has been described by Friedlander (1946):

$$P(t) = P_a + P_s \cdot \left(1 - \frac{t}{t_d}\right) \cdot e^{-b \frac{t}{t_d}} \quad (1.1)$$

The typical blast signature for a free-field explosion is shown in Fig. 1.2. The head of the blast wave is called the shock front, and the peak pressure value of the shock front is referred to as peak overpressure (P_s). As the blast wave expands into the atmosphere, the overpressure values decrease exponentially to below atmospheric pressure value and gradually return to ambient pressure levels. The time period between the peak overpressure (t_1) and the instance when the pressure levels start to become negative (t_2) is known as ‘positive phase duration’, t_d . The negative pressure phase is usually small when compared to the positive pressure phase, and most of the damages are incurred because of the positive phase of the blast wave.

Fig. 1.2 Typical blast wave pressure profile for a free-field explosion



1.1.1 Blast Environments

A shock wave originates from an explosion. Depending on the nature of media in which shock wave propagates, the explosions are classified as an air-blast explosion, surface explosion, underground explosion and underwater explosion. The secondary effects of explosion like heat radiation emanating from the fireball will also largely depend on the surrounding media. For an explosive having same mass will have different quantitative and qualitative effects on different media. Hence, the knowledge of the mechanical interaction of the blast wave with the surrounding environment is of vital importance.

The explosion can also be classified depending on the position of the charge with respect to the surface of the earth. Three distinct blast environments are considered, namely air-blast, surface-blast and subsurface or buried-blast. The three blast conditions mentioned are associated with air (atmosphere) or soil (ground surface) or both.

1.1.1.1 Air-Blast

An air-blast is an explosion when an explosive is detonated in air at a sufficient altitude above the ground surface. In the present case, the fireball is expected to dissipate in air before reaching the ground surface. The schematic illustration of the air-blast event taking place during blast wave interaction with the ground surface is shown in Fig. 1.3. The steep-fronted blast wave travelling ahead of the fireball

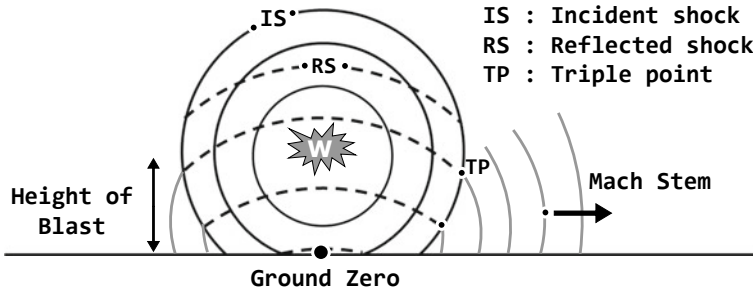


Fig. 1.3 Illustration of an air-blast event

approaches the ground surface in spherical geometry; the spherical blast wave with a peak overpressure impacts the ground surface. The point of contact of the blast wave on the earth surface (target) directly below the explosion is known as ‘ground zero’. The incident blast wave gets reflected into the region which has already been compressed by the incident shock front and strong blast winds. This results in an accelerated ‘reflected shock wave’ with a higher-pressure intensity. The magnitude of the reflected pressure depends on the type and yield of an explosion, strength of incident shock, angle of incident and properties of the earth (target) surface. At ground zero, the angle of incident of shock wave is normal to surface and pressure intensity will be maximum. Upon reflecting from the ground surface, the reflected wave catches up with the incident wave away from the ground zero level, giving rise to a third wave front called ‘Mach stem’ or ‘fused shock’. The point of intersection between incident shock wave, reflected shock wave and Mach stem is known as ‘triple point’. The height of the Mach stem increases as the shock wave propagates and becomes a nearly vertical shock front which sweeps outward on the ground surface.

Targets located at ground zero position will experience both incident and reflected shock wave and will undergo severe damage, and however, this region is highly localized when compared to region covered by Mach stem which spreads over a large distance radially. Mach stem travels horizontally on the surface and damages the buildings which are well below the height of Mach stem. The glass windows and wall panels are shattered and act like shrapnel, which are considered as secondary blast effects. Air-blast explosion is often designated to destroy heavily armed target structures and shatter the ground target over a huge area. The infamous Hiroshima and Nagasaki bombing (1945) involved air-blast nuclear explosion. More recently on 13 April 2017, USA dropped Massive Ordnance Air Blast bomb (BU-43/B-MOAB) on Afghanistan soil (DOD 2017). The non-nuclear air-blast bomb was used to target the bunkers, caves and tunnels used by the terrorist groups. Based on the available information (Howes 2017), the MOAB had an equivalent of 11-tonnes of TNT warhead which was detonated at about 1.8 m above the ground surface. The peak incident and reflected pressure of the shock front at a ground zero surface (point on the earth’s surface right below the point of detonation) are approximately

40.98 MPa and 499.09 MPa, respectively. The above-mentioned blast parameters are estimated from charts of Kingery and Bulmash (1984).

1.1.1.2 Surface-Blast

A surface-blast is an explosion when an explosive is detonated close to or on the ground surface. The shock wave originating from ground explosion immediately interacts with the ground surface and expands into the surrounding atmosphere in hemispherical geometry. In addition, a crater is also formed at source of explosion. In the present case, the fireball directly interacts with the ground surface and the maximum damage incurred will be around the region of ground zero and most of the damages are due to the thermal radiation. The strong winds from the fireball are heavily loaded with debris and sand particles which again cause secondary blast effects. Moreover, shock wave overpressure of the explosion also plays an important role in destruction of the surface targets. Unlike the air-blast, the incident shock wave is reflected and amplified directly by the ground surface to generate a reflected shock wave. A Mach front is also formed at a certain distance from source. Mach front has similar characteristics of the one generated from an air-blast and becomes vertical over large distances. The schematic illustration of the air-blast event taking place during an explosion on the ground surface is shown in Fig. 1.4.

A surface explosion has become very common among the terrorist attacks, which is easier to detonate and cause immediate damages to lives and property. Whereas, for an air-blast detonation, an aircraft is generally employed to carry huge bombs and parachutes are used to discharge the bomb at a specific altitude.

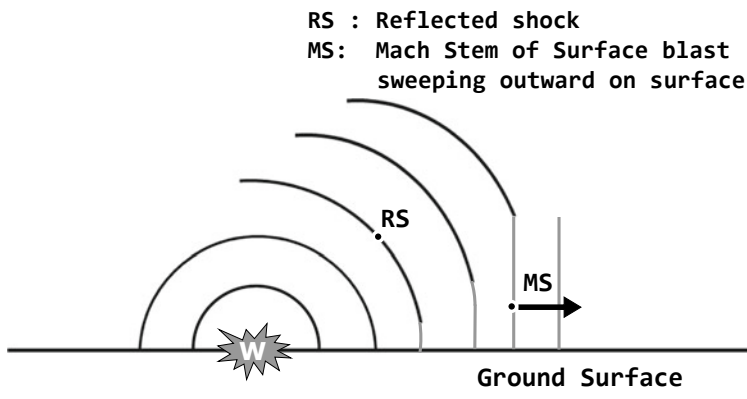
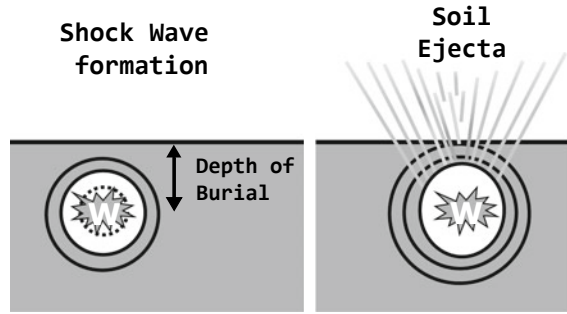


Fig. 1.4 Illustration of a surface-blast event

Fig. 1.5 Illustration of a buried-blast event



1.1.1.3 Buried-Blast

A buried-blast is an explosion when an explosive is detonated beneath the ground surface. The schematic illustration of events taking places during buried-blast explosion is shown in Fig. 1.5. When an explosive that is buried at a shallow depth is detonated, a sphere of high-pressure gases spread rapidly leading to formation of shock waves. The shock wave travels radially outward in all directions and ejects the soil particles out of the surface. This process leads to the formation of a crater on the surface. The impact generated from the sand ejecta is highly localized but are very powerful. When an explosive is detonated at an optimum buried depth, sand ejecta is expected to carry maximum momentum over the surface (Bergeron et al. 1998). Ammunitions like improved explosive device (IED) and landmine were commonly used in warfare, causing a significant threat to lightweight military vehicles and to personal lives onboard (Cheeseman et al. 2006). Buried-blast is generally categorised into two types, namely anti-personnel mines and anti-tank mines. Anti-personnel mines are a smaller size, and they are triggered when the victim steps on them. Compared to anti-personnel mines, anti-tank mines require larger pressure for detonation and the damage intensity is large. During the past several years, it has also become popular among terrorist's groups to bury an explosive device few centimetres below the ground surface and cause fatalities of considerable proportion.

1.2 Shock Wave and Blast Wave Profile

The basic difference between the shock wave and blast wave loading lies in the shape of the pressure profile. Figure 1.6 shows the distinction in the pressure–time profile of a shock wave and a blast wave. A shock wave is characterized by the presence of a sudden jump in the pressure amplitude and the pressure remains constant for a while, this constant zone is called as plateau region. A shock wave pressure profile can also appear in the medium when an object impacts against another at high velocity. A blast wave is a term generally used for the shock waves which are formed due to a free-field air explosion. However, the term ‘blast wave loading’ is generally used

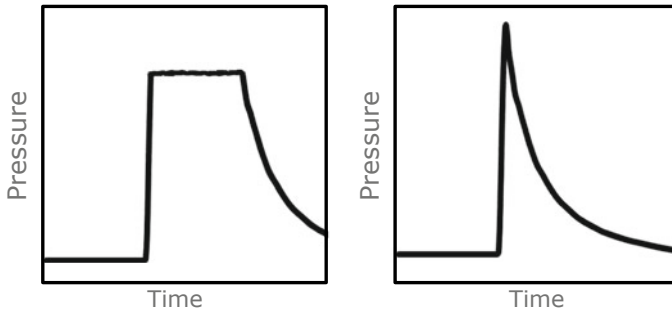


Fig. 1.6 Pressure–time profile of **a** shock wave and **b** blast wave

whenever a pressure profile similar to air-blast wave is obtained. In a blast wave, the sudden jump in pressure is immediately followed by an expansion wave where the pressure decreases exponentially. Blast wave is commonly seen during explosion event.

1.3 Blast Protection System

The threats from blast loadings are significant worldwide and cause devastating property damages and loss of lives. The potential targets include military facilities and defence personnel, and with the increasing terrorist activity, several governmental agencies and civilian structures are also targeted aiming at inflicting maximum economic damage and loss of innocent lives (Krauthammer 2008). Therefore, there is a need for development of efficient Blast Protection systems. A blast resistant system must be designed to prevent catastrophic failure of structures and to protect personnel lives from the blast effects. Blast protective barriers and protected spaces are widely used in military applications to provide shelter to the occupants and protect the control system against the effects of an external explosion.

Initially, structural steel and reinforced concrete structures were commonly used as protective structures against explosion. Although these structures have high tolerance in mitigating the blast, upon extreme blast loads, the structures collapse leading to generation of debris particles and sharp fragments (secondary blast effects). Concrete and steel structures are efficient material in blast protection, and however, these structures are mostly permanent and involve considerable time and labour for the construction. Later, a more rational approach was carried out by researchers in selecting appropriate mitigating materials for the blast protective structures. The materials presented include soft condensed matter (like granular materials and foams), heavy metals and alloys (ferrous alloys, aluminium alloys and titanium), lightweight composite and polymers (fibreglass, nylon fabrics) and ceramics (alumina, boron carbide, silicon carbide). Choosing a material that is effective under different blast environment and ballistic loading is a significant challenge.

The granular geomaterial (in particular sand) is one of the oldest and most common materials used till date as a blast protective medium. Sand bags are used for over a century as protective barrier walls in civil and military applications. A photograph of the sand bags used in front of the US government building is shown in Fig. 1.7a. The function of the sand bag is to act as a temporary fortification against blast/shock wave and projectile (bullet/fragments) impact. Further, sand particles are considered as promising granular mitigating material because of the low density and their inherent ability to absorb energy. The modern protective barriers used in the fields are improvised version of the sand bags. One such commercially available product which has found extensive use in military application is HESCO® Bastion concertainer wall barriers. The concertainer barriers are cubical baskets made of stainless-steel wire mesh lined with geotextile, and they form a protective barrier system upon filling with locally available granular material like sand and gravels (Scherbatiuk and Rattanawangcharoen 2008). A schematic illustration of the HESCO® units is shown in Fig. 1.7b. Geotextile contained sand barriers are prefabricated type of protective structures which are lightweight, cost-effective, easy to set up and easily mobilizable to different site conditions, thereby reducing the load carried by the military personals. Moreover, these barriers do not undergo brittle failure like concrete walls upon blast impact (Ng et al. 2000).

Sand is a naturally occurring porous granular material which is abundantly available (making it cost-effective) and by itself is a very good shock absorbent material. The different applications where sand is used as blast protective medium are illustrated in Fig. 1.8.

The sand particles can either act as an effective blast mitigating medium or can also induce damages. The role of the sand media depends on the type of loading it is subjected to. For instance, locally available sands are filled into bags (or HESCO®

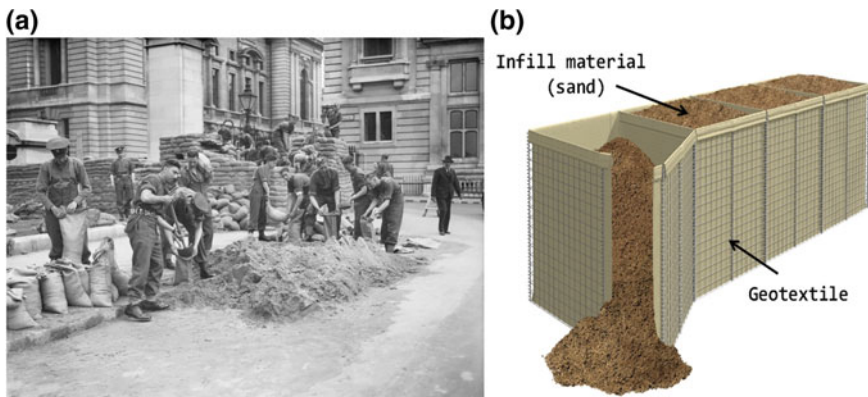


Fig. 1.7 Sand bags used as blast protective barrier walls: **a** sand bags defence wall were being constructed by the troops in London against possible air strikes in London, 1940 (photograph courtesy: Imperial War Museum); **b** an illustrative figure of HESCO Bastion concertainer wall units

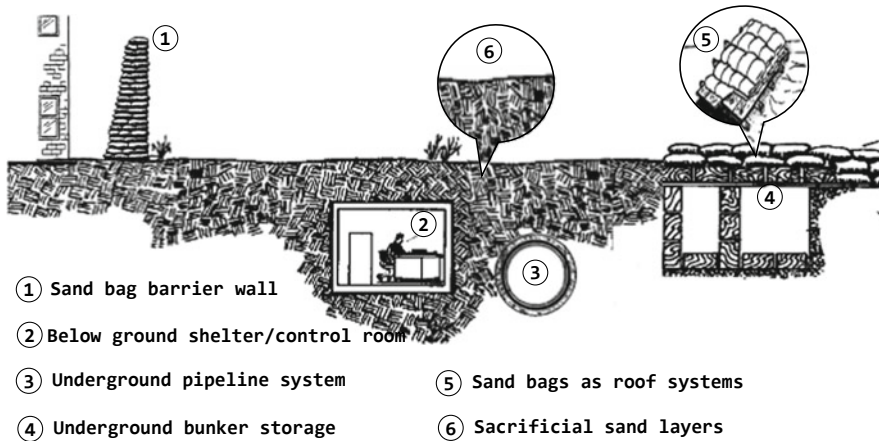


Fig. 1.8 Illustration showing different target structures, where sand particles are used as a blast protective medium (Inspired from FM-3-4 1992)

units) and are stacked one above the other, which forms a temporary barrier wall against direct shock waves or Mach stem originating from the air/surface-blast. Protected underground spaces are bunker like structures, which are often used as control rooms, storage units for munitions and explosives and also house important military equipment's (radars, etc.) used for communication purpose. The surface or underground bunkers are often constructed using sand bags, where cut timber and scrap materials are used to support the sand bags which are used as roofing systems. Some important bunker units are buried deep under the ground surface, and the overburden soil above the bunker units acts as sacrificial layers in attenuating the incoming blast waves. A similar condition can be observed with respect to the underground tunnels and pipeline systems, which are buried at a specific depth such that it is least influenced by the surface explosions. Sand particles can also be detrimental, for instance, during buried-blast loading like landmine, the sand fragments originating from the sand ejecta impact the surface targets and cause catastrophic damages.

References

- Aune V (2017) Behaviour and modelling of flexible structures subjected to blast loading. Ph.D. thesis, Norges Teknisk-Naturvitenskapelige Universitet (NTNU), Norway
- Bergeron DM, Walker R, Coffey C (1998) Detonation of 100-gram anti-personnel mine surrogate charges in sand—a test case for computer code validation. Ralston, Alberta
- Cheeseman BA, Wolf S, Yen CF, Skaggs R (2006) Blast simulation of explosives buried in saturated sand. *Fragblast* 10(1–2):1–8
- Cormie D, Mays G, Smith PD (2009) Blast effects on buildings. Thomas Telford Ltd., London

- DOD (2017) U.S. Bombs, Destroys Khorasan Group Stronghold in Afghanistan. United States of America, Department of Defence, <https://www.defense.gov/News/Article/Article/1151139/us-bombs-destroys-khorasan-group-stronghold-in-afghanistan/>
- FM-3-4 (1992) NBC protection, Department of the Army, Headquarters, Washington, DC. <https://www.globalsecurity.org/wmd/library/policy/army/fm/3-4/index.html>
- Friedlander F (1946) The diffraction of sound pulses. I. Diffraction by a semi-infinite plane. Proc R Soc A Math Phys Eng Sci 186(1006)
- Hesco (2010) HESCO Bastion concertainers. <http://www.hesco.com/>
- Howes S (2017) What is MOAB? 'Mother of All Bombs' GBU-43/B dropped on ISIS is 11-tonnes of pure TNT. Daily Mirror Online, <http://www.mirror.co.uk/news/politics/what-moab-mother-bombs-gbu-10221849>
- Kingery CC, Bulmash G (1984) Air blast parameters from TNT spherical air burst and hemispherical surface burst. Defence technical information center, Ballistic Research Laboratory, Aberdeen proving ground, Maryland, USA, Report BRL, 02555
- Krauthammer T (2008) Modern protective structures. CRC Press, Taylor & Francis Group, Florida
- Krehl P (2008) History of shock waves, explosions and impact: a chronological and biographical reference. Springer, Berlin
- Long J, Tong L, Bauman R, Atkins J (2010) Blast-induced traumatic brain injury: using a shock tube to recreate a battlefield injury in the laboratory. In: 26th southern biomedical engineering conference SBEC, Maryland USA, pp 26–30
- Ng CC, Chew SH, Karunaratne GP, Tan SA, Loh SL (2000) Flexible and rigid faced MSE walls subject to blasting. In: Advances in transportation and geoenvironmental systems using geosynthetics. American Society of Civil Engineers, Reston, pp 322–336
- Scherbatiuk K, Rattanawangcharoen N (2008) Experimental testing and numerical modeling of soil-filled concertainer walls. Eng Struct 30(12):3545–3554

Chapter 2

Fundamental of Shock Waves and Shock Tube



2.1 Introduction

Several empirical and numerical methods are available to understand the behaviour of granular materials under impulse and blast loading. Experimental method is the most reliable testing procedure to understand the dynamic response of granular materials during various blast events since it represents the actual physics of the problem. The most ideal testing methods involve full-scale field testing using explosive charges. However, a full-scale field blast testing is expensive and involves high risk. The full-scale blast testing has several drawbacks (Sundaramurthy and Chandra 2014):

- i. Experimental procedure is tedious and is highly unsafe.
- ii. The experiments are uncontrolled, and repeatability of the experiments is difficult to achieve.
- iii. The fireball and debris obscure the test phenomenon to be visualized.
- iv. The blast testing using explosives often damages the sensors mounted on the specimen.

However, complete elimination of the full-scale field blast testing using explosive is not possible. Nevertheless, by using advanced laboratory-scale blast simulator, the required number of field experiments can be minimized, and more controlled and safe experiments can be carried out. Various alternative testing methods are available for studying the responses of granular materials under shock and blast loading conditions.

Scaled explosive testing, blast pendulum, hydraulic blast simulator, split-Hopkinson bar, gas gun and shock tube are some of the experimental facilities which are widely used to simulate the shock and blast loading. Each of these techniques has its own advantages and disadvantages. Scaled explosive charge testing method recreates the blast explosion in the laboratory scale. The explosive weights and corresponding blast waves are appropriately scaled using scaling law (discussed in detail in the next section). As mentioned earlier, it has disadvantages with respect to

repeatability and visibility issues during testing. Hydraulic actuated blast simulator (Stewart et al. 2014) is an explosive-free laboratory method to simulate blast loading. Explosion pressure levels are precisely replicated in a laboratory using hydraulic actuators. The blast simulator is considered to be very expensive. Split-Hopkinson pressure bar (SHPB), developed by Kolsky (1949), has been used widely to study material at high strain rates (Zhang et al. 2009). The blast simulator and SHPB impart the high-pressure loading by sudden release of flanges (or striker bar), and the flanges accumulate maximum momentum and deliver to test samples through contact. Blast simulator generates the blast wave pressure profile on the sample, while SHPB is used only to get high strain rate data of the materials. Both the methods do not account for the gas dynamics phenomenon associated with the blast loading, for example, dynamic pressure winds which are developed on passage of blast wave in air. Gas gun is a laboratory tool which is used to study the impact dynamics of materials. The projectile (resembling bullet) is propelled using a gun barrel which is powered by chemical reaction usually generated by gunpowder (Crozier and Hume 1957). The gas gun is modified to generate shock wave pressure profile by using a flyer plate. The accelerated flyer plate impacts the sample and thereby imparting shock wave loading over the entire sample surface. The characteristic features of a shock wave and blast wave are also generated by using a shock tube. High-pressure compressed gas is released suddenly to generate shock waves. Shock tube is a low-cost tool which can also generate blast wave under controlled laboratory conditions without the use of explosives. Moreover, among the mentioned blast simulators, shock tube alone facilitates the direct interaction of gas with the sample (as observed in an actual blast). Hence, the experiments performed using shock tube can account for both gas dynamic and solid mechanics aspects involved during a blast event. The advantages of shock tube are listed below.

- (i) Shock tube tool is relatively simple in operation and is inexpensive when compared to full field blast experiments.
- (ii) Field experiments performed with explosives are unsafe and are highly prone to accidents. Shock tube offers a safe working environment.
- (iii) Shock tube experiments are performed in a controlled laboratory environment with wide range of instrumentation and advanced diagnostic measurements. Data measurements in field experiments are a tedious process, and often, the sensors are damaged due to impact of the debris.
- (iv) Excellent repeatability conditions can be achieved using shock tube.

However, limitations of this non-explosive method are restricted to smaller size sample, and it is highly challenging to produce high-level peak overpressure values in shock tubes (Whisler and Kim 2014). It is difficult to obtain blast parameters similar to field explosion, and it is a common practice to use scaling laws to simulate blast events of large magnitude.

This book emphasizes on the experiments related to shock tube. The dynamic response of granular materials against shock and blast loading is investigated using a compressed-gas-driven shock tube. Before looking into the shock tube experiments, it is helpful to review the basic concepts of shock waves and theory involved in the shock tube.

2.2 What Are Shock Waves?

Shock waves are nonlinear waves, which can be formed in gaseous, liquid and solid medium. Shock wave appears in the nature whenever the elements in a medium approach one another at a velocity higher than the speed of the sound in the same medium. A classic example is when a bullet is fired, or an explosion, during which sudden amount of energy gets released over a short duration. A shock wave can be visualized as a thin region of disturbance propagating at supersonic speed (Mach no., M_s greater than 1; Mach no. is defined as the ratio of object speed to local sound speed in the medium of propagation) across which sudden change in fluid flow properties like pressure, density and temperature takes place.

Shock wave associated phenomena are often studied using shock tubes, and it is considered to be most reliable tool to generate shock waves in the laboratory. The shock tubes are most widely used in aerospace engineering for investigating high-speed flow field around ballistic missiles and re-entry space vehicles (Balakalyani and Jagadeesh 2019; Davis and Curchack 1969; Ibrahim et al. 2016). The advantages of shock tubes over explosive testing equipment are: (i) it is a non-explosive method; hence, it offers a safe working environment, (ii) excellent repeatability can be obtained, (iii) experiments are controlled, and (iv) it involves simple operation and is considered to be cost-effective when compared to full field blast experiments.

The shock tube is also one of the few laboratory tools which are capable of reproducing the pressure conditions involved during blast or impact event. Shock tubes are often considered as an alternative to explosive testing methods and have many advantages over conventional explosive testing. However, shock tube does have some disadvantages. The pressures level which shock tubes can be operated is limited. Moreover, shock tube does not recreate the radiation and thermal effects involved during an explosion and further fail to deliver secondary effects like debris/shrapnel impacts.

2.3 Ideal Shock Tube Theory

The discussion on shock tube theory is limited to compressed-gas-driven-type shock tube having a circular cross section. The relationship between the thermodynamic properties on both sides of the shock front is given by the Rankine–Hugoniot relations (also known as the jump conditions). One-dimensional theoretical analysis is considered for the shock tube problem; the flow is considered inviscid and obeys ideal gas equation with constant specific heat. The governing equations representing the conservation of mass, momentum and energy are given by Eqs. (2.1), (2.2) and (2.3) (Anderson 2003):

$$\rho_2 v_2 = \rho_1 v_1 \quad (2.1)$$

$$P_2 + \rho_2 v_2^2 = P_1 + \rho_1 v_1^2 \quad (2.2)$$

$$\frac{P_2}{\rho_2} + e_2 + \frac{1}{2}v_2^2 = \frac{P_1}{\rho_1} + e_1 + \frac{1}{2}v_1^2 \quad (2.3)$$

where P , ρ , v and e represent pressure, density, velocity and internal energy, respectively. Ideal gas equation ($Pv = \rho RT$) is substituted in the conservation equation and appropriately rearranging them, we get:

$$\frac{T_2}{T_1} = \frac{P_2}{P_1} \left(\frac{\frac{\gamma+1}{\gamma-1} + \frac{P_2}{P_1}}{1 + \frac{\gamma+1}{\gamma-1} \frac{P_2}{P_1}} \right) \quad (2.4)$$

$$\frac{\rho_2}{\rho_1} = \left(\frac{\frac{\gamma-1}{\gamma+1} + \frac{P_2}{P_1}}{\left[\frac{\gamma-1}{\gamma+1} \right] \frac{P_2}{P_1} + 1} \right) \quad (2.5)$$

The above equations are referred to as Rankine–Hugoniot equations (Anderson 2003). It is also convenient to represent pressure ratio across the shock wave in terms of Mach number, as given below.

$$\frac{P_2}{P_1} = 1 + \frac{2\gamma}{\gamma+1} (M_s^2 - 1) \quad (2.6)$$

In the case of shock tube, properties of driver gas and driven gas are known. However, the properties of gas in region 2, 3 are unknown (refer Fig. 2.1). With the known properties of the driver and driven gas (ratio of specific heat γ_4 and γ_1), the Mach number (M_s) is obtained using the below relation (Gaydon and Hurler 1963).

$$\frac{P_4}{P_1} = \frac{\gamma_1 - 1}{\gamma_1 + 1} \left[\frac{2\gamma_1}{\gamma_1 - 1} M_s^2 - 1 \right] \left[1 + \frac{\gamma_4 - 1}{\gamma_4 + 1} \left(\frac{a_1}{a_4} \right) \left(M_s - \frac{1}{M_s} \right) \right]^{-\frac{2\gamma_4}{\gamma_4 - 1}} \quad (2.7)$$

where a_4 is the speed of sound in driver gas, and a_1 is the sound speed in driven gas. With the calculated Mach number from Eq. (2.7), the pressure ratio across the shock wave is predicted using the shock relations mentioned in Eq. (2.5). The reflected shock wave Mach number (M_R) is determined from the incident shock wave Mach number (M_s) using the below equation.

$$\frac{M_R}{M_s^2 - 1} = \frac{M_s}{M_s^2 - 1} \sqrt{1 + \frac{2(\gamma_1 - 1)}{(\gamma_1 + 1)^2} (M_s^2 - 1) \left(\gamma_1 + \frac{1}{M_s^2} \right)} \quad (2.8)$$

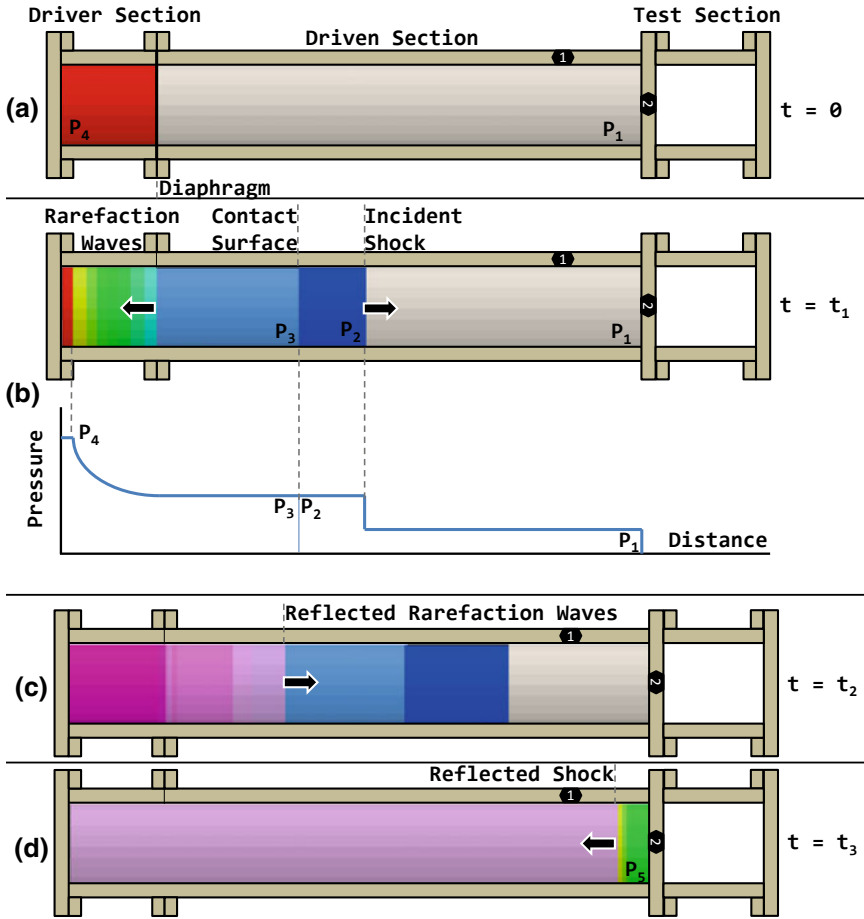


Fig. 2.1 Schematic representation of various events occurring inside the shock tube: **a** initial conditions before rupturing the diaphragm; **b** different wave fronts appear immediately after the diaphragm rupture (distribution of pressure along the shock tube is also shown); **c** reflected rarefaction waves travelling into the driven section; and **d** shock wave after reaching the end of the driven section

The peak-reflected shock wave pressure (P_5) at the end wall of the shock tube is related to the reflected shock wave Mach number (M_R) using the following equation,

$$\frac{P_5}{P_2} = 1 + \frac{2\gamma_1}{\gamma_1 + 1} (M_R^2 - 1) \tag{2.9}$$

2.4 Shock Tube Workings Principles

The shock tube essentially consists of two main components: driver (high pressure) and driven (low pressure) sections, which are separated by a diaphragm. The high-pressure gas (nitrogen or helium is commonly used) is used to pressurize the driver section until the diaphragm ruptures while maintaining the driven section at low pressure. Qualitative pictures of the events happening inside the shock tube at different time intervals are shown in Fig. 2.1.

At time $t = 0$ (Fig. 2.1a), the diaphragm ruptures leading to a sudden release of the high-pressure driver gas (P_4) into the low-pressure gas (P_1) section, a series of compression waves, propagate into the driven section. On the way of travel, compression waves compress the driven gas and raise its temperature. At time $t = t_1$ (Fig. 2.1b), the rear compression pressure waves at region of high-temperature zone travel faster than leading pressure waves, and these compression waves eventually coalesce to form an incident shock wave at a certain distance away from the diaphragm section. The generated shock wave will be travelling at velocity higher than the velocity of sound of the driven gas. The driver gas and driven gas come in contact at the contact surface, which travels right behind the shock wave. The pressure region between contact surface and shock wave is denoted as P_2 . Subsequently, an expansion wave travels in the reverse direction of shock wave (Fig. 2.1b) into the driver section. The expansion wave travels at the speed of sound in the driver gas, and the pressure drop is gradual unlike the shock waves (see pressure–distance curve in Fig. 2.1b). The region between contact surface and the expansion wave is denoted as P_3 . The expansion wave is also called as rarefaction fan with the leading wave referred as ‘head’ and the last wave as the ‘tail’. The rarefaction head upon reaching the end of the driver section gets reflected to interact with the incoming expansion fan (tail), and this overlap further accelerates the reflected rarefaction fan (Gaydon and Hurlé 1963). The reflected rarefaction wave travels towards the contact surface (Fig. 2.1c). Finally, at $t = t_4$, the incident shock wave undergoes reflection at the end of the driven section (Fig. 2.1d), and there is further rise in pressure P_5 .

2.4.1 Modes of Operation

The shock tube can essentially be operated in both shock wave mode and blast wave mode. The basic difference between a shock wave and blast wave lies in the pressure zone behind the shock front. A typical shock wave profile is characterized by the presence of shock front (sudden jump), followed by the contact surface pressure which remains constant for a certain period. While in the case of a blast wave, the sudden jump in pressure is immediately followed by an expansion wave where the pressure decreases exponentially. The type of wave generated in a shock tube depends on the following parameters:

- (i) Length of the driver section.
- (ii) Nature of the driver gas.

The role of the above-mentioned parameters in the formation of shock wave/blast wave is explained with the help of the wave diagram shown in Figs. 2.2 and 2.3.

In order to generate a shock wave, a rapid driving force is required. In the shock tube, the sudden release of driver gas initiates the formation of shock wave, as discussed in Sect. 2.4. Figure 2.2 illustrates the wave diagram of different wave fronts for shock wave mode of operation. The idealized pressure profile obtained during a shock wave mode is also shown in Fig. 2.2, location 1 corresponds to side wall of the shock tube and location 2 is on the end wall of driven section. From the wave diagram, it can be seen that the reflected rarefaction head has failed to catch the incident shock front, and the constant pressure behind the shock front is limited

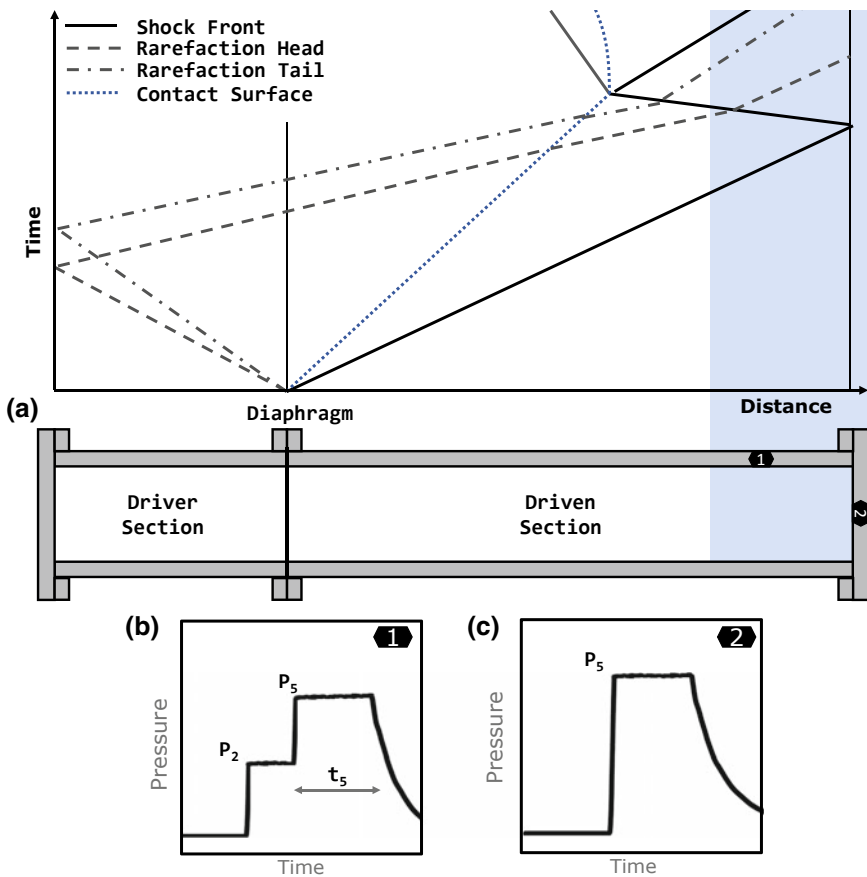


Fig. 2.2 Shock wave mode of operation: **a** an illustration showing different wave fronts in the $x-t$ space of a shock tube; **b** typical shock wave pressure profile at location 1; and **c** typical shock wave pressure profile at location 2

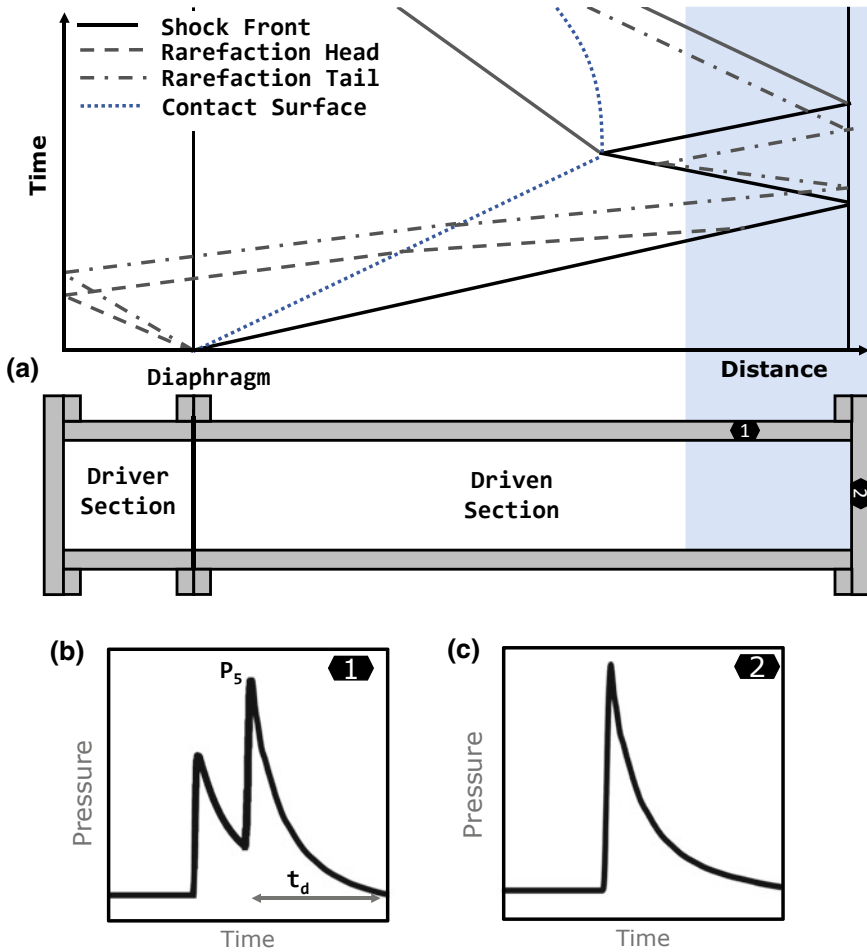


Fig. 2.3 Blast wave mode of operation: **a** an illustration showing different wave fronts in the $x-t$ space of a shock tube; **b** typical shock wave pressure profile at location 1; and **c** typical shock wave pressure profile at location 2

primarily by the arrival of the rarefaction wave (see Fig. 2.2b). The rarefaction wave eventually catches up with the reflected shock front (P_5) by overtaking the contact surface and decays the pressure level (Fig. 2.2c). The constant pressure duration (t_5) can be achieved by providing sufficient driver length with driver gas having lower sound speed (e.g. nitrogen), to delay the arrival time of the contact surface (or rarefaction wave). The reflected shock wave pressure (P_5) over a constant time duration (t_5) is used as input loading pulse in investigating the target against shock loading.

Figure 2.3 illustrates the wave diagram for the blast wave mode of operation. It is emphasized in the shock wave mode that the arrival of the rarefaction plays a major

role in decaying the pressure levels. In order to obtain an immediate pressure decay profile, the rarefaction waves have to be accelerated. This can be achieved by choosing a driver gas which has a higher sound speed (e.g. helium), and hence, the rarefaction wave is expected to travel faster in the driver section. The reflected rarefaction wave from the driver section further accelerates when it crosses the contact surface due to the increased sound speed and eventually decays the incident shock pressure. In addition, the length of driver section can also be reduced (considering enough driving force for shock front formation) so that time taken for the travel of rarefaction wave in driver section is reduced. The decay in the pressure profile at location 1 (Fig. 2.3b) indicates that rarefaction head has caught up with the leading shock front and at location 2 (Fig. 2.3c), and the reflected shock pressure is exponentially decreased by the series of expansion fan. The reflected shock wave pressure (P_3) over positive time duration (t_d) is used as input blast pulse in investigating the target against blast loading.

References

- Anderson JD (2003) *Modern compressible flow: with historical perspective*. McGraw-Hill
- Balakalyani G, Jagadeesh G (2019) An accelerometer balance for aerodynamic force measurements over Hypervelocity Ballistic models in shock tunnel. *Measurement* 136:636–646
- Crozier WD, Hume W (1957) High-velocity, light-gas gun. *J Appl Phys Am Inst Phys* 28(8):892–894
- Davis HJ, Curchack HD (1969) *Shock tube techniques and instrumentation*. Technical Report TR-1429, Defense Technical Information Center, Fort Belvoir, VA, USA
- Gaydon AG, Hurlle IR (1963) *The shock tube in high-temperature chemical physics*. Chapman and Hall Ltd., London
- Ibrahim SM, Vivek P, Reddy KPJ (2016) Experimental investigation on transpiration cooling effectiveness for spacecraft entering martian atmosphere. *AIAA J* 54(9):2922–2926
- Kolsky H (1949) An investigation of the mechanical properties of materials at very high rates of loading. *Proc Phys Soc Sect B* 62(11):676–700
- Stewart LK, Durant B, Wolfson J, Hegemier GA (2014) Experimentally generated high-g shock loads using Hydraulic Blast Simulator. *Int J Impact Eng* 69:86–94
- Sundaramurthy A, Chandra N (2014) A parametric approach to shape field-relevant blast wave profiles in compressed-gas driven shock tube. *Front Neurol* 5:253
- Whisler D, Kim H (2014) A non-explosive test method for generating wide area dynamic blast-type pressure pulse loading on armored panels. *Int J Impact Eng* 68:28–40
- Zhang M, Wu HJ, Li QM, Huang FL (2009) Further investigation on the dynamic compressive strength enhancement of concrete-like materials based on split Hopkinson pressure bar tests. Part I: experiments. *Int J Impact Eng* 36(12):1327–1334

Chapter 3

Measurement, Diagnostic Techniques and Initial Shock Tube Experiments



3.1 Measurement and Instrumentation

The shock waves are associated with extremely high velocities and pressures, and it is hence necessary to have an appropriate system that includes fast-response measurement devices. This section will be devoted to the discussion of various instruments used in the experimental setup.

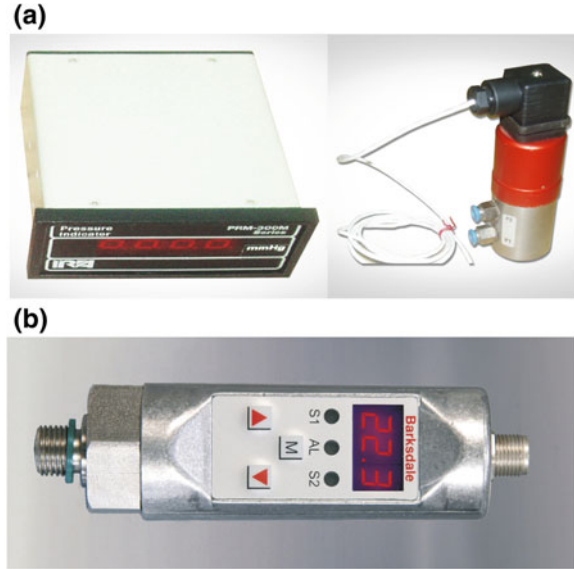
3.1.1 Measurement Sensors

3.1.1.1 Pressure Sensors

The high-pressure gas in the driver section is monitored through digital pressure gauges. Two different types of pressure gauges are used. The IRA digital pressure gauge (model PRM-300M) enables the measurement and display of pressure values in the range of 0–200 bar with a least count of 1 bar. While, Barksdale pressure switch SW2000 (Barksdale Control Products, Reichelsheim, Germany) is used for pressure values in the range of 0–50 bar with a least count of 0.1 bar. The photograph of the digital pressure gauges is shown in Fig. 3.1.

Piezoelectric pressure transducers have gained wide acceptance in shock wave pressure measurements. The pressure transducers are generally mounted at the end of the driven section and are flush mounted onto the inner surface of the shock tube. The pressure profiles and the velocity (and Mach No.) of shock wave are determined from the two (at least) transducers mounted on the shock tube. The piezoelectric-type pressure transducers are also embedded in the sand deposits, which are used to measure dynamic pressure/principal stresses developed during shock impact. Different series of PCB (Piezotronics Inc., USA) pressure transducers of varying pressure

Fig. 3.1 Digital pressure gauge: **a** IRA Pvt. Ltd.; **b** Barksdale Inc.



ranges are used in the experimental study shown later in subsequent chapters. PCB 112A22 series has a measurement range up to 50 psi ($1 \text{ psi} = 6894.75 \text{ N/m}^2$) with a sensitivity of 100 mV/psi; PCB 113B24 and PCB 113B22 series displays pressure with the range of 0–1000 psi (sensitivity of 5.0 mV/psi) and 0–5000 psi (sensitivity of 1.0 mV/psi), respectively; PCB 113B23 series has a measurement range up to 10,000 psi with a sensitivity of 0.5 mV/psi. The rise time of these transducers is about 1 μs . A photograph of PCB model 113B23 is shown in Fig. 3.2a.

3.1.1.2 Accelerometers

The physical movements of granular particles upon shock/blast interaction are analysed using accelerometers. The movements comprise of acceleration in various directions and can also vary in frequency and intensity. Hence, two types of accelerometers are used in the experiments, uniaxial accelerometer (UA) and triaxial accelerometer (TA). Both uniaxial (M353B17) and triaxial accelerometer (PCB356B11) are of piezocrystal (Quartz type) resistive transducers manufactured by PCB Piezotronics Inc., USA. Uniaxial accelerometer has frequency range of ($\pm 5\%$) 1–10,000 Hz with a sensitivity of 10 mV/g. The triaxial accelerometer (TA) is composed of three uniaxial piezoresistive accelerometers mounted orthogonal to each other. The TA is miniature-type accelerometer weighing approximately 4 gm; it has frequency range of ($\pm 5\%$) 2–10,000 Hz with a sensitivity of 10 mV/g. A photograph of uniaxial and triaxial accelerometers is shown in Fig. 3.2b, c, respectively.

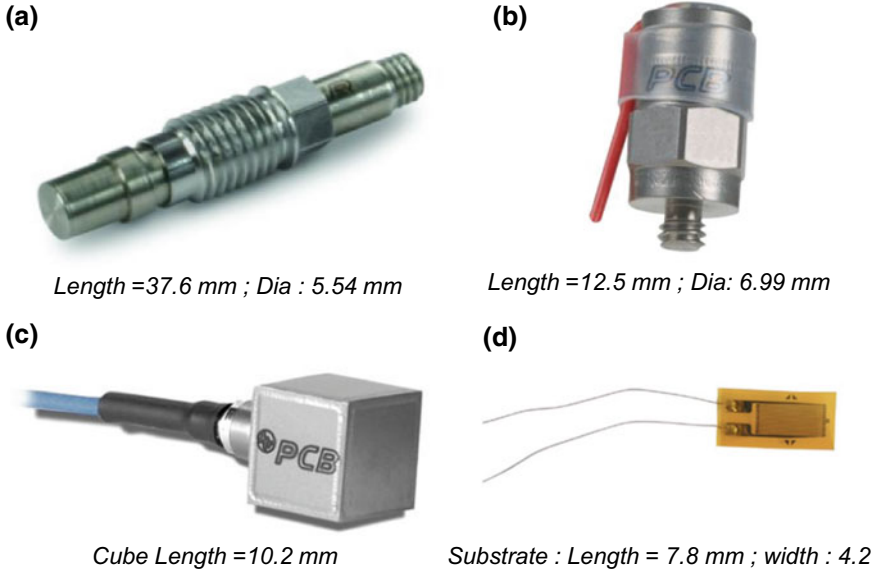


Fig. 3.2 Dynamic measurement sensors: **a** PCB piezoelectric pressure transducers; **b** PCB uniaxial accelerometer; **c** PCB triaxial accelerometer; **d** strain gauge

3.1.1.3 Strain Gauges

The strain gauges are used to measure the deformation of the test model pipe, made of aluminium. The model surface is polished using a fine sandpaper, and the target surface is cleaned using acetone solvent. A 350 Ω foil strain gauge (M/s IPA Pvt. Ltd., Bangalore, India) is bonded on the prepared model surface using cyanoacrylate adhesive. A strain gauge's conductors are very thin and are connected using a four-wire quarter bridge configuration by using the DAQP-STG module of M/s Dewetron GmbH. The photograph of the strain gauge used in the experiments is shown in Fig. 3.2d.

3.1.1.4 Data Acquisition (DAQ) System

The signals from the PCB pressure transducers and accelerometer signals are passed through a signal conditioner box (Model 482A21) manufactured by PCB Piezotronics Inc. (Fig. 3.3a). The signal conditioner box receives the sensor outputs and converts the output signals in terms of voltage. The output signals are recorded and captured using a DL750 Scopecorder (Yokogawa Electric Corp. Japan). For the strain gauge, a Dewetron signal conditioning rack (M/s Dewetron GmbH, Germany) is used for signal processing (Fig. 3.3b) and the output signals are recorded using Yokogawa's

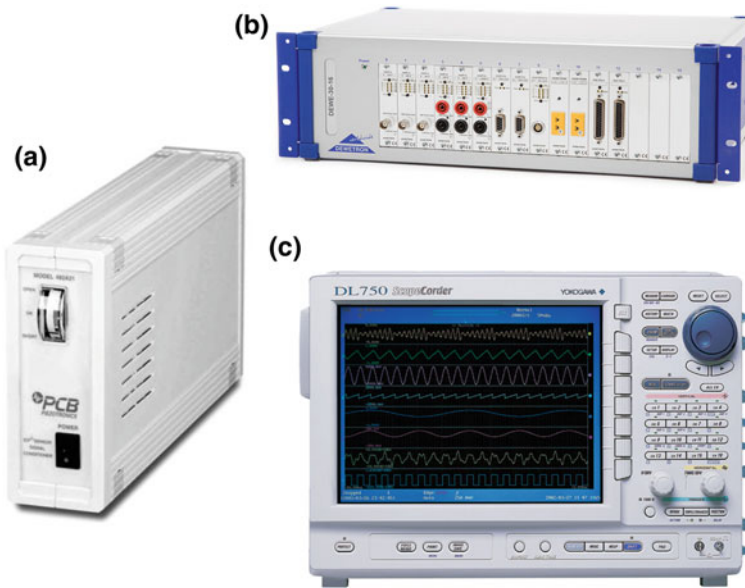


Fig. 3.3 Data acquisition system: **a** PCB signal conditioner for pressure transducers and accelerometers; **b** Dewetron signal conditioner for strain gauge; **c** Yokogawa oscilloscope

ScopeCorder (Fig. 3.3c). In most of the experiments, the signals are captured with a sampling rate of 500 kHz.

3.1.2 High-Speed Visualization Techniques

Qualitative and quantitative information of the events occurring during blast event are captured using high-speed photography. In most of the experiments, the test regions (mostly containing sand particles) are directly captured at a higher frame rate using a high-speed camera. The direct capture system does not need any optical component except a high-powered flashlight source. A typical experimental setup prepared for the direct capture is shown in Fig. 3.4a. The test region of the experimental setup is illuminated with 1000 W halogen lamp. A Phantom V310 high-speed camera (Vision Research[®] Inc., USA) is used in all the visualization experiments (Fig. 3.4c). Generally, a signal from a pressure sensor or accelerometer is used to trigger the high-speed camera via a delay pulse generator (Stanford Research Centre, USA) as shown in Fig. 3.4d. The experiments involving the visualization of shock/blast wave flow field are carried out using shadowgraph and schlieren technique.

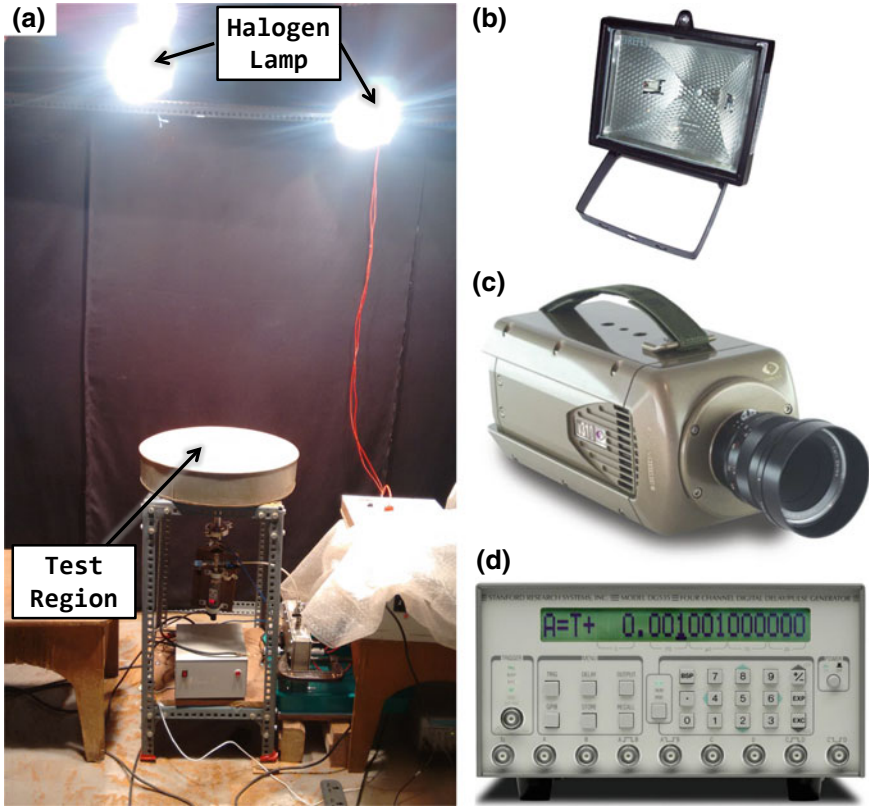


Fig. 3.4 Photograph of an experimental setup prepared for direct capture: **a** fully assembled experimental setup; **b** halogen lamp; **c** high-speed camera; **d** delay pulse generator used to trigger the camera

3.1.2.1 Shadowgraph Technique

Shadowgraph is a type of flow visualization technique which is used to observe the flow of varying density gradation. The density of a fluid varies with temperature and pressure. Shadowgraph technique is used to visualize blast wave (across which temperature and pressure changes abruptly) and also used to measure the expansion rate of the shock front. In principle, when a parallel beam of light passes through the test region having density gradients, variations in the refractive index would deflect light passing through the fluid and cast a shadow on the recording plane. The shadowgraph technique requires a light source, two concave mirrors and a high-speed camera with DAQ system. The schematic diagram of the shadowgraph setup is shown in Fig. 3.5.

The two concave mirrors are slightly tilted such that light from the source is collimated and the parallel rays of light are passed through the test region of the shock tube. By focusing the lens, a much larger field of view is obtained on the

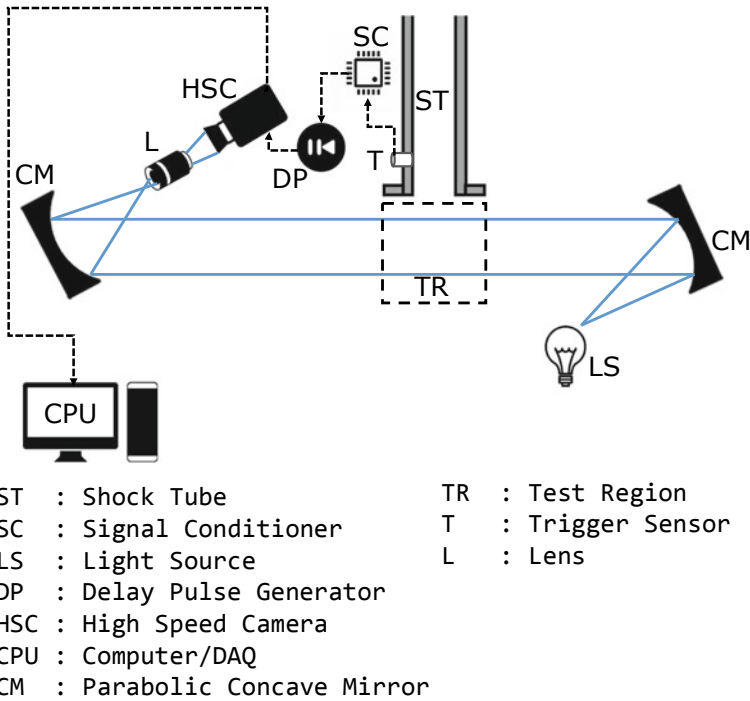


Fig. 3.5 A schematic diagram of the shadowgraph technique and the various components used in the technique

recording plane. A pressure transducer (T) is used as the trigger source. A delay unit is set between the sensor and camera by using delay pulse generator, so as to control trigger timing during the test time of the event. Successive images of the test region are captured by high-speed camera and are available for further processing.

3.2 Shock Tubes Used for Experimental Investigation

The response of granular materials under different types of blast events like air-blast and buried-blast are discussed in Chaps. 4, 5, 6 and 7. Shock tubes of different dimensions are used to simulate shock/blast loads based on the intended applications. The shock tube experiments presented in this book were performed in Department of Aerospace Engineering, Indian Institute of Science. Three different types of shock tube are used in the experimental investigation, namely

- (i) Diaphragmless shock tube (DST)
- (ii) Vertical shock tube (VST)
- (iii) Table-mount shock tube (TST)

DST facility is used to generate shock loading, while, VST and TST setup are used to generate air-blast and buried-blast loading, respectively. The conventional shock tube has to be slightly modified based on some requirements and preferences which would help in accommodating the granular test chamber in the shock tube. The detailed discussion of the test chamber introduced in the shock tube facility is mentioned in the respective chapters, Chap. 4 (shock loading), Chaps. 5 and 6 (air-blast loading) and Chap. 7 (buried-blast loading).

3.2.1 Diaphragmless Shock Tube (DST)

3.2.1.1 Configurations and Operation

The diaphragmless shock tube is designed to operate in shock wave mode, with a wide range of shock strengths. The shock tube consists of two major sections, driver and driven section. The driver section is mounted perpendicular to the driven section with a capacity of 0.0454 m^3 . The driven section is 6.1 m long with an internal diameter of 50 mm (Hariharan et al. 2011). The driver and driven section are connected through a pneumatic valve. Schematic diagram of the diaphragmless shock tube assembly and the photograph of the setup are shown in Fig. 3.6. The end of driven section is covered with an end flange, which is generally replaced by a test chamber. A digital pressure gauge (PRM-300M) is fixed at the driver section to record the fill pressure at the time of release of the valve. Shock wave of desired strength can be generated by varying the fill pressure in driver section. In order to measure the shock wave velocity and pressure, piezoelectric pressure transducers P_1 and P_2 are flush mounted at the tail end of the driven section.

The conventional shock tubes are operated by rupturing metal diaphragms placed between the driver and driven sections. Due to the random rupturing process, repeatability of the experimental results is difficult to achieve. Further, diaphragm method is a time-consuming process which involves regular replacement of diaphragm after each test run. The conventional metal diaphragm is replaced by a fast-opening pneumatic valve (ISTA, St. Petersburg, Russia) in DST. The valve has an opening time of around 5 ms. Although, high-speed pneumatic valve cannot replicate the opening time achieved through rupturing process, which is around $250\text{--}500 \mu\text{s}$ (Janardhanraj 2015). However, the valve offers many advantages over the diaphragm. The valve produces well-defined repeatable shock waves at ambient pressure conditions which are comparable with the theoretical values (Britan et al. 2001). The photograph of the high-speed pneumatic valve mounted between driver and driven section is shown in Fig. 3.7.

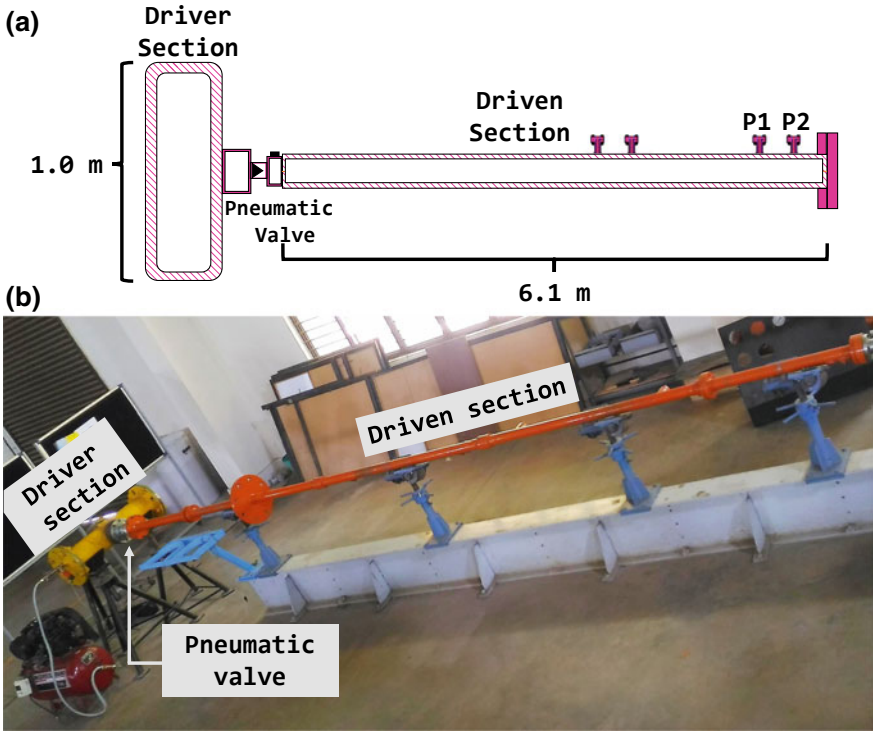
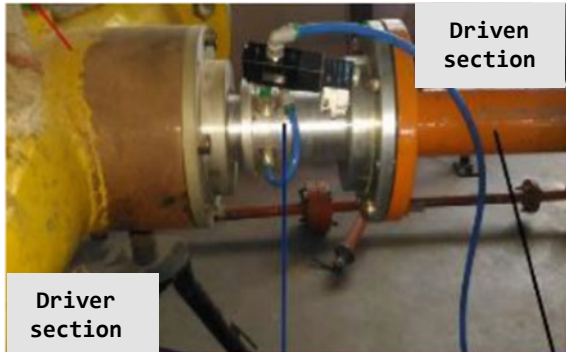


Fig. 3.6 Diaphragmless shock tube test facility (DST): **a** schematic diagram of the setup; **b** photograph of the test facility

Fig. 3.7 A photograph of the high-speed pneumatic valve mounted between driver and driven section



3.2.1.2 Initial Experiment Performed in DST

All the experiments involving DST are carried out using nitrogen as the driver gas while the driven section is kept at ambient atmospheric conditions. Initial experiments are performed without the test sample at the end of the driven section. The pneumatic valve is released upon filling required pressure of nitrogen gas in the driver section. The pressure data recorded from a typical shock tube experiment is shown in Fig. 3.8. The first jump seen in the signal of P_1 is the incident shock wave and the second jump corresponds to the reflected shock wave from the end wall of the shock tube. A distinct plateau pressure region is observed at the end of the first jump, indicating a constant pressure zone is maintained behind the travelling shock front.

It is to be noted that the incident shock wave pressure level (P_2) is independent of the test material located at the end of the shock tube while the pressure level of the reflected shock wave (P_5) depends on the material properties of the sample. The pressure signals shown in Fig. 3.8 are against rigid stainless-steel end flange. Hence, the strength of the shock wave is characterized using incident shock Mach number and the corresponding pressure behind the incident shock front, i.e., the peak incident pressure (P_2), where, Mach number (M_s) is defined as ratio of the velocity of the shock wave in a given medium to the velocity of the sound in the same medium. The velocity of the incident shock wave in a shock tube is calculated by time of flight method, measuring the time interval between the signals recorded by transducers P_1 and P_2 .

The shock impact experiments on the granular materials are performed with four different shock intensities. The peak incident pressure recorded for fill pressures of 5 bar, 10 bar, 20 bar and 30 bar and their corresponding shock strength (M_s) are listed in Table 3.1

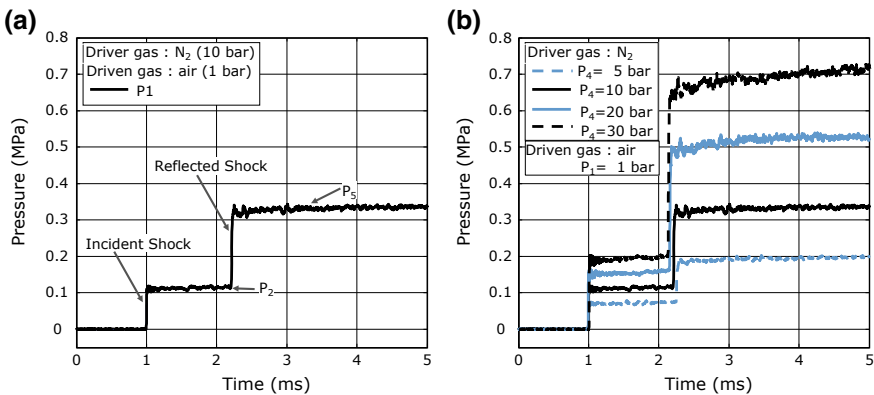


Fig. 3.8 Typical pressure signals recorded at P_1 of DST. **a** Pressure–time histories recorded for P_4 of 10 bar of N_2 (SW2); **b** shock wave signature for case SW1, SW2, SW3 and SW4 (Table 3.1)

Table 3.1 Peak incident pressure and incident Mach number obtained for different driver pressures in DST

Shock wave	Nitrogen fill pressure, P_4 in bar ^a (± 1)	Peak incident pressure, P_2 in MPa (± 0.002)	Incident Mach No., M_s (± 0.01)
SW1	5	0.071	1.29
SW2	10	0.112	1.43
SW3	20	0.164	1.57
SW4	30	0.205	1.70

^a1 bar = 10^5 N/m²

3.2.2 Vertical Shock Tube (VST)

3.2.2.1 Configurations and Operation

The vertical shock tube is a long cylindrical tube which essentially consists of two sections: the driver section, the one which contains high-pressure gas and the driven section, which is kept relatively at low pressure. The vertical shock tube is 5 m long installed on a vertical platform above the ground level. The schematic diagram of the vertical shock tube (VST) and the photograph of the shock tube mounted in the two-storied platform are shown in Fig. 3.9.

VST features two identical shock tubes (L and R) with an internal diameter of 135 mm which are mounted on a common platform. The exit of the tubes is connected to large cylindrical dump tank, where the samples are generally located. The shock tube test assembly is made up of customized modular individual units of 0.5 m, which enables us to configure shock tubes of varying driver and driven length. The driver section can be varied from 0.5 m to 1.5 m in length and similarly maximum length of driven section is 4.5 m, with flexibility of reducing the length in units of 0.5 m. The maximum working pressure of the individual modular section is about 100 bar (1 bar = 10^5 N/m²).

The driver and driven sections are separated by an aluminium diaphragm. The metal diaphragm is housed in the diaphragm mounting section. Rubber O-rings are provided in the flange of the diaphragm mounting section to ensure leak-proof sealing. Metal diaphragm is generally provided with a groove of specific depth; this ensures controlled rupture with repeatable bursting pressure (Fig. 3.10a). The diaphragm is ruptured using high-pressure compressed driver gas. The geometry of the groove is very critical in the formation of a uniform plane shock wave front. A perfect petal pattern as shown in Fig. 3.10c is an indication of ideal rupture of diaphragm. Shock waves of different intensities are obtained by bursting the diaphragm at different pressure ratios. Higher bursting pressure can be achieved by having a shallow groove depth on the diaphragm or by increasing the diaphragm thickness. A digital pressure gauge (PRM-300 M) is fixed at the driver tube to record the diaphragm rupture pressure (P_4) and a series of pressure transducers are mounted along the driven

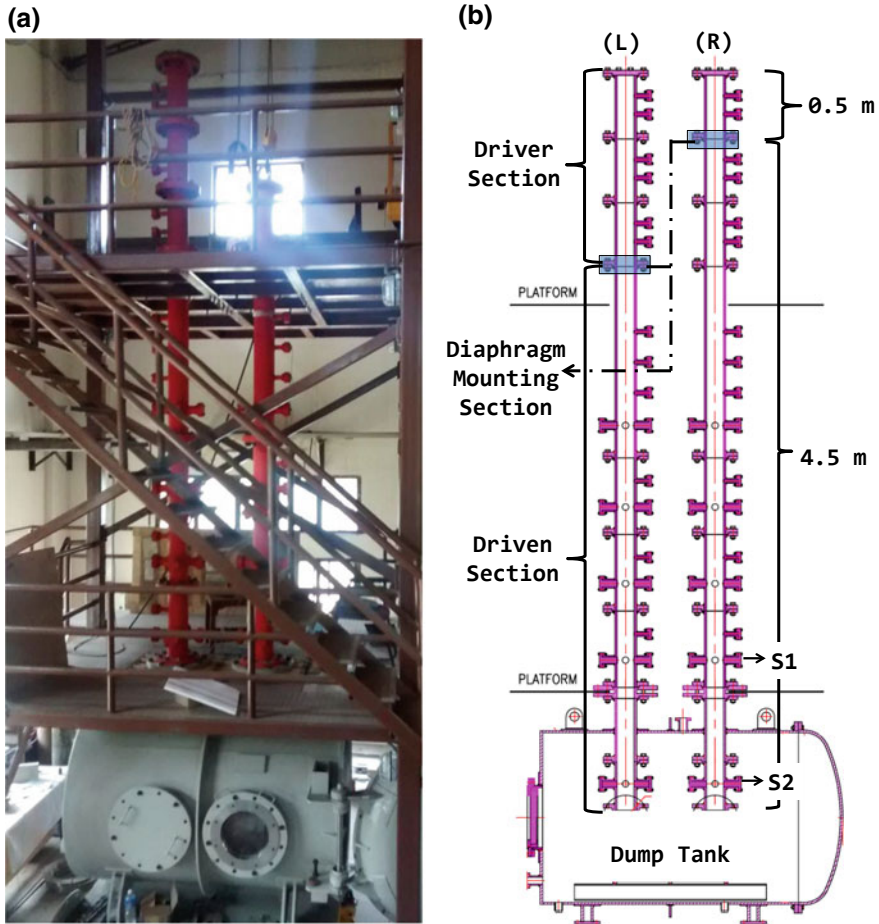


Fig. 3.9 Vertical shock tube test facility (VST): **a** photograph of the test facility; **b** schematic diagram of the setup

section to measure the pressure intensity of the shock wave. The photograph of the grooved aluminium diaphragm before and after rupture is shown in Fig. 3.10b-c.

3.2.2.2 Initial Experiments Performed in VST

A few sets of initial experiments were carried out to determine the operative length for the driver and driven section. The focus of this section is to generate the blast wave waveform identical to air-blast explosion using a shock tube. Nitrogen or helium gas is used as driver gas, and the driven section is kept at atmospheric pressure. A driver section of 0.5 m and a driven section of 4.5 m provided a blast wave pressure

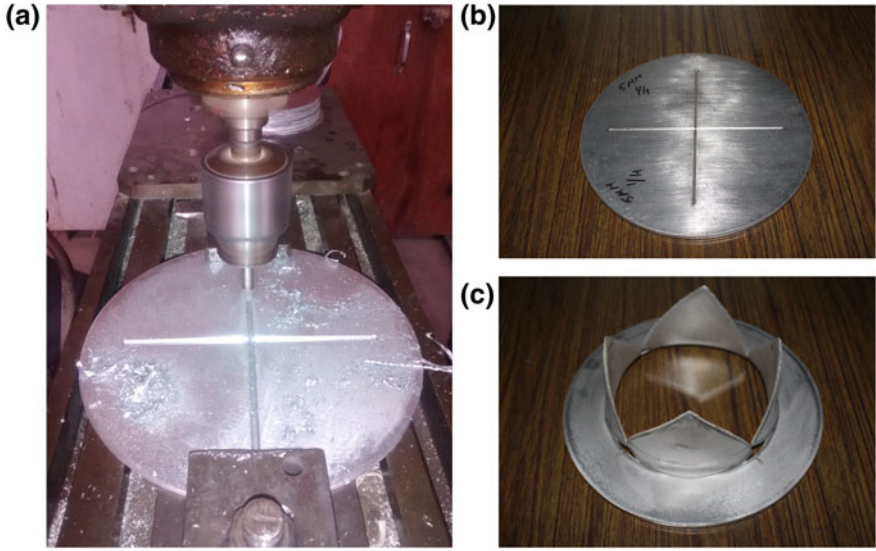


Fig. 3.10 Diaphragm used in VST: **a** grooves are made on the surface of aluminium diaphragm; **b** before rupture; **c** after rupture

profile with helium as driver gas. A typical pressure–time response recorded close to the end of the driven section is shown in Fig. 3.11. Observing the pressure profile of He at S_2 , the reflected rarefaction waves from the driver section catch up with the incident shock front and decay the incident shock pressure levels. Further, a peak-reflected overpressure is achieved upon reflection against the sample surface. Response time of the rarefaction waves is significant in the formation of the blast

Fig. 3.11 Typical pressure signal recorded at S_2 of VST, when operated with nitrogen and helium as driver gas

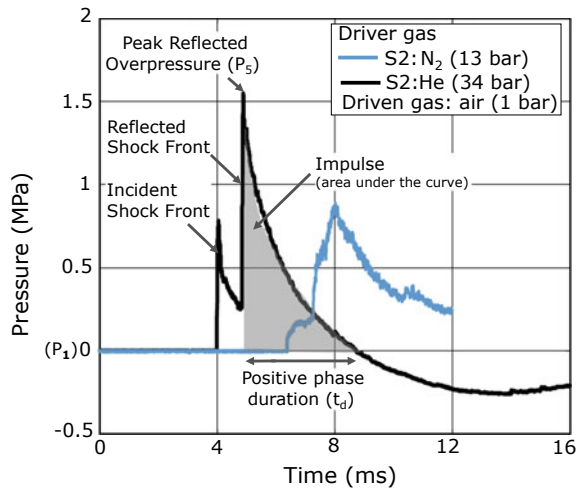


Table 3.2 Rupture pressure of different diaphragms used in VST

Diaphragm type ^a	Rupture pressure, P_4 in bar (1 bar = 10^5 N/m ²)
4 mm–1 mm	35 (± 1)
5 mm–2 mm	28 (± 2)
2 mm–0.25 mm	17 (± 1)
2 mm–0.4 mm	13 (± 1)
2 mm–0.5 mm	11 (± 1)
2 mm–1 mm	5 (± 1)

^a4 mm–1 mm: 4 thick diaphragms with a groove of 1 mm depth

wave, which eventually decides the blast wave parameters. The blast wave pulse generated from the VST is characterized by blast parameters such as ‘peak-reflected overpressure’, ‘reflected impulse’ and ‘positive time duration’ as the blast parameters. Peak-reflected pressure (P_5) of the second jump is considered as peak overpressure value; the positive phase duration (t_d) is the time taken for the reflected pressure (second jump) to decay to the atmospheric pressure levels (P_1); and the ‘impulse’ is determined by calculating the area under the pressure–time curve (shaded portion in Fig. 3.11) over the positive phase duration (t_d). The initial test runs performed in VST were against granular sample (unlike against solid flange in case of DST), hence the peak overpressure values shown in this section are problem-specific and are discussed in detail in Chap. 5 for various other granular samples. However, qualitative information on the blast wave parameters obtained is discussed in the present section.

The experiments presented in the present study involving air-blast loading against sand deposits are performed using the shock tube-(R) of VST with the following test configuration: (i) driver length of 0.5 m with helium gas (ii) driven length of 4.5 m. (iii) three different aluminium diaphragms are used having thickness of 5 mm, 4 mm, and 2 mm with groove depth of 2 mm, 1 mm, and 0.4 mm, respectively. In addition, the shock tube was operated with various other diaphragms, and the complete list of diaphragms and their corresponding rupture pressure are listed in Table 3.2.

3.2.3 Table-Mount Shock Tube (TST)

3.2.3.1 Configurations and Operation

Table-mount shock tube (TST) is a portable shock tube, which can be easily mounted on a table. TST can be operated in both vertical and horizontal positions based on the need of the experiment. TST is buried inside sand deposit and the shock tube is mounted vertically such that tail end of shock tube is facing upwards. A photograph of the shock tube mounted vertically upwards is shown in Fig. 3.12a, and the schematic diagram of the shock tube (TST) is shown in Fig. 3.12b. The length of the driver section is 55 mm and the driven section is 175 mm long and both the sections have

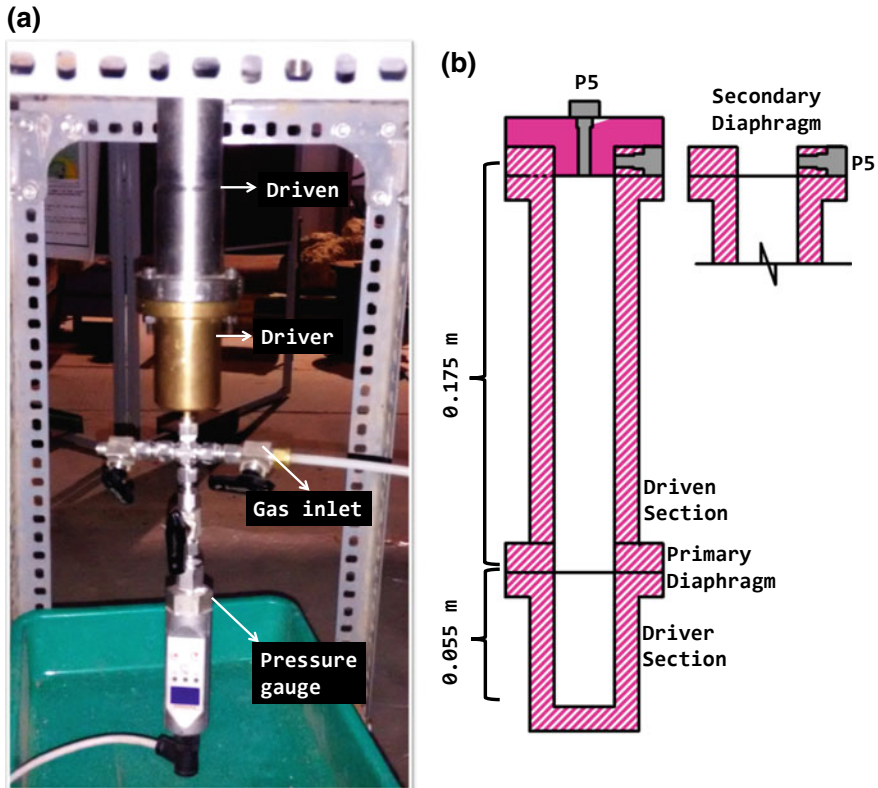


Fig. 3.12 Table-mount shock tube test facility (TST): **a** photograph of the test facility; **b** schematic diagram of the setup

an internal diameter of 25 mm. The driver section is connected to the high-pressure helium cylinder using a flexible hose, which is used to rupture the diaphragm. The rupture pressure is recorded using Barksdale pressure switch (SW2000). The TST is provided with two diaphragm mounting sections, primary diaphragm separating the driver and driven sections, and the secondary diaphragm separating the driven section and the surrounding atmosphere. Mylar® sheet (polyester film) of thickness 0.1 mm is used as the primary diaphragm, and a tracing paper (60-65 GSM) is used as the secondary diaphragm. The primary diaphragm and the secondary diaphragm are held in position with the help of the fasteners, ensuring leak-proof conditions.

3.2.3.2 Initial Experiments Performed in TST

A blank test run is performed with an end flange placed at the secondary diaphragm section. The shock tube is operated by rupturing the Mylar® diaphragm. The photograph of Mylar® before and after rupture is shown in Fig. 3.13. A typical blast

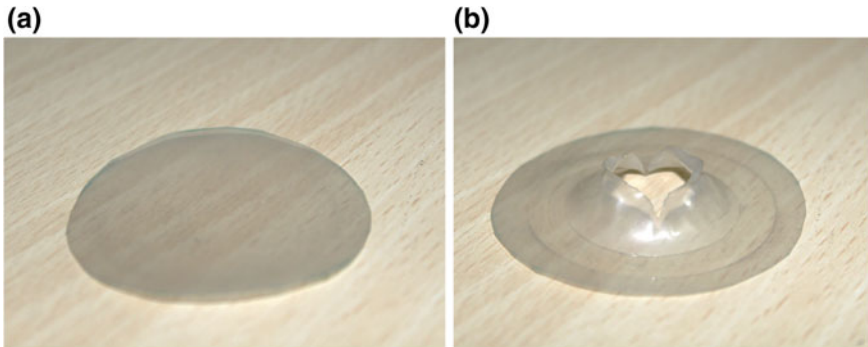
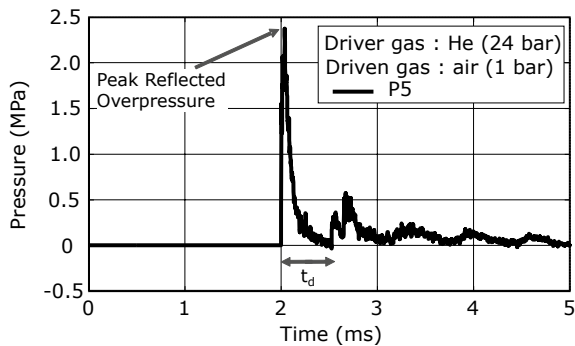


Fig. 3.13 Diaphragm used in TST: **a** before rupture; **b** after rupture

Fig. 3.14 Typical pressure signal recorded at P'_5 of TST, when operated with helium as driver gas



wave signal recorded from the P_5 pressure sensor located on the end flange is shown in the Fig. 3.14. The peak-reflected pressure is found to be 23.75 ± 0.5 bar, and the positive phase duration is measured to be $475 \pm 25 \mu\text{s}$.

TST is used to investigate the buried-blast interaction with sand deposits. The exit of TST with the paper diaphragm is embedded within the sand deposit (details of the buried-blast experiment are discussed in Chap. 7). The thickness of paper diaphragm is chosen such that it has minimum effect on the blast wave profile and the paper also has to withstand the overburden pressure exerted by the sand. The pressure signal of the blast wave at the exit of the shock tube is captured using sensor P'_5 , located just above the secondary (paper) diaphragm.

3.3 Scaling Laws and TNT Equivalence

By using scaling laws, some real-scale explosion properties can be predicated in the laboratory (or outdoor space) by performing experiments at smaller scale. Blast scaling law was first postulated by Sach during World War I and later formulated by

Hopkinson and Cranz during the period of World War II for air-blast and underwater blast conditions (Baker et al. 1991). The most popular and commonly used scaling law is ‘Hopkinson–Cranz’ scaling law which is also known as cube-root scaling law. Let us consider an observer placed at a distance ‘ R ’ from the centre of an explosive source (explosive charge of diameter, ‘ d ’ and mass ‘ W ’) and observer experiences a blast wave of peak overpressure ‘ P_s ’ with a positive duration, ‘ t_d ’ and an impulse ‘ I ’. The Hopkinson–Cranz scaling law states that for an observer now stationed at the distance ‘ λR ’ from the centre of a similar explosive (but with different mass, ‘ λd ’) will experience a blast wave of same amplitude P_s but with a scaled positive duration ‘ λt_d ’, and impulse ‘ λI ’ (Baker 1973). A parameter λ is introduced as the scaling factor in Eq. (3.1).

$$\lambda = \frac{1}{W^{\frac{1}{3}}} \quad (3.1)$$

The cube-root scaling law implies that all the physical properties with the dimension of pressure and velocity remains unchanged after scaling and the rest are scaled using the scaling factor (λ). The distance of the target from the explosion after scaling is represented by cube-root scaled distance (Z) or commonly referred as scaled distance (Eq. 3.2). Scaled distance is often used to characterize the explosion damage which relates similar blast effects from various charge weights of same explosive at various distances.

$$Z = \frac{R}{W^{\frac{1}{3}}} \quad \text{or} \quad Z = \frac{H}{W^{\frac{1}{3}}} \quad (3.2)$$

In order to apply the scaling laws, the simulated blast wave of interest has to be represented using an equivalent TNT weights (W), which would yield similar blast effects. Hence, the blast parameters (P_s , t_d , I) generated from the blast simulators are to be related to an equivalent spherical air-burst or hemispherical surface-blast of TNT explosion (of weight ‘ W ’), depending on the type of explosion. For an air-blast condition, ‘ H ’ is defined as altitude of the explosion above the ground surface (assuming target is present at ground zero level) and in the case of surface-blast, ‘ R ’ is the stand-off distance of the target from source of explosion.

Kingery and Bulmash (1984) have developed charts to predict spherical and hemispherical air-blast parameters with respect to the scaled blast distance. These charts are developed based on explosive field tests conducted with charge weights from less than 1 kg to over 400,000 kg, at varying stand-off distances. Higher-order polynomial curves are fitted with the available large database of experimental records. These empirical charts available in UFC 3-340-02 (2008) are widely used in the literature to predict the blast wave parameters like peak overpressure, impulse and positive phase duration for a specific scaled blast distance (Z). The same charts are used in this book to predict the equivalent TNT and corresponding stand-off distance (H/R) for the available blast parameters (P_s , t_d , I) obtained from the simulators (like shock tube). Unique value of weight of ‘TNT’ and stand-off distance ‘ R ’ will be

generated in terms of scaled distance (Z). The data of Kingery and Bulmash (1984) are in graphical form in most of the available literature (Needham 2010; Smith and Hetherington 1994), and it is difficult to accurately back calculate the 'Z' values from them. Recently, Shin et al. (2015) has performed numerical modelling of the air-blast phenomenon using CFD analysis for scaled distance range of $0.0553 \leq Z < 40 \text{ m/kg}^{1/3}$ and compared the results with the chart developed by Kingery and Bulmash (1984). The numerical modelling compares very well with Kingery and Bulmash chart for Z greater than $1 \text{ m/kg}^{1/3}$ and it under predicts incident impulse and reflected peak overpressure value for $Z < 1 \text{ m/kg}^{1/3}$. During this process, they have developed a series of polynomial functions for a range of Z value and listed out the polynomial coefficient value for various blast parameters.

Polynomial functions generated by Shin et al. (2014) are polynomial functions of the form shown in Eq. (3.3), and the corresponding blast parameter coefficients are listed in Table 3.3. The functional form of the equations is similar to the one adopted by follows that adopted by Kingery and Bulmash (1984).

$$Y = C_0 + C_1 \cdot U + C_2 \cdot U^2 + \dots + C_N U^N \quad (3.3)$$

Table 3.3 Polynomial coefficients for reflected peak overpressure, reflected impulse and positive phase period

Parameter	P_s (kPa)		$I/W^{1/3}$ (kPa ms $\text{kg}^{1/3}$)		$t_d/W^{1/3}$ (ms/ $\text{kg}^{1/3}$)
	$Z < 0.5$	$Z > 0.5$	$Z < 0.5$	$Z > 0.5$	$Z > 0.83$
K_0	1.613	-0.4784	0.2159	0.8609	-0.228
K_1	1.98	0.922	0.7506	1.265	0.9841
C_0	5.749	2.251	3.0934	3.839	3.063
C_1	-1.472	-2.444	-1.892	-2.128	0.9747
C_2	0.1963	1.752	2.003	1.794	0.4196
C_3	1.416	-1.329	2.239	-1.256	-2.577
C_4	-1.999	-1.514	0.6488	0.4165	2.549
C_5	-2.735	4.729		-0.05467	-0.7938
C_6	3.556	-3.051		0.000972	
C_7	1.131	-2.02			
C_8	-0.8315	3.52			
C_9	0.5336	-2.843			
C_{10}	-1.676	3.272			
C_{11}	-0.2248	-1.233			
C_{12}	1.074	-0.6161			
C_{13}	-0.2745	1.211			
C_{14}		-3.61			
C_{15}		2.491			

where, Y = common (base 10) logarithm of the blast parameter (Reflected overpressure, P_s ; Positive phase period, t_4 ; Reflected impulse, I)

$$U = K_0 + K_1 \cdot \log(Z) \quad (3.4)$$

where, C and K = constants and N = order of the polynomial.

With the help of these polynomial functions and coefficients, one can accurately predict 'Z' value ($>1 \text{ m/kg}^{1/3}$) for the blast parameters and thereby having an estimate of equivalent TNT explosion. A similar procedure of estimating TNT weight and stand-off distance is mentioned in Aune et al. (2016).

3.4 Natural and Synthetic Granular Materials

Granular materials considered in this book are classified as natural and synthetic materials. The coarse sand (CS) and fine sand (FS) are naturally occurring granular material (river sand) and glass bead (GB) is a synthetic material. The sand particle (CS and FS) and glass bead (GB) samples are used in shock loading experiments shown in Chap. 4. The experiments involving the blast loading in Chaps. 5, 6 and 7 are primarily carried out using fine sand (FS) samples. The images of different granular materials used in the experimental investigation are shown in Fig. 3.15.

3.4.1 Coarse Sand

The grain size of coarse sand (CS) varies from 1.18 to 4.75 mm and is classified as poorly graded with symbol SP as per Unified Soil Classification System (ASTM D2487-11 2011). The majority of the CS grain particles are angular shaped with rough surfaces. The grain size distribution of the granular particles is obtained by



Fig. 3.15 Images of granular materials used in the experimental investigation

performing a dry sieve analysis test (ASTM D6913-04 2004). The grain size distribution curve for the different granular materials used in the experiments is shown in Fig. 3.16. The gradation curve of the CS particle indicates the sample is poorly graded with grains more uniform in size. The gradation property and the engineering properties of the granular samples are listed in Table 3.4.

Fig. 3.16 Grain size distribution of the granular particles

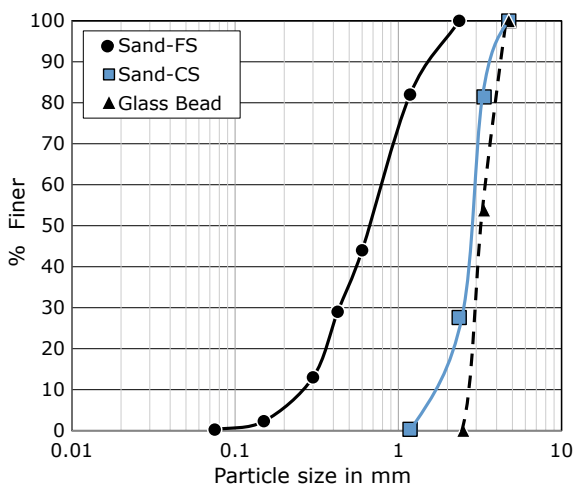


Table 3.4 Properties of different granular materials used in the experimental study

Parameter	Find sand (FS)	Coarse sand (CS)	Glass bead (GB)
d_{10} (mm)	0.26	1.80	2.90
d_{50} (mm)	0.70	2.75	3.50
Coefficient of uniformity, C_u	3.07	1.67	1.20
Coefficient of curvature, C_c	0.96	1.15	0.94
Maximum void ratio, e_{max}	0.97	0.88	0.76
Minimum void ratio, e_{min}	0.53	0.55	0.58
Young's modulus (MPa)	14.95	-	-
Poisson's ratio	0.30	-	-

3.4.2 *Fine Sand*

Dry river bed sand is used for the fine sand material. The sand is completely oven dried at 130 °C and subsequently air dried for 24 h prior to the experiments. The grain size of fine sand (FS) varies from 0.075 to 2.36 mm and classified as well graded with symbol SW as per Unified Soil Classification System (ASTM D2487-11 2011). As we observe the gradation profile of FS in Fig. 3.16, the curve stretches more or less with a uniform slope across wide range of particle size. The Young's modulus of fine sand is determined from the consolidated undrained triaxial compression test. The tests are carried out at three different confining pressures of 100, 200 and 300 kPa. The engineering properties of FS sand are also listed in Table 3.3.

3.4.3 *Glass Beads*

In order to consider shape effect of granular particles, soda lime glass beads of smooth surface finish are considered. The glass beads (GB) used are spherical in shape with particle size of 3 mm and 4 mm (in proportion of 50:50). The gradation curve of GB samples is comparable to the CS sample (Fig. 3.16).

3.4.4 *Supplementary Materials*

Wire mesh and geotextile are used as facing formwork material for the granular materials against shock loading. The aluminium pipe is used as model material for the buried pipe experiment (discussed later in this Chap. 6). The images of the supplementary material used in the experimental study are shown in Fig. 3.17. The physical and engineering properties of the supplement materials are listed in Table 3.5.

A stainless-steel wire mesh is used as a protective screen for supporting the infill granular materials. The wire mesh (WM) is plain steel rolled wire of 0.5 mm diameter with a square-opening aperture of 2.5 mm × 2.5 mm. The tensile strength of the wire mesh is determined as per ASTM standards (ASTM D4964-96 2000). The geotextile is a polypropylene woven geotextile of 0.6 mm thickness. Tensile strength of the geotextile is determined by wide width strip method (ASTM D4595-11 2011), and it is found to be 55 kN/m. An aluminium pipe of internal diameter of 25 mm ($I_{d,al}$), with a wall thickness (t_{al}) of 1.25 mm, is used in the experiments. The mechanical properties of the aluminium pipe are listed in Table 3.4. The bending of the pipe along the longitudinal axis will be of major concern. The flexural stiffness value of the pipe is determined by multiplying the Young's modulus (E) and the moment of Inertia (I), and the EI value for aluminium pipe used is found to be 613.6 N m².

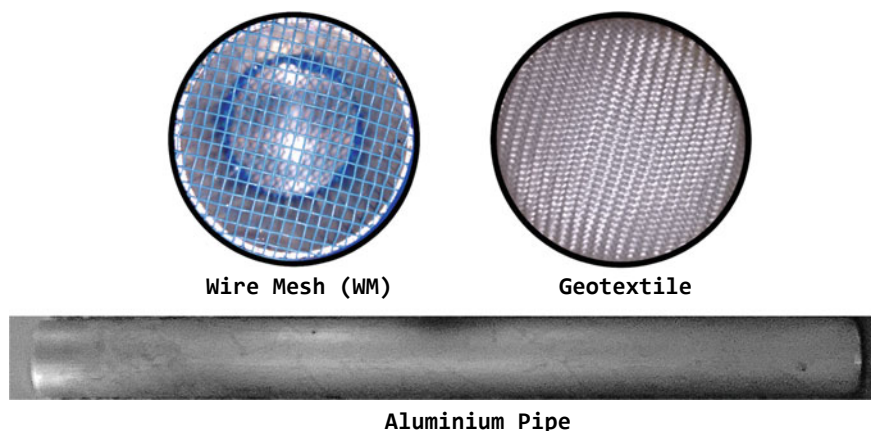


Fig. 3.17 Images of supplement materials used in the experiments

Table 3.5 Properties of the supplement materials used in the experiments

Parameter	Geotextile	Wire mesh	Aluminium pipe
Thickness (mm)	0.6	0.5	1.25
Mass per unit area (g/m^2)	247	801	–
Ultimate tensile strength	55 kN/m	20 kN/m	97 MPa
Young's modulus	–	–	68.9 MPa

3.5 Test Bed Preparation

While preparing the sand bed, it is important to maintain constant relative density, such that the same test conditions can be reproduced. For this purpose, the sand pluviation technique is used. The sand pluviator tool is used to generate test sample of constant relative density (RD). Relative density is defined as the ratio of the difference between the void ratio of cohesionless soil in its loosest state (e_{\max}) and existing natural state (e) to the difference between its void ratio in the loosest (e_{\max}) and densest states (e_{\min}).

$$\text{RD} = \frac{e_{\max} - e}{e_{\max} - e_{\min}} \quad (3.5)$$

The schematic diagram of the sand pluviator and the photograph of the pluviator tool are shown in Fig. 3.18. The sand pluviation tool consists of a fixed overhead hopper, which is in turn connected to a flexible, adjustable (100–500 mm in height) PVC pipe. The bottom end of the PVC pipe is connected to a sand diffuser. The sand diffuser is a hollow cylindrical pipe of 100 mm in length, with a 60° inverted cone

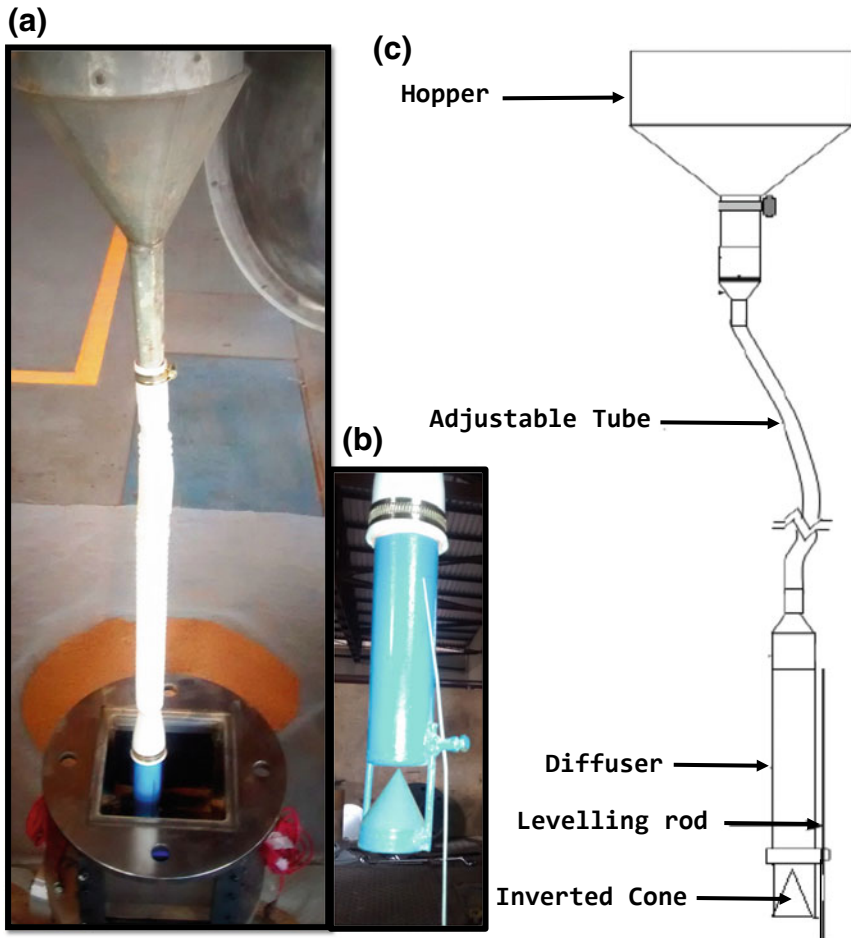


Fig. 3.18 Sand pluviator: **a** photograph of the sand pluviator tool; **b** close-up view of the diffuser; **c** schematic diagram of the pluviator

welded to the opening end (Fig. 3.18b). The sand particles are poured into the hopper; the sand passes through the PVC pipe and disperses out of the diffuser. The diffuser is provided with a thin levelling rod which is set to a pre-marked level, prior to sand raining. The diffuser is held in upright position and is made to travel back and forth such that the sand that exit from the conical surface is uniformly distributed in the test chamber. Simultaneously, the diffuser is gradually traversed in the vertical direction as and when the sand bed level reaches the tip of the levelling rod, thus maintaining a constant height of fall. A constant sand flow rate is thus achieved, and the density is relatively kept constant. Such a method will help in delivering repeatable sand layer deposits. The height of fall determines the desired relative density of the sand deposit (Vaid and Negussey 1984). Height of fall is defined as the distance between the top

Table 3.6 Impedance value for loose and dense sand deposit

Fine sand category	Dry density, ρ (kg/m ³)	Young's modulus, E (MPa)	Impedance, $\rho.c$ (kPa s/m)
Loose sand (RD45)	1566	14.95	177.82
Dense sand (RD73)	1658	19.13	206.67

of the sand bed to the bottom of the sand diffuser (base of the cone). The relative density of the sand deposit is monitored by placing small cups of known volume at different locations in the sand chamber (Latha and Krishna 2008).

The sand grain particles are rained down at two different heights of fall, 10 and 20 cm. The loose and dense sand deposits are thus prepared with a relative density of 45 and 73% with an approximate dry density of 1566 kg/m³ and 1658 kg/m³, respectively. The impedance value of the sand deposit is calculated by multiplying the density (ρ) achieved and the sound wave velocity (c) in the medium. The wave velocity is determined from the Young's modulus (E) value using Eq. (3.6). The impedance value obtained for the loose and dense sand deposit is mentioned in Table 3.6.

$$c = \sqrt{\frac{E}{\rho}} \quad (3.6)$$

3.6 Summary

Various instruments and measurement techniques involved in the shock tube experiments are discussed. The details of three different type of shock tubes are presented, namely diaphragmless shock tube (DST), vertical shock tube (VST) and table-mount shock tube (TST). DST is configured to generate shock loading on the granular materials, with the help of fast pneumatic valve. While, VST and TST are configured to simulate air-blast loading and buried-blast loading, respectively. The results of the initial experiments carried out in these three-mentioned shock tubes are presented. The properties of various granular materials, supplement supporting materials and model materials used against shock and blast loading are discussed in the present chapter. The sand pluviation technique and the procedure to obtain loose and dense sand deposit in the test chamber are described in the present chapter. The test chamber configurations are different for air and buried-blast loading. Hence, the sample preparation along with details of the test chamber is presented in the experimental setup section of Chaps. 5 and 7 for air-blast and buried-blast loading, respectively.

References

- ASTM D2487-11 (2011) Standard practice for classification of soils for engineering purposes (unified soil classification system). ASTM International, West Conshohocken, PA, USA
- ASTM D4595-11 (2011) Standard test method for tensile properties of geotextiles by the wide-width strip method. ASTM International, West Conshohocken, PA, USA
- ASTM D4964-96 (2000) Standard test method for tension and elongation of elastic fabrics (constant-rate-of-extension type tensile testing machine). ASTM International, West Conshohocken, PA, USA
- ASTM D6913-04 (2004) Standard test methods for particle-size distribution (gradation) of soils using sieve analysis. ASTM International, West Conshohocken, PA, USA
- Aune V, Fagerholt E, Langseth M, Borvik T (2016) A shock tube facility to generate blast loading on structures. *Int J Prot Struct* 7(3):340–366
- Baker WE (1973) Explosions in air. University of Texas Press, Austin
- Baker WE, Westine PS, Dodge FT (1991) Similarity methods in engineering dynamics-theory and practice of scale modeling. Elsevier
- Britan A, Ben-Dor G, Igra O, Shapiro H (2001) Shock waves attenuation by granular filters. *Int J Multiph Flow* 27(4):617–634
- Hariharan MS, Janardhanraj S, Saravanan S, Jagadeesh G (2011) Diaphragmless shock wave generators for industrial applications of shock waves. *Shock Waves* 21(3):301–306
- Janardhanraj S (2015) Investigations on supersonic flows in miniature shock tubes. Ph.D. thesis, Indian Institute of Science
- Kingery CC, Bulmash G (1984) Air blast parameters from TNT spherical air burst and hemispherical surface burst. Defence technical information center, Ballistic Research Laboratory, Aberdeen proving ground, Maryland, USA, Report BRL, 02555
- Latha GM, Krishna AM (2008) Seismic response of reinforced soil retaining wall models: influence of backfill relative density. *Geotext Geomembr* 26(4):335–349
- Needham CE (2010) Blast waves (shock waves and high pressure phenomena). Springer, Berlin, pp 49–50
- Shin J, Whittaker AS, Amjad A, Aref AJ, Cormie D (2014) Air-blast effects on civil structures. State University of New York at Buffalo, Report, MCEER-14-0006
- Shin J, Whittaker AS, Cormie D (2015) Incident and normally reflected overpressure and impulse for detonations of spherical high explosives in free air. *J Struct Eng* 14(12):04015057
- Smith PD, Hetherington JG (1994) Blast and ballistic loading of structures. Butterworth-Heinemann, London
- UFC 3-340-02 (2008) Structures to resist the effects of accidental explosions. US Department of Defence, Washington, DC, USA
- Vaid YP, Negussey D (1984) Relative density of pluviated sand samples. *Soils Found* 24(2):101–105

Chapter 4

Attenuation of Shock Wave Through Granular Materials



4.1 Introduction

Upon explosion, a high-intensity shock wave front arises causing physical damage to structures and destruction of lives. Structural steel and reinforced concrete structures are commonly used as protective structures against explosion. Although they have high tolerance in mitigating the blast, the post-failure leads to generation of sharp debris particle. And most of these structures are permanent and involve considerable time and labour for the construction. Alternatively, sand bags are commonly used as protective barrier walls against shock waves. The function of temporary barrier walls built on the surface is to shield against the shock (Mach) waves resulting from a surface explosion and also to protect from secondary blast effects like projectile and debris impact. The infill sand particles absorb the energy from the impact and attenuate the shock pressure. An improvised version of sand bags is made out of geosynthetic materials. Geosynthetic reinforced soil (RS) wall is used as a protective structure in both civil and military application. The function of such a barrier wall is to shield against the blast effect from various sources like terrorist attacks, accidental detonation of stored explosives, munitions, battle field, etc. Reinforced soil structures are cost-effective and are prefabricated type of protective barriers, easy to setup and mobilize to different site conditions. Moreover, RS walls do not undergo brittle failure like concrete walls upon blast impact.

A commercially available geotextile encapsulated sand barriers products, Hesco Bastion Concertainer[®] are lately used in the military and civilian applications. The geotextile encapsulated sand barrier systems are made of cubical wire mesh formwork lined with geotextile and form a thick protective barrier when filled with granular materials. A photograph of surface-level bunker constructed using Hesco[®] barrier units ($0.6 \times 0.6 \times 1.2$ m) is shown in Fig. 4.1a. The granular barrier system also finds use in various industrial and commercial applications. For instance, they are used as ventilation seals in the mining industry to protect the mine workers from the violent

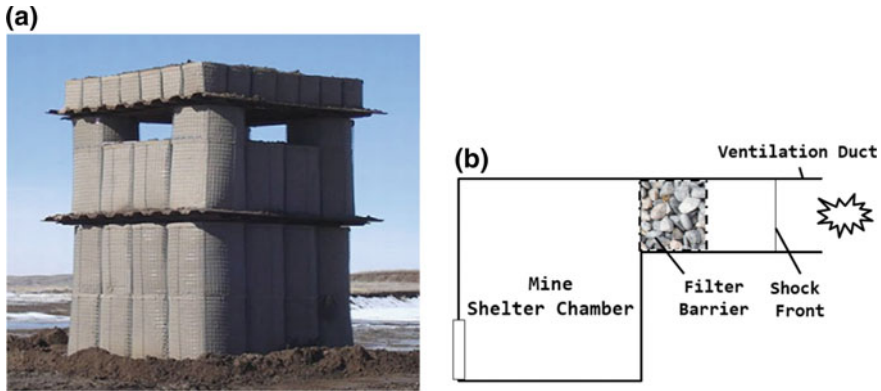


Fig. 4.1 Application of sand barrier walls: **a** HESCO bastion units used as a surface bunker in war fields (*Photo credits Hesco 2010*) and **b** granular barriers used as ventilation seals in ducts of mining chambers

explosions and prevent the outburst gases entering the confined working chambers (Sapko et al. 2009). Schematic diagram of the ventilation duct used in mining field is shown in Fig. 4.1b.

4.2 Previous Studies on Shock-Granular Interaction

Numerous literatures are available on the shock wave attenuation through granular medium (Ben-Dor et al. 1997; Britan et al. 1997, 2001, 2007; Engebretsen et al. 1996; Lv et al. 2017). Laboratory experiments were predominantly carried out using shock tube. Researchers have used various types of granular medium as an obstacle to mitigate the incoming shock wave. Engebretsen et al. (1996) have considered plastic and glass spheres as granular particles and studied the effect of the material density and particle size on the attenuation phenomenon. A series of shock tube experiments were carried out by Ben-Dor et al. (1997) on various types of granular materials (potash, polystyrene, nylon, sand etc.) by measuring the pressure in front and inside the granular layers. It was observed that the impact of shock wave has generated a transmitted wave in the granular media (resulting in the compaction of the granular particles) which is also influenced by gas filtration process. Britan et al. (2001) have used ceramic granules of $ZrSiO_4$, steel balls and glass beads as barrier medium for shock wave attenuation; the transmitted shock through the granular medium was analyzed with respect to the length of the sample and the air gap between the protective structure and the granular sample. In similar experiments, Britan et al. (2007) and van-der Grinten et al. (1985) have performed shock tube experiments by using long granular samples of length 2.5 m and 1.85 m, respectively. Researchers have also investigated the impact of shock wave on various kinds of textile and fabrics. Hefernan et al. (2006) have considered lightweight textile membranes like tarpaulins,

synthetic fibre, etc., in mitigating the blast wave. They have also proved that woven textile provides better resistance to blast wave when compared to non-woven textile. The reflection and propagation of shock wave in textile like satin, muslin and poly-cotton were experimentally investigated by Hattingh and Skews (2001). Instead of the expected attenuation behaviour, pressure amplification was observed at region adjacent to the textile layer. The authors have justified the amplification with the two involved mechanisms: (i) the transmitted shock wave reflecting back and forth between the end wall and the textile and (ii) generation of compression waves due to the piston-like movement of the textile (Hattingh and Skews 2001; Skews et al. 2010).

Geotextiles are widely used in Geotechnical Engineering as a separation and reinforcement medium (Koerner and Soong 2001; Ling et al. 2003). Under purview of geotextile-granular interaction, researchers have extensively studied the effects of particle shape and size (Afzali-Nejad et al. 2017; Athanasopoulos 1993), interlocking behaviour between geotextile and sand particles (Lee and Manjunath 2000) and interfacial frictional characteristics of sand and the reinforcing materials like geotextile and wire mesh (Vangla and Latha 2016). In addition, research has been conducted by various researchers to assess geotextile as a protective reinforcement medium (Bathurst et al. 2006; Hong et al. 2016; Koerner et al. 1996; Narejo et al. 1996). Most of these experiments were performed under quasi-static loading or cyclic loading conditions. Some of the researchers have used geotextile as protective wall against blast loads (Pieri 1998; Rose et al. 1998; Smith 2010; Yogendrakumar and Bathurst 1992). However, the role of geotextile as a blast mitigating medium is not much explored. Among the few available literature, Scherbatiuk and Rattanawangcharoen (2008) have performed full-scale field blast test on free-standing, soil-filled, geotextile-lined HESCO concertainer walls and reported displacement-time histories on the wall for different blast pressures. Ng et al. (2000) have carried out several detonation experiments on geosynthetic reinforced soil wall and reinforced earth wall with precast concrete facings and compared the damage patterns between them. Further, Zhiwei (2009) has performed full-scale field blast test on geosynthetic faced reinforced soil wall using 5 tons and 27 tons of TNT. Blast induced soil displacements and the overall performance of a reinforced soil wall were studied extensively using strain and pressure measurements on the walls, which are placed at different stand-off distances (30, 60 and 90 m) from the source of the blast. From the above cited literature, it is obvious that granular particles are widely used as attenuating medium for shock waves.

4.3 Experimental Test Program

A small-scale encapsulated sand barrier model is developed in the laboratory and tested using a shock tube. The shock waves are produced by using diaphragmless shock tube (DST). A photograph of the test chamber at the end of the driven section of the shock tube is shown in Fig. 4.2. The test chamber is also a cylindrical tube

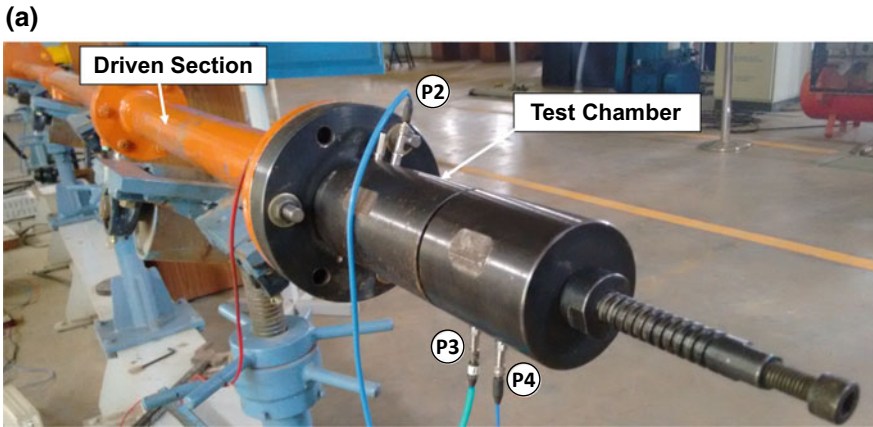
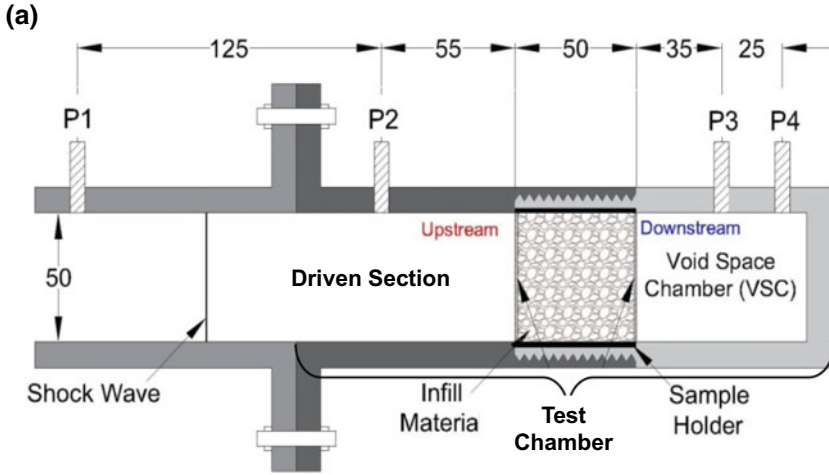


Fig. 4.2 Test chamber used in DST: **a** schematic diagram of the test chamber cross-section and **b** photograph of test chamber mounted in the shock tube (all dimensions are in mm)

having the same internal diameter as that of the driven section of DST (50 mm). The test chamber consists of extended driven section (70 mm), sample holder and void space section (VSC). The sample holder is held rigidly in the VSC, which is, in turn, connected to the main flange of the driven section. This assembly ensures that the sample is aligned along the axis of shock tube with a fixed end condition, and the shock wave impact is normal to the face of the sample. The region to the left of the sample is referred as upstream and to the right is referred as downstream end (see Fig. 4.2). Two pressure transducers P_1 and P_2 are mounted on the upstream side, and similarly, two transducers P_3 and P_4 are mounted on the downstream side of the sample.

The sample holder is filled with granular sample with a facing formwork cladded to the upstream and downstream side. Three different kinds of granular materials are

used as the infill material (refer Sect. 5.2), namely coarse sand (CS), fine sand (FS) and glass beads (GB). In order to evaluate the effect of shape and surface features of the infill material, glass beads are selected as the comparative infill material to the coarse sand. A stainless-steel wire mesh and/or geotextile layer is used as a protective facing formwork to support the infill granular materials. The barrier sample model is prepared using a cylindrical sample holder with an internal diameter of 50 mm (equal to ID of the shock tube). The thickness (or length, $L = 50$ mm) of the sample is kept constant throughout the study. The sample holder is provided with groove along the rim of the upstream and downstream edges, which would facilitate in binding the facing formwork. A pre-weighed quantity of the granular material is poured into the sample holder, and the desired bulk density is achieved by controlled tamping. All test samples are carefully prepared to achieve a relative density of 53% (± 1) which corresponds to bulk unit weight of 15.2 kN/m^3 , 15.6 kN/m^3 and 15.8 kN/m^3 for CS, GB and FS, respectively. The sample holder is then firmly held inside the slot provided in the VSC.

The experiments involved in this chapter are designed to generate shock loading (with a flat-top plateau region, as discussed in Chap. 2). The shock impact experiments presented in this chapter are carried out at different shock strengths, SW1-SW4. Since the reflected shock wave is influenced by sample properties, the strength of the shock wave is defined using incident shock Mach number (M_s) and the corresponding pressure behind the incident shock front, i.e., the peak incident pressure (constant-overpressure).

The experiments carried out in this study are broadly classified into six test cases (graphically described in Fig. 4.3). The primary aim of the experiments is to obtain the pressure signals on the upstream and downstream sides of the sample holder. Initial set of experiments is carried out to understand the role of wire mesh and geotextile as structural facing formwork (test case 1 and 4). Without any granular infill, shock impact test is carried out on the wire mesh (test case 1). The purpose of test case 1 is to examine the influence of the wire mesh alone in attenuating the pressure levels of the incident shock wave. Further, test case 4 is performed to evaluate the effectiveness of the woven geotextile against shock impact loads. Experiments of varying input shock strengths are carried out to investigate the performance of coarse grain sand (CS) as the infill material with the wire mesh as the formwork medium (test case 2). Test case 3 is performed by replacing the coarse grain angular particles (CS) with a uniformly graded smooth glass beads (GB). The combined effect of the particle shape and surface characteristics (roughness) on the barrier is analyzed by comparing the test case 3 with that of test case 2. Finally, experiments are conducted by encapsulating the infill granular materials (CS and FS) in a geotextile lined wire mesh formwork (test case 5 and 6).

All the experiments (test case 1–6) are carried out using nitrogen as the high-pressure gas in the driver section, while driven section is kept at ambient atmospheric conditions. The pneumatic valve is released upon filling the required pressure in the driver section (5/10/20/30 bar), and the corresponding peak incident pressures (in MPa) are 0.071, 0.112, 0.164 and 0.205. Figure 4.4 compares the pressure data


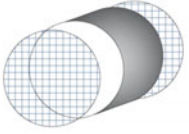
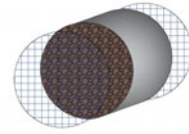
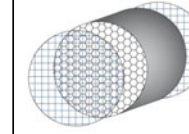

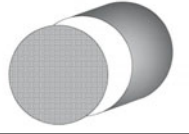
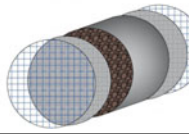
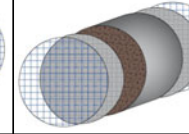
TEST CASE	CASE: 1	CASE: 2	CASE: 3
			
Upstream Face	Wire Mesh (WM)	WM	WM
Downstream Face	Wire Mesh (WM)	WM	WM
Infill Material	BLANK	SAND - CS	GLASS BEAD-GB
TEST CASE	CASE: 4	CASE: 5	CASE: 6
			
Upstream Face	GEOTEXTILE	WM + Geotextile	WM + Geotextile
Downstream Face	-	WM + Geotextile	WM + Geotextile
Infill Material	BLANK	SAND - CS	SAND - FS

Fig. 4.3 Different test cases considered for the test barrier

recorded by upstream pressure transducer P_1 for different shock intensities. A distinct plateau pressure region is observed at the end of the first jump, indicating a constant pressure zone travelling behind the incident shock front. Subsequently, the pressure behind the shock front increases upon reflection at the end wall. Similar pressure profiles will be observed in the transmitted wave on the downstream side of the test sample. The steady (plateau) pressure value at the end of the incident and transmitted wave is used for the calculation of the attenuation coefficient (K_a), given by expression:

$$K_a = \frac{\text{Downstream Pressure behind Transmitted Wave}}{\text{Upstream Pressure behind Incident Shock Wave}}$$

The measurements of the incident pressure behind the shock front allow us to vaguely compare with the ‘peak overpressure’ of the surface-blast wave and relate it to the detonation of a TNT charge at a specific stand-off distance from the target (using Kingery and Bulmash 1984 charts). For instance, a hemispherical surface explosion with a charge of 7 kg of TNT detonating at stand-off distance of 5.82 m from the barrier would generate an incident pressure of 0.112 MPa and reflected pressure of 0.318 MPa; these pressure ranges are comparable with the test condition with Mach number, M_s equal to 1.43 (see Fig. 4.4). Moreover, at farther distances away from the explosion, a Mach stem is expected to form. Hence, the estimated value just gives an approximate TNT equivalent, since the charts were developed for



$$K_a = \frac{\text{Downstream Pressure behind Transmitted Wave}}{\text{Upstream Pressure behind Incident Shock Wave}}$$

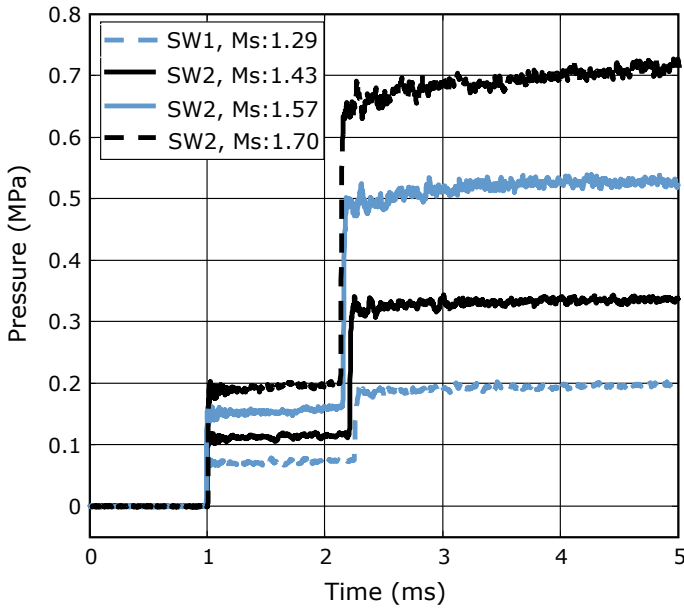


Fig. 4.4 Pressure signals recorded at P_1 of DST, when operated with different driving pressures of nitrogen

hemispherical blast wave front and not for a shock/Mach wave. Further, no exact data or pressure distribution is available behind the Mach stem of a surface explosion.

4.4 Attenuation of Shock Wave Due to Presence of Wire Mesh

The pressure data recorded from the test case 1 are shown in Fig. 4.5. The first jump seen in the upstream side of signal P_2 is the incident shock wave, and the second jump corresponds to the reflected shock wave from the wire mesh. The first jump observed in downstream side of P_4 signal is due to passage of the transmitted shock wave through the wire mesh, and the second jump is due to the reflection from the end wall of the void space chamber. The incident and transmitted Mach number for the wire mesh case is found to be 1.43 and 1.41, respectively. It is observed that the transmitted wave through the mesh is travelling at supersonic velocity ($M_s > 1$). However, depending on the type of barrier, the transmitted wave can be attenuated to a weak shock wave or a subsonic ($M_s < 1$) compression wave (Ben-Dor et al.



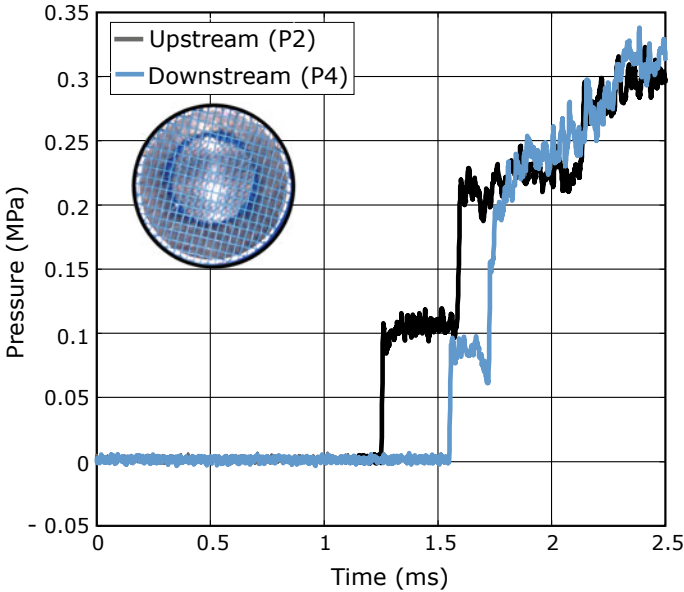


Fig. 4.5 Pressure–time history for test case 1 (wire mesh)

1997; Mazor et al. 1994). Notably, there is a slight drop in pressure between the incident shock and the transmitted shock due to the presence of the mesh. The shock attenuation coefficient (K_a) value is found to be 0.84.

4.5 Attenuation of Shock Wave Through Sand Medium

The pressure traces obtained during a shock impact ($M_S = 1.43$) on sand (CS) barrier (CS) is shown in Fig. 4.6 (test case 2). As expected, the downstream pressure has a different trend when compared to pressure signal of test case 1 (Fig. 4.5). In order to have better representation of the pressure signals, the pressure profiles from all the transducers P_1 – P_4 are plotted in space-time domain (popularly known as x - t diagram), which demonstrates shock propagation phenomena inside the shock tube. The y -axis represents the driven section of the shock tube; the sensors and the sample locations are appropriately scaled and identified on the y -axis. Each division on the y -axis corresponds to a pressure of 1 MPa, and the x -axis corresponds to the time domain in millisecond (ms).

The construction lines (in red) shown in Fig. 4.6 represent the trajectories of the shock waves. The line ab is drawn by connecting the foot of the first jump observed in the pressure profiles of P_1 and P_2 , which corresponds to the passage of the incident shock wave. Upon impinging on the sample, a part of the incident shock wave (ab) gets reflected as reflected shock wave (bc), while the rest of it passes through the

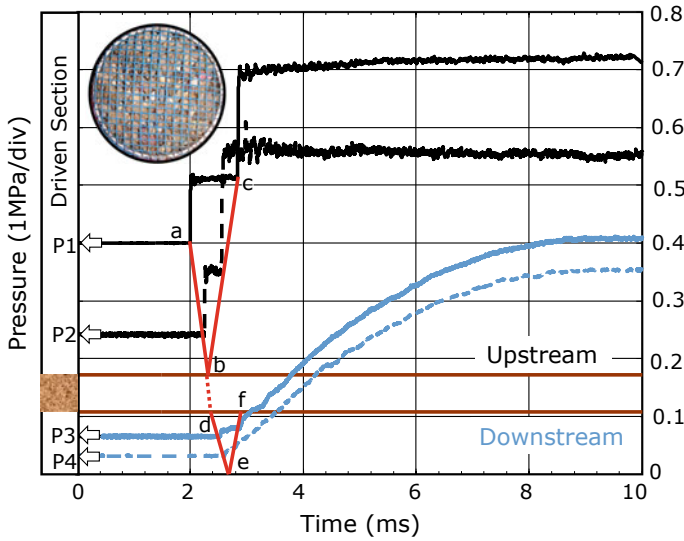


Fig. 4.6 Pressure–time histories recorded at upstream and downstream side for test case 2 (coarse sand)

granular sand media as a transmitted wave (bd). This transmitted wave emerges out on the downstream side as a shock wave/compression wave (de). After reaching the end of the shock tube wall (VSC), the transmitted wave further gets reflected into a reflected transmitted wave (ef). After the second pressure jump on the downstream end (in P_3 and P_4), no further noticeable pressure jumps are observed. However, pressure continues to rise asymptotically (because of gas filtration process) to reach an equilibrium condition (P_e) with the upstream pressure levels. In the present case, the transmitted wave is a weak shock wave with Mach number equal to 1. In the $x-t$ diagram, the angle of incident ray (angle between the incident trajectory path on the sample surface and the line perpendicular to the sample surface at the intersectional point of the incident trajectory) and the transmitted ray is found to be 9° and 18° , respectively. Increase in the angle of the transmitted trajectories indicates the delay in the arrival time of the shock in the downstream end. With the attenuation coefficient value of 0.169, the coarse sand (CS) together with wire mesh has assisted in bringing down the shock pressure levels in the downstream side to about 17% of the incident pressure levels.

In order to consider the effect of particle shape and surface roughness, additional experiments are performed using spherical particles (glass beads–GB). The comparison of pressure profiles recorded at P_3 , with CS and GB as infill material for incident shock strength, M_s equal to 1.43 (test case 2 and 3), is shown in Fig. 4.7. It is observed that the initial pressure rise and plateau region of the GB matches exactly with that of CS. Henceforth, not much of a change is reflected on the K_a value. However, at the rise of the second jump, the pressure signal of GB exhibits slightly higher pressure and gradually isolates from CS. Upon impact load, the granular media is expected to

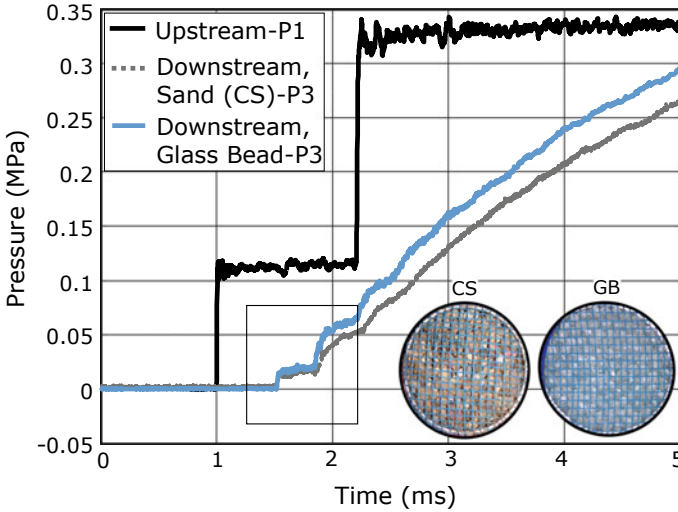
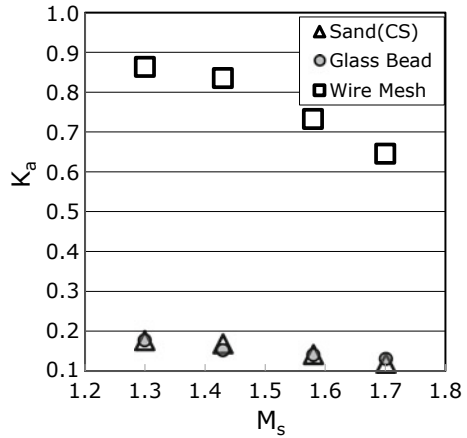


Fig. 4.7 Pressure–time history for test case 2 (coarse sand) and test case 3 (glass bead)

undergo particle breakage and/or tend to relocate with enhanced interlocking. It is reasonable to believe that the shock induced pressure has assisted in the compaction of sand particles to a much denser state. The spherical particles have a lower degree of particle–particle interlock when compared to the angular particles. This effect is characteristically observed at the rise of the second jump shown in Fig. 4.7. The compacted sand (CS) medium impedes the gas flow (travelling behind the shock front) significantly compared to GB, thereby decreasing the downstream pressure and eventually increasing the time to attain the equilibrium pressure (P_e).

The mitigating capability of the infill materials (CS and GB) for varying incident Mach number is shown in Fig. 4.8. The attenuation coefficient value is found to decrease with the increase in the incident Mach number. The glass bead (GB) and coarse sand (CS) have the same effects on K_a even at higher shock strength. It is also evident that the particle shape and roughness have minimum effect on the attenuation behaviour. However, the infill material with angular shape seems to favour particle interlocking and is considered to be more efficient in delaying the gas filtration process. Normally, the delicate targets located on the downstream side of the barrier are expected to withstand a gradual build-up of pressure than a sudden increase in pressure. Hence, the longer the time taken to attain equilibrium pressure, the better is the functional behaviour of the barrier system.

Fig. 4.8 Variation of attenuation coefficient with respect to incident shock Mach numbers



4.6 Shock Wave Interaction with Geotextile Layer

The geotextile fabric is cut into 75 mm diameter samples and is placed on the upstream face of the sample holder. The geotextile is held tight in position by wrapping a strong adhesive tape around the rim of the sample holder. The sample holder is placed at the end of the driven section such that geotextile is facing the incoming shock wave, as shown in Fig. 4.9.

Though the main interest of this section is to assess the geotextile survivability upon shock impact, the downstream pressure levels are also recorded over a larger void space of 120 mm. The pressure profile recorded for the test case 4 with an

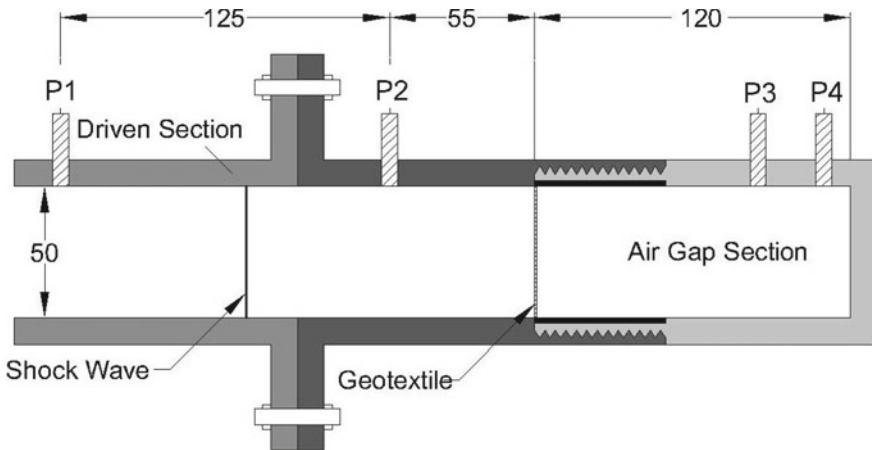


Fig. 4.9 Expanded view of the sample mounting section, applicable to test case 4 (all dimensions are in mm)

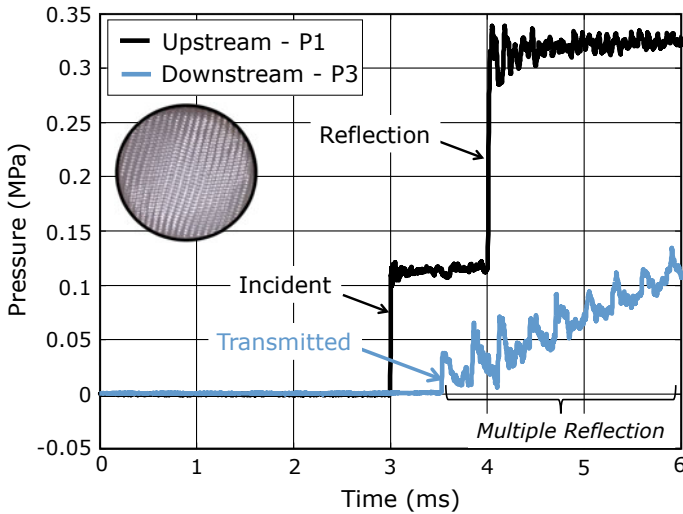


Fig. 4.10 Pressure–time history for test case 4 (geotextile)

incident shock, M_s of 1.43 is shown in Fig. 4.10. A transmitted wave with M_s of 1.17 is formed in the downstream side with an attenuation coefficient of 0.33. In the absence of any kind of obstacle (infill material), the transmitted wave travels further till the end wall. Multiple sharp peaks are observed at the downstream side of the geotextile (signal P_3 of Fig. 4.10), these peaks are due to the repeated reflections between the geotextile layer and the end wall. The amplitude of the spikes becomes smaller with the increase in the number of the reflections. Moreover, if the void space chamber is smaller in length, these reflected shocks (peaks) would have fused together to form a stronger shock on the downstream side. Hence, it is important not to provide any gap between the geotextile and the adjacent infill materials.

Scanning electron microscope (SEM) micrograph images of the geotextile layers are captured before and after the impact of the shock wave, at magnification of $100\times$ (Fig. 4.11a, b). Geotextile layers, on exposure to shock wave with M_s of 1.29, have little or no effect on the strands. While slightly increasing the Mach number to 1.43, geotextile has undergone slight surface deformity. Because of the impact force and the high temperature of the shock wave (around 180°C), the polypropylene strands of geotextile have melted to form globule like structures. Upon further increasing the shock strength to M_s equal to 1.57, the geotextile can no longer resist the high temperature and pressure and thereby it ruptures (Fig. 4.11c). The tensile stress and the flexural rigidity of the geotextile have significant influence on the occurrence of the failure.

From the attenuation coefficient values, it is observed that geotextile by itself appears to be more efficient than the wire mesh. However, because of the low tensile stress and flexural rigidity, geotextile alone cannot be considered a stable formwork. The permeable geotextile fabric together with wire mesh will act as reliable formwork

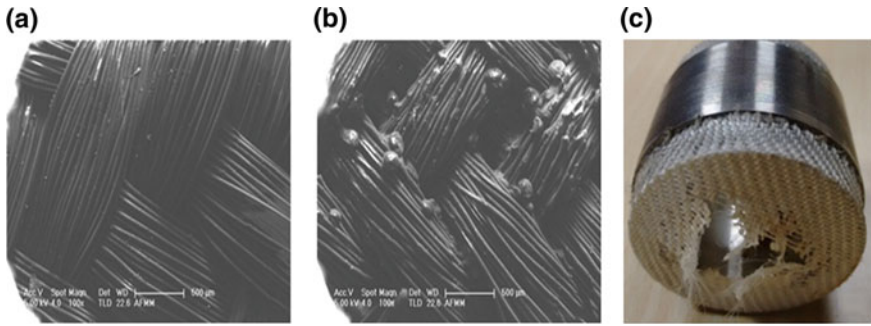


Fig. 4.11 Images of geotextile fabric: **a** SEM images before shock impact, **b** SEM images after shock impact of $M_s = 1.43$ and **c** photograph of ruptured geotextile after shock impact of $M_s = 1.57$

structure for the infill sand particles. Since a fabric like geotextile is considered to be a part of the formwork, extreme care must be taken during the infill material compaction. The formwork should be held in position such that proper contact is ensured between the geotextile and infill materials. Moreover, if there exists any gap (between geotextile and infill material), the pressure level adjacent to the geotextile is expected to amplify (also observed by Hattingh and Skews 2001; Skews et al. 2010)) and the encapsulated barriers will result in low structural stability.

4.7 Influence of Geotextile Layer on the Sand Barrier System

As mentioned previously (Ben-Dor et al. 1997), shock wave impact on granular medium transmits a wave in the granular medium which is followed by two major processes: (i) pore volume compression, pore pressure increases and effective stress transfer take place through particle–particle contact, (ii) gas filtration, where the entrained gas behind the shock wave passes through the pores of the granular medium, overcoming the drag resistance offered by the granular particles.

The downstream pressure profiles for the test cases ($M_s = 1.43$) involving coarse sand barrier (CS), geotextile faced coarse sand barrier (G-CS) and geotextile faced fine sand barrier (G-FS) are summarized in Fig. 4.12. By close inspection of the pressure traces of G-CS, the plateau region of the transmitted wave is still visible. However, the transmitted wave is not considered to be a shock wave (absence of sharp jump) but a compression wave. A delayed filtration process has resulted in a weak compression wave with lower pressure levels when compared to barrier system without geotextile facing. The strength of the transmitted wave further diminishes when the encapsulated barrier is filled with FS. It is evident from the pressure profiles of G-FS that there is a gradual rise in the pressure (without any jump or plateau region), which implies that steady-state gas filtration has taken place through the

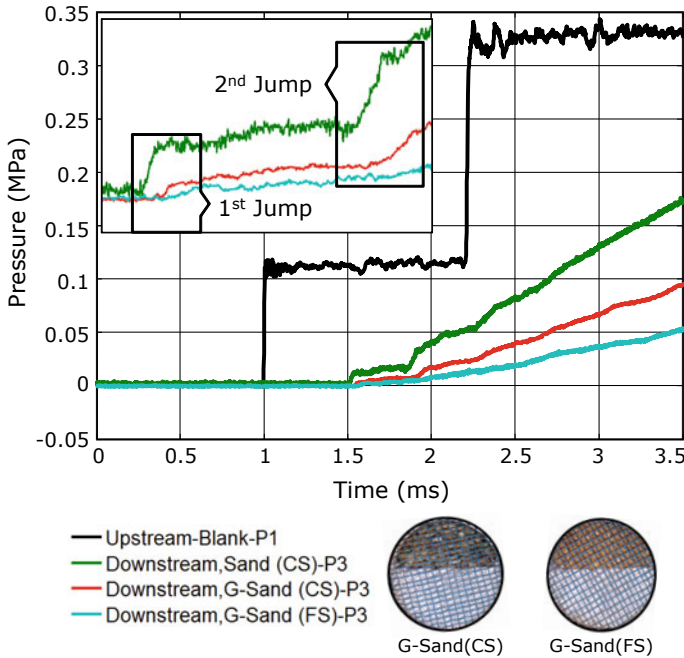
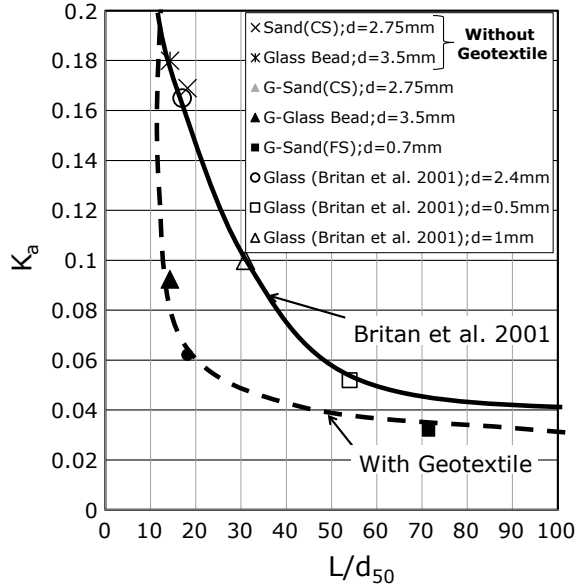


Fig. 4.12 Comparison of pressure signals from test case 2 (coarse sand), test case 5 (geotextile lined coarse sand) and test case 6 (geotextile lined fine sand); Inset figure: magnifies the plot between 1.5 and 2 ms

sand particles. The presence of geotextile layer on FS and CS has also decreased the slope of the quasi-steady pressure rise curve leading towards the equilibrium pressure (P_e).

The K_a value is plotted against a non-dimensional parameter, normalized barrier length L/d_{50} , where L is the length (or thickness) of the sample and d_{50} is the average particle diameter (Table 3.4). The comparison of the experimental results ($M_s = 1.46$) of Britan et al. (2001) on glass particles of different sizes with the results obtained in present study ($M_s = 1.43$) is shown in Fig. 4.13. Though there is a slight variation in the M_s value, one can infer the results for qualitative comparison purpose. The K_a value for the glass beads compares well with that of Britan et al. (2001) value. Let us consider 0.5 mm glass bead infill of Britan et al. (2001), K_a value of 0.05 is reported for a sample of length, $L \approx 108$ mm. By using a geotextile facing on the barrier unit of length 50 mm and with a FS infill ($d_{50} = 0.7$ mm), the coefficient of attenuation is found to be much lower ($K_a = 0.032$). For lower L/d_{50} ratio, the presence of geotextile has reduced the K_a value drastically to about 40–50% to that of the unprotected barrier. The fact that geotextile aids in shock wave attenuation implies that the barrier can further reduce the wall thickness.

Fig. 4.13 Attenuation coefficient versus the normalized barrier length



Furthermore, tests are carried out on the encapsulated barriers by increasing the strength of the shock wave ($M_s > 1.53$). It is observed that single layer of geotextile fabric on the upstream end could not withstand the high temperature and the pressure impact induced by the shock wave (see Fig. 4.14a). Consequently, the infill sand particles are released out of the sample holder through the damaged portion of the geotextile, thereby decreasing the compaction of the infill sand. The wire mesh on

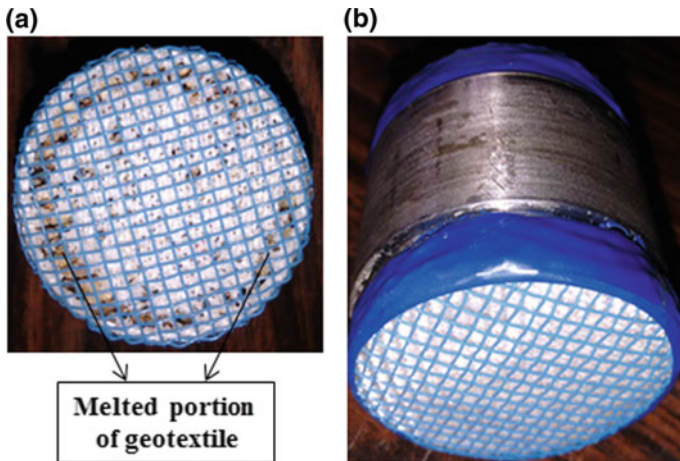


Fig. 4.14 Photograph of geotextile lined coarse sand barrier model after shock impact: **a** upstream side and **b** downstream side

the upstream end has also undergone minor damages at certain intersection joints. However, the geotextile and the wire mesh on the downstream end of the sample seem to be unaffected (see Fig. 4.14b). The geotextile layer on the barrier system has contributed significantly; it primarily serves as a confinement enclosure for the infill granular materials. Geotextile facing prevents the direct contact of the shock wave on the granular particles. The steel wire mesh provides structural stability, while geotextile acts as a shield against the shock wave impact and secondary fragments (such as debris, shrapnel, shattered glass, etc.). Though geotextile is a permeable membrane, it impedes the gas flow to some extent. The flow impedance caused by the geotextile affects the gas filtration process and subsequently decreases the rate at which downstream pressure equilibrates.

In order to assess the stability of the system, series of experiments ($M_s = 1.43$) are carried out by mounting the accelerometer on the supporting formwork. From the experimental results, it is observed that the pressure level of the reflected shock against the upstream face of the barrier is always higher than the incident shock. Hence, it is important to ensure that the upstream supporting formwork of the barrier system can withstand the pressure generated by the reflected shock wave. The shock resistance of the barrier system is evaluated by measuring the displacement-time histories at critical points on the barrier systems. Two accelerometers are installed on the barrier system, one at the upstream face and the other at the downstream face of the formwork. The complete assembly and the positions of the accelerometer are shown in Fig. 4.15a–c. The uniaxial accelerometers are mounted using an adapter, which is then firmly affixed on the wire mesh and the geotextile layer. Accelerometer (A_{us}) on the upstream end is embedded in the infill material, while the accelerometer (A_{ds}) is mounted on the rear end of the barrier system. The presence of the miniature accelerometer (7 mm diameter \times 12.4 mm length, with a mass of about 1.7 g) inside the infill material and the wires extending out of the sample is assumed to have minimal effect.

The acceleration responses are captured at sampling rate of 500 kHz for each of the test case over a period of 4 ms. The acceleration-time histories of test case 5 (G-CS) and test case 6 (G-FS) are shown in Figs. 4.16 and 4.17, respectively. The peak acceleration value and the positive response of the upstream formwork are found to be similar in both the cases. The type of infill granular medium has found to have little effect on the response of upstream formwork. However, the downstream peak acceleration response is found to be higher for coarse sand when compared to fine sand infill.

The displacement response of the system is indirectly obtained by double integration of the recorded acceleration signal. The displacement-time histories for CS and FS infill are shown in Figs. 4.18 and 4.19, respectively. As predicted, the deformation on the upstream end is observed to be larger than the downstream end. The confined sand together with the upstream formwork offers most of the resistance to the impinging shock. The deformation on the downstream end is mainly due to the effective stress transfer through the particles. In order to ascertain that, displacement

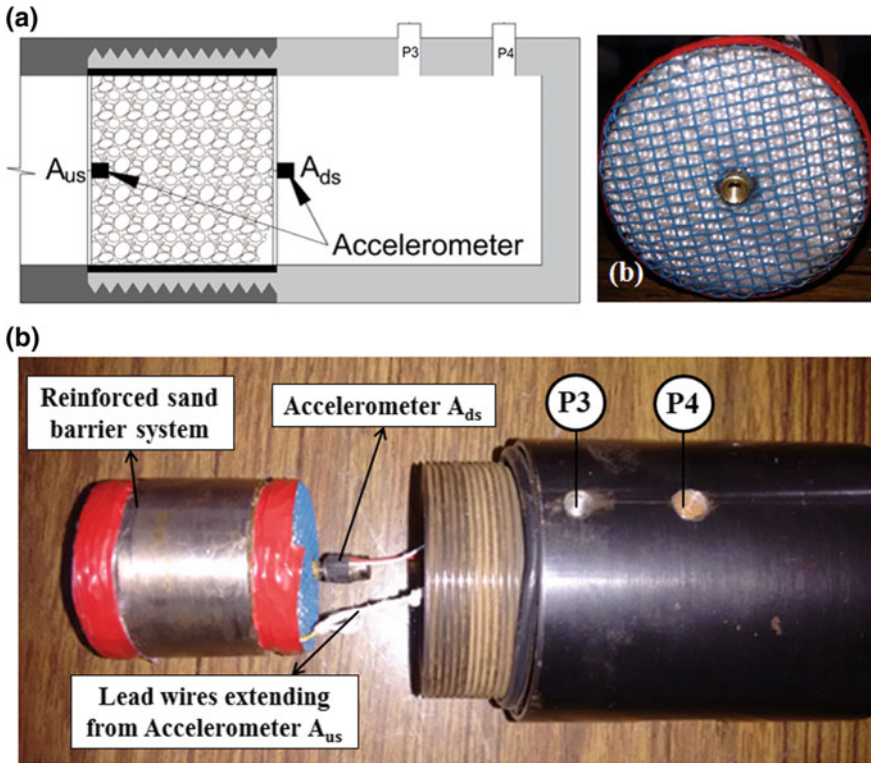


Fig. 4.15 Test section assembly with accelerometers: **a** schematic cross-section showing the location of accelerometer, **b** adapter mounted on the downstream section and **c** overview of the assembly with sample holder

responses are evaluated from the test results of fine sand infill (G-FS). There is a substantial decrease in the displacement on the downstream side when compared to the coarse sand (see Fig. 4.19). This observation is explained with the help of a simple contact stress phenomenon, an illustration of different barrier systems used is shown in Fig. 4.20. When a shock wave impinges on unprotected granular media, contact forces develop between individual particles, and the shock induced stress primarily gets transferred through particle–particle contact (Terzaghi et al. 1996). When compared to the spherical particle, the contact area between the particles is higher for an angular-shaped particle. Increase in the contact area effectively decreases the magnitude of the effective stress. In the case of the fine sand, the small grain particles are suspended within the matrix of fines, and the interacting area with the adjacent particles becomes large. Consequently, the stress induced from the fine sand to the downstream formwork is lower.

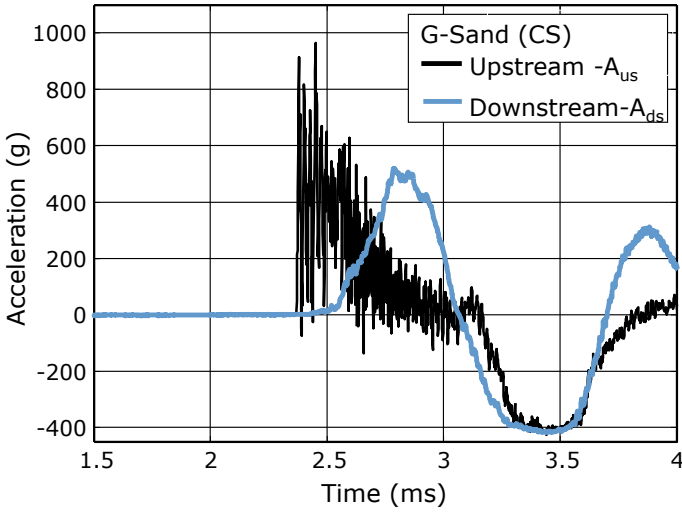


Fig. 4.16 Acceleration-time history for the test case 5, geotextile encapsulated barrier system with coarse sand infill material

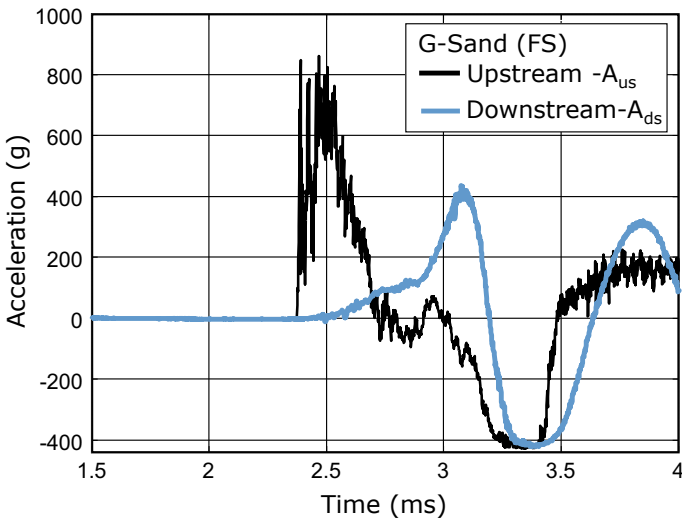


Fig. 4.17 Acceleration-time history for the test case 6, geotextile encapsulated barrier system with fine sand infill material

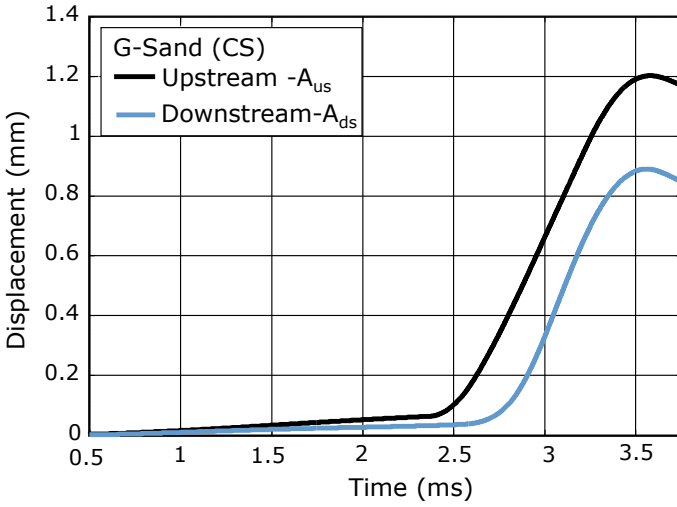


Fig. 4.18 Displacement-time history for the test case 6, geotextile encapsulated barrier system with coarse sand infill material

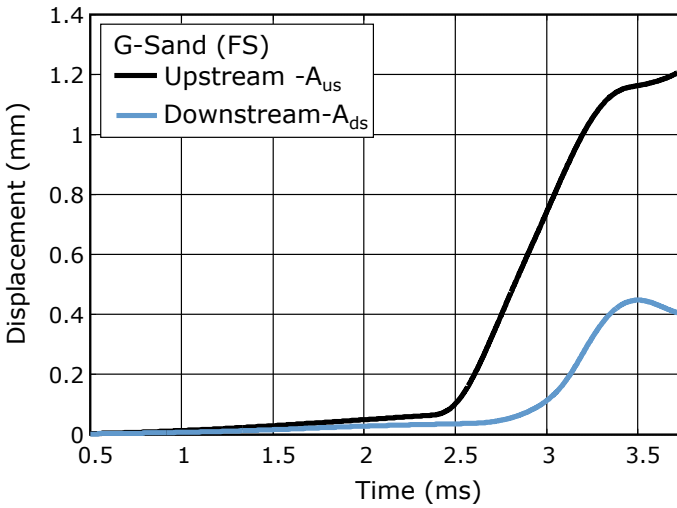


Fig. 4.19 Displacement-time history for the test case 6, geotextile encapsulated barrier system with fine sand infill material

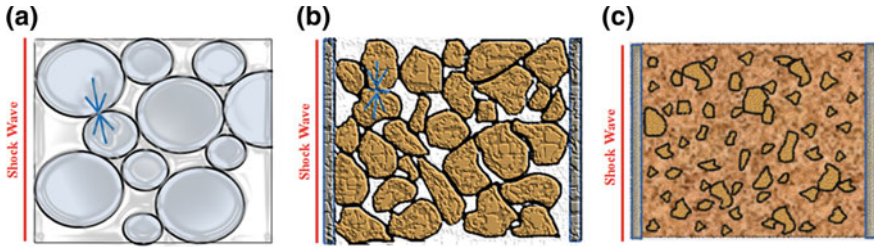


Fig. 4.20 Illustration of particle arrangement in different barrier systems: **a** glass bead barrier (GB), **b** geotextile faced coarse sand barrier (G-CS) and **c** geotextile faced fine sand barrier (G-FS)

4.8 Summary

The present chapter has demonstrated that the effectiveness of using shock tube is analyzing the attenuating property of the granular material-based barrier system. The shock tube experiments were performed at different shock strengths, Mach numbers ranging from 1.29 to 1.7. The barrier system performance is analyzed using coarse and fine sand as infill materials with and without geotextile facing. The attenuation coefficient value, K_a is found to be higher for coarse sand when compared to fine sand, lower the K_a value higher is the attenuation. The shape of particle has least influence on the attenuation coefficient. The contribution of geotextile reinforced sand barrier as a protective system against shock waves is also discussed. The primary function of the geotextile is to provide a formwork along with the wire mesh for the infill granular materials. In addition to this, geotextile prevents the direct contact between the shock wave and the sand particles, thereby reducing the magnitude of the stress transfer. The presence of the geotextile has significantly reduced the gas pressure exiting the encapsulated barrier and also decreased the rate at which downstream pressure equilibrate (P_e). On the basis of the results obtained from this study, a geotextile encapsulated barrier system can be designed with appropriate infill material for an optimized thickness, thereby offering an efficient protection system against shock loads. Some of the key observations from the experimental study are listed below.

1. Attenuation coefficient (K_a) values decrease with decrease in the particle size, and there is found to be no significant effect on the attenuation coefficient due to particle shape and surface roughness. However, angular-shaped sand particle has prominent role in delaying the P_e compared to spherical particle.
2. K_a value alone is not sufficient to decide on system performance; it also depends on the rate at which downstream pressure equilibrate.
3. A lower attenuation coefficient and gradual pressure rise can easily be achieved by using a geotextile layer on a granular medium instead of using sand column of large thickness.
4. For shock wave with the M_s greater than 1.57, there was evidence of damages to geotextile layer, and the SS wire mesh was disconnected at few locations. The deformation level of the wire mesh and intact state of the geotextile at the rear

end is noteworthy. However, the failure of the barrier system can be considered to be a non-debris and ductile. Hence, the reinforced geotextile sand barrier finds effective use in low shock ranges ($M_s < 1.5$). Nevertheless, these systems can still be operated at such vulnerable conditions by reinforcing the protective screen with higher tensile strength and heavy-duty geotextiles.

A simple laboratory-scale experiment with shock tube operating at low Mach number regime will suffice to characterize the shock-barrier interaction. This experimental technique provides the shock wave attenuation data based on the pressure—time history and would further help in designing better protective shields against shock loading. The studies presented herein have been successful in performing laboratory test to understand the fundamental behaviour of blast protective wall system in laboratory conditions. This present study is to be further extended considering the scaling laws with the actual field size wall systems. Further experiments are to be carried out to assess the dependency on the degree of water saturation upon exposure to shock waves.

References

- Afzali-Nejad A, Lashkari A, Shourijeh PT (2017) Influence of particle shape on the shear strength and dilation of sand-woven geotextile interfaces. *Geotext Geomembr* 45(1):54–66
- Athanasopoulos GA (1993) Effect of particle size on the mechanical behaviour of sand-geotextile composites. *Geotext Geomembr* 12(3):255–273
- Bathurst RJ, Vlachopoulos N, Walters DL, Burgess PG, Allen TM (2006) The influence of facing stiffness on the performance of two geosynthetic reinforced soil retaining walls. *Can Geotech J* 43(12):1225–1237
- Ben-Dor G, Britan A, Elperin T, Igra O, Jiang JP (1997) Experimental investigation of the interaction between weak shock waves and granular layers. *Exp Fluids* 22(5):432–443
- Britan A, Ben-Dor G, Elperin T, Igra O, Jiang JP (1997) Gas filtration during the impact of weak shock waves on granular layers. *Int J Multiph Flow* 23(3):473–491
- Britan A, Ben-Dor G, Igra O, Shapiro H (2001) Shock waves attenuation by granular filters. *Int J Multiph Flow* 27(4):617–634
- Britan A, Shapiro H, Ben-Dor G (2007) The contribution of shock tubes to simplified analysis of gas filtration through granular media. *J Fluid Mech* 586
- Engelbreten T, Bakken J, Hansen EWM, Lysberg I (1996) Shock waves and gas flow through granular materials. In: *Proceeding workshop explosion effects in granular materials, Norway, Oslo*, pp 111–131
- Hattingh TS, Skews BW (2001) Experimental investigation of the interaction of shock waves with textiles. *Shock Waves* 2:115–123
- Heffernan PJ, Moyle CC, Wight RG, Scherbatuk KD (2006) The effectiveness of textile barriers to attenuate blast wave ingress into buildings. In: *Proceedings of 1st international structural specialty conference, Canadian Society for Civil Engineering, Calgary, Canada*, pp 1–8
- Hesco (2010) HESCO Bastion concertainers. <http://www.hesco.com/>
- Hong Y-S, Wu C-S, Yu Y-S (2016) Model tests on geotextile-encased granular columns under 1-g and undrained conditions. *Geotext Geomembr* 44(1):13–27
- Kingery CC, Bulmash G (1984) Air blast parameters from TNT spherical air burst and hemispherical surface burst. Defence technical information center, Ballistic Research Laboratory, Aberdeen proving ground, Maryland, USA, Report BRL, 02555

- Koerner RM, Soong T-Y (2001) Geosynthetic reinforced segmental retaining walls. *Geotext Geomembr* 19(6):359–386
- Koerner RM, Wilson-Fahmy RF, Narejo D (1996) Puncture protection of geomembranes part III: examples. *Geosynth Int* 3(5):655–675
- Lee KM, Manjunath VR (2000) Soil-geotextile interface friction by direct shear tests. *Can Geotech J* 37(1):238–252
- Ling HI, Leshchinsky D, Tatsuoka F (2003) Reinforced soil engineering—advances in research and practice. Marcel Dekker, Newyork
- Lv H, Wang Z, Li J (2017) Experimental study of planar shock wave interactions with dense packed sand wall. *Int J Multiph Flow* 89:255–265
- Mazor G, Ben-Dor G, Igra O, Sorek S (1994) Shock wave interaction with cellular materials. *Shock Waves* 3(3):159–165
- Narejo D, Koerner RM, Wilson-Fahmy RF (1996) Puncture protection of geomembranes part II: experimental. *Geosynth Int* 3(5):629–653
- Ng CC, Chew SH, Karunaratne GP, Tan SA, Loh SL (2000) Flexible and rigid faced MSE walls subject to blasting. In: *Advances in transportation and geoenvironmental systems using geosynthetics*, American Society of Civil Engineers, Reston, VA, pp 322–336
- Pieri RL (1998) Using reinforced earth walls for blast mitigation. Ph.D. thesis, University of Florida
- Rose TA, Smith PD, Mays GC (1998) Protection of structures against airburst using barriers of limited robustness. *Proc Inst Civ Eng Struct Build Thomas Telford ICE Virtual Libr* 128(2):167–176
- Sapko MJ, Hieb MR, Weiss ES, Zipf RK, Harteis SP, Britt JR (2009) Passive mine blast attenuators constructed of rock rubble for protecting ventilation seals. SME (Society for Mining, Metallurgy & Exploration Inc.) Annual meeting and exhibit and CMA's 111th national western mining conference proceedings
- Scherbatiuk K, Rattanawangcharoen N (2008) Experimental testing and numerical modeling of soil-filled concertainer walls. *Eng Struct* 30(12):3545–3554
- Skews BW, Bugarin S, Sawicka E (2010) Surface pressure effects from shock wave impact on inclined and curved clothing. *Int J Impact Eng* 37(3):231–241
- Smith P (2010) Blast walls for structural protection against high explosive threats: a review. *Int J Prot Struct* 1(1):67–84
- Terzaghi K, Peck RB, Mesri G (1996) *Soil mechanics in engineering practice*. Wiley-Inter Science Publication, New York
- van-der Grinten JGM, Van-Dongen MEH, van-der Kogel H (1985) A shock-tube technique for studying pore-pressure propagation in a dry and water-saturated porous medium. *J Appl Phys* 58(8):2937–2942
- Vangla P, Latha MG (2016) Effect of particle size of sand and surface asperities of reinforcement on their interface shear behaviour. *Geotext Geomembr* 44(3):254–268
- Yogendrakumar M, Bathurst RJ (1992) Numerical simulation of reinforced soil structures during blast loads. *Transp Res Rec* 1336:1–8
- Zhiwei H (2009) Geosynthetics structures subject to blast load. Ph.D. thesis, National University of Singapore

Chapter 5

Granular Material Responses to Air-Blast Wave Loading



5.1 Introduction

From the previous chapter, it was proved that sand is an excellent energy absorbent material and is efficiently used as protective barriers against sudden impact and blast loadings. Sand barrier-retaining walls and steepened slopes are often used in military and civilian applications to protect personnel and property against blast and ballistic loads. Sand deposits in the forms of sand bags are also used around the trenches and bunkers which act as a attenuating medium and form a fortification and a base for underground storages against possible air strikes (Scherbatiuk and Rattanawangcharoen 2011; Smith 2010). Regardless of the fortification material, the roof surface of the bunkers is generally covered with a layer of sand or sand bags, intended for shock absorption as shown in Fig. 5.1. In certain cases, the entire bunker will have sandbagged roof. Sand layer is also used as a base isolation system, to mitigate the ground shock effects on structures resulting from the blast loads (Wu et al. 2004).

An air-blast is an explosion when an explosive is detonated in air at a sufficient altitude above the ground surface. Air-blast explosions generate radially expanding shock waves; the resulting overpressure can impart significant damage to the structures and people on the ground surface. The magnitude of the blast effect is influenced by the height of the burst and the weight of the charge. At smaller scale, an air-blast event can be a case when an explosive is detonated in a vehicle located above the ground surface. It can also be carried out on a massive scale, explosive loaded shells, and bombs are dropped using aircraft such that they detonate in the air. During such an event, detonation energy will spread over a large surface area causing maximum destruction.

An air-blast explosion (near-surface) involves three significant phases (Whitman 1970):



Fig. 5.1 Artistic impression of the bunker built using sand bags

- (i) Crater formation on the target surface.
- (ii) Generation of an air-blast wave which sweeps outward over the surface.
- (iii) Generation of surface ground motion and stress waves within the soil deposit.

The present chapter will focus on the effect of air-blast wave pertinent to stress waves and vibrations in the sand media.

5.2 Previous Studies on Air-Blast Impact on Granular Medium

Very little is known about the dynamic response of sand during air-blast impact loading. However, numerous studies have been reported on the dynamic behaviour of soil, when subjected to underground and surface-blast conditions. Among them, a few relevant papers, which discuss the propagation of dynamic wave in the surrounding soils, are listed: Alekseenko and Rykov (1972), William and Robert (1975), Drake and Little (1983), TM5-855-1 (1986), Rinehart and Welch (1995), Roy (1998), and Wu et al. (2003). Several empirical relations are also available (Baker 1973; Kinney and Graham 1985; Smith and Hetherington 1994), which have been developed based on field experiments and numerical simulations. These equations help us to predict parameters like peak soil pressure (PSP) and peak particle velocity (PPV) as a function of buried explosive mass and distance. A well-known reference TM5-855-1 (1986), which is widely used for prediction of ground shock parameters, recommends

the following equation for dry sand with low relative density (*note: units are in FPS system*).

$$\text{PSP} = 1920 f \left(\frac{R}{W^{1/3}} \right)^{-3.0} \quad (5.1)$$

$$\text{PPV} = 160 f \left(\frac{R}{W^{1/3}} \right)^{-3.0} \quad (5.2)$$

where ‘ R ’ is distance from source, ‘ W ’ is charge weight, ‘ f ’ is the coupling factor and the exponent term is termed as attenuation coefficient (k). The ‘ k ’ value predicted for the PPV for the buried-blast condition in case of dry loose and dense sand deposit is reported to be 3 and 2.5, respectively (Leong et al. 2007).

Only a few literatures are available which determine the effect of explosion in air on the soils. Ambrosini et al. (2002) conducted a series of field experiments with TNT charges of 1, 2, 4, 7 and 10 kg at 0.5 m and 1 m above the ground level. The aim of the experiment was to address phase (1) of air-blast; the crater dimension is quantified for specific air-blast and compared with the empirical relations (Kinney and Graham 1985). The craters belonging to air-blast were observed to be significantly smaller compared to the craters produced by the explosions at ground level or underground. Busch et al. (2015) conducted similar small-scale experiments on a clayey soil deposit using TNT weight ranging from 0.9 to 100.9 g. Seismograph signals obtained from the buried geophones and air-blast sensors were used to obtain a relationship for ground vibration and crater dimension, with the explosive mass and distance from the ground surface. The above-mentioned studies have primarily focused on impact crater formation, and information available on the ground vibration is very much limited to cohesive soil deposit. Moreover, no results were given on the shock pressure attenuation and stress distribution in the soil during blast impact.

One of the earliest attempts was made by Akai et al. (1972) to investigate the stress response of soils due to shock loading using shock tube. The attenuation of peak stress in confined sandy loam indicated an exponential decay. van-der Grinten et al. (1985) too observed similar behaviour of pressure amplitudes in dry and wet sand media. Sniekers et al. (1989) and Smeulders and van Dongen (1997) carried the work forward in further understanding the pressure wave propagation in water-saturated, partially saturated and dry sand samples. Ben-Dor et al. (1997) performed few experiments on sand samples; the rise in the pressure is attributed to two phenomena, compaction of the granular particle due to the shock impact followed by gas filtration, which affects the particles by the drag forces between the solid and gaseous phases. In most of the studies mentioned above (and in previous chapter), pressure pulse generated by shock tube has constant pressure zone behind the shock front. And the impulse generated will be significantly different from that of a blast wave. Blast wave impulses depend not only on the peak overpressure and the duration of the wave, but also on the rate of decay of the overpressure (Kinney and Graham 1985). Overall, these studies provide limited information on the attenuation performance of sand medium with reference

to air-blast. In addition to shock pressure attenuation, further investigation on air-blast is necessary to obtain vibrational response parameters, such as peak particle acceleration (PPA), peak particle velocity (PPV) and the strain induced in the sand medium.

5.3 Shock Tube Simulated Air-Blast Experimental Series

This chapter provides insight into the spatial distributions of particle velocity and pressure over the depth of the sand specimen impacted by blast waves. The following sections will provide some quantitative information regarding the magnitude of shock pressure and vibrational amplitudes in loose and dense sand deposits. The above aspects are addressed in three sections: propagation and attenuation of stress waves, acceleration and velocity response of sand particles and dynamic strains induced in sand deposits. To gain a better understanding of the responses over a different blast intensity, shock tube experiments are conducted by varying (by using different diaphragms) the TNT equivalent explosion on different sand deposits (loose and dense).

The experimental setup is broadly categorized into three major sections. The foremost being the shock tube, the second part of the setup includes the test chamber which is filled with test sample. And finally, the setup is incorporated with appropriate instrumentation system, which includes both contact- and non-contact-based measurement techniques. Air-blast wave is simulated using vertical shock tube facility.

5.3.1 Test Chamber and Instrumentation

The outlet of the driven section of the shock tube is connected to the test chamber which is enclosed in the dump tank. The cross-sectional and plan view of the test chamber is shown in Fig. 5.2a, b, respectively. The test chamber is a square-shaped steel chamber of size of 250 mm \times 250 mm, 225 mm in depth, with a wall thickness of 15 mm. To avoid wave reflections from the chamber walls, adjacent sides and the bottom face of the test chamber are provided with 10-mm-thick rubber padding (Fig. 5.3a). These padded rubbers are expected to have lower impedance value (product of density and wave velocity in the medium) when compared to mild steel.

Dry river bed sand is used to prepare the test specimen. The properties of fine sand used for sample preparation are described in Chap. 3. A sand test specimen of 200 mm \times 200 mm \times 200 mm is prepared using sand pluviation technique. The sand pluviation technique is used to generate test sample of constant relative density (RD). In the present study, two sand deposit test specimens are prepared, namely loose and dense sand deposits with relative densities of 45% and 73%, respectively.

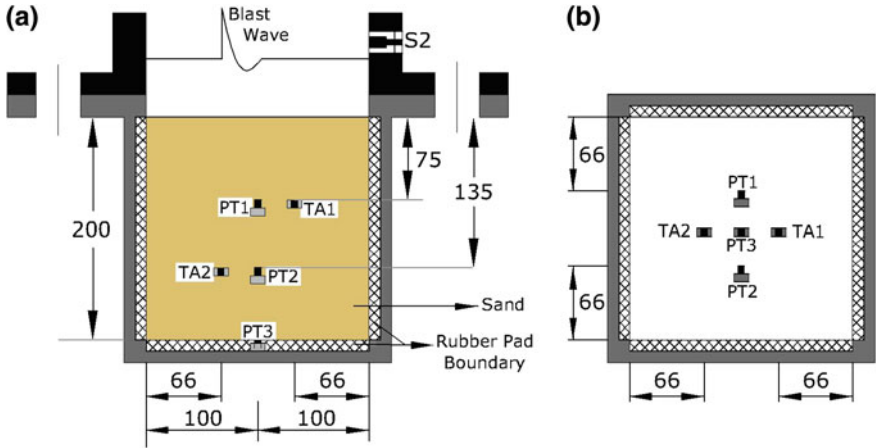


Fig. 5.2 Schematic diagram the test chamber used in VST: **a** sectional view of test chamber and **b** top view of test chamber

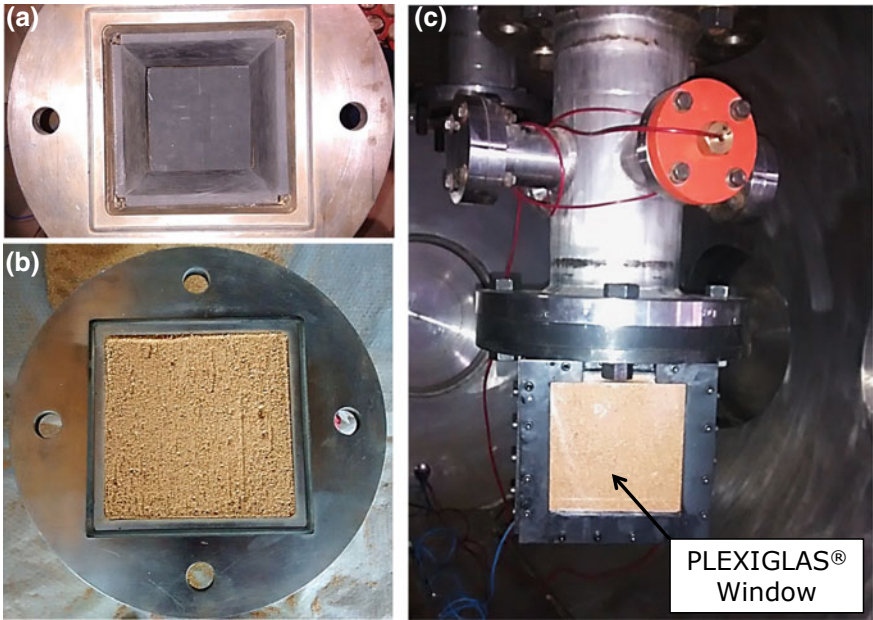


Fig. 5.3 A photograph of the test chamber: **a** an empty test chamber with the rubber padding walls; **b** test chamber filled with sand with surface levelled; **c** a view of the test chamber mounted at the end of VST, assembled for DIC

The photograph of the test chamber with the sand deposit is shown in Fig. 5.3b. For the test case which involves digital image correlation technique, one of the side walls of the test chamber is replaced with a 30-mm-thick Plexiglas® window, which will facilitate in visualizing and recording the sand particle movements (Fig. 5.3c).

Three piezoelectric pressure transducers—PT1, PT2 and PT3—and two triaxial accelerometers—TA1 and TA2—are mounted inside the test chamber. In addition to it, two additional pressure transducers, S_1 and S_2 , are flush-mounted on the inner wall of the driven section in the shock tube. These sensors help us to capture the pressure profiles of the blast wave and also help in measuring the speed of the shock front. The location of sensors is shown in Fig. 5.2a. The TA is mounted such that the y -axis of the sensor is aligned vertical along the shock tube axis. The TA is used to distinguish blast wave-induced vibrational activity in the lateral (x - z -axis) and longitudinal directions (y -axis). Piezoelectric pressure transducers (PT) are used to measure the dynamic pressure caused due to the stress waves. The wave propagation in the sand deposit is assumed to be symmetric along the shock tube axis, and hence, each pair of sensors (PT and TA) is located at depth of 75 and 135 mm from the top surface of the sand bed (shown in sectional view in Fig. 5.2a). PT and TA are located at a distance of 66 mm (one-third of sample dimension) from the side wall of the test chamber (shown in top view in Fig. 5.2b). A third pressure sensor PT3 is located at the bottom, centre of the test chamber. The pressure transducers PT1–PT3 record pressure, resulting from both the solid phase (stress transfer through particles) and the gaseous phase (entrained gas). PT and TA transducers are simultaneously triggered by a signal from S_2 sensor, which is closest to the surface of the sand bed (0.6 m away). Yokogawa's ScopeCorder is used to acquire accelerometer and pressure data at a sampling rate of 100 kHz.

5.3.2 Digital Image Correlation (DIC) System

The fast rate deformation of the sand specimen during the blast impact is analysed through a series of high-speed images using digital image correlation method. Digital image correlation (DIC) is an optical-based experimental technique that uses photographic images to determine the response of a system. ARAMIS-GOM (GOM mbH, 2009), a commercial software, is used for the DIC analysis in the present study. The photograph of the test chamber with one of the side walls having a Plexiglas® window is shown in Fig. 5.3c.

Phantom V310 high-speed camera is used to capture high-speed images. The line of sight of the camera is aligned perpendicular to the side wall of test chamber, and the target area is illuminated with a tungsten-halogen light source. For the DIC program to track the deformation, the target is generally painted with a speckle pattern. In the present study, the randomly arranged sand particles act as 'pseudo-speckle' pattern (Fig. 5.4a). Upon blast impact, the pseudo-sand speckle pattern undergoes transformation which is captured by high-speed camera. The DIC method allows us to determine the displacement of a point on the surface by comparing the initial and

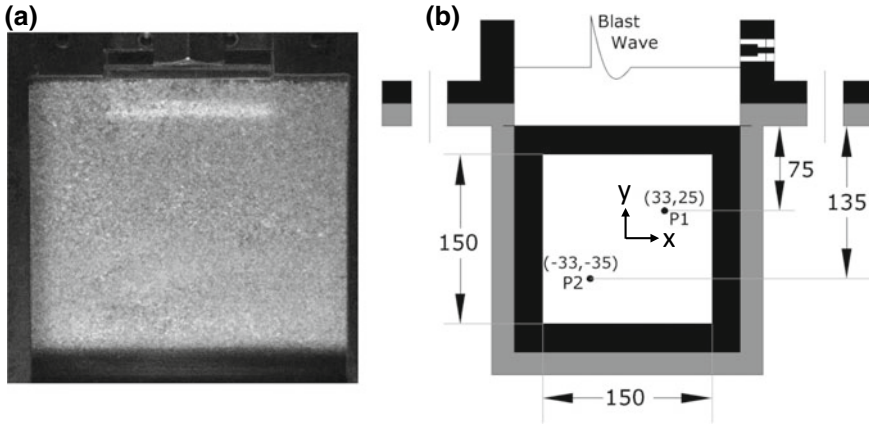


Fig. 5.4 DIC setup: **a** pseudo-speckle pattern generated by sand particles and **b** schematic diagram of the front face of test chamber with Plexiglas window

subsequent successive images of the same point acquired during the experiment. By cross-correlation procedure, the entire image (150×150 mm) is analysed to obtain a point-wise displacement and strain field. In Fig. 5.4b, two reference points, P_1 and P_2 , are identified on the glass window. The absolute displacement of these two coordinate points is monitored. The location of P_1 and P_2 corresponds to the projection of transducers TA1 and TA2 on the window pane, which would help us to validate DIC results against the physical measurement data.

The high-speed camera is triggered by a signal from S_2 sensor. A series of images are recorded at 12,000 frames per second at an exposure of $82 \mu\text{s}$. All the images are captured with a resolution of 480×480 pixels. A total of 100 sequential images captured during the test time are selected for image analysis.

5.3.3 Blast Wave Characterization and Experimental Test Program

The shock tube is operated by using high-pressure compressed helium gas in the driver section (0.5 m) and air at atmospheric pressure in the driven section (4.5 m). Three different aluminium diaphragms are used, having thicknesses of 5 mm, 4 mm and 2 mm with groove depth of 2 mm, 1 mm and 0.4 mm, respectively. The blast wave profile evolved at the exit of the shock tube for a typical case with a 4 mm-1 mm (4-mm-thick diaphragm with a 1 mm deep v -groove) is shown in Fig. 5.5.

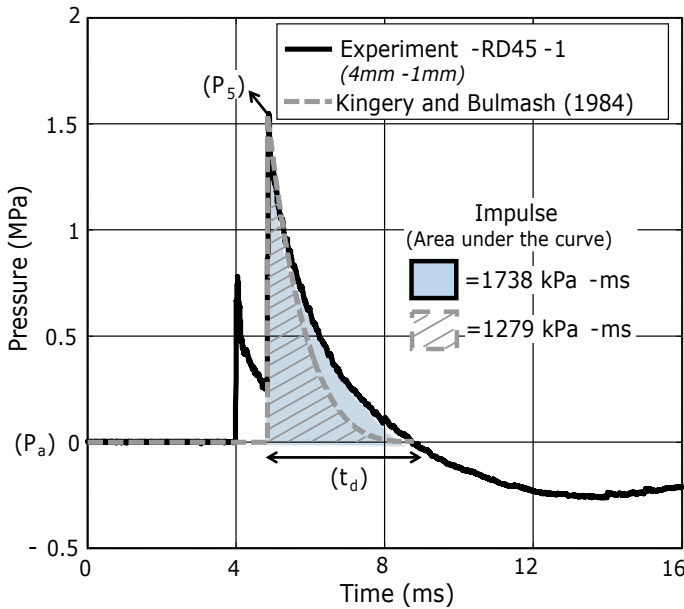


Fig. 5.5 Typical blast wave profile generated from VST, using a 4 mm–1 mm diaphragm

5.3.3.1 Blast Wave Characterization

The two significant blast parameters are identified of the blast wave generated from the shock tube, namely ‘peak-reflected overpressure’ and ‘positive time duration’. Positive impulse (area under the positive phase) is indirectly represented by peak overpressure and positive time. For all the test cases in the present study, peak-reflected pressure (P_5) is considered as peak pressure value of the second jump, and the positive phase duration (t_d) is the time taken for the reflected pressure (second jump) to decay to the atmospheric pressure levels (P_a). Further, the impulse is determined by calculating the area under the pressure–time curve (shaded portion in Fig. 5.5) over the positive phase duration (t_d). The blast wave parameters obtained from the shock tube are expressed in terms of equivalent charge weight of TNT (W) detonating at an altitude (H) using Kingery and Bulmash (1984) chart and coefficients of Shin et al. (2015). The procedure adopted for the estimation of equivalent TNT explosion in terms of scaled blast distance (Z) is discussed earlier in Chap. 3.

Let us consider the blast parameters obtained from the typical blast wave shown in Fig. 5.5 of test case RD45-1, $P_5 = 1.547$ MPa, $t_d = 3.931$ ms and $I = 1738$ kPa ms. A value of Z equal to 1.52 is predicted from peak-reflected polynomial function (Appendix A) for a peak overpressure value of 1.547 MPa. For the predicted Z value, unique values of W (54.15 kg) and H (5.75) are obtained, such that positive phase duration polynomial function yields the same time duration value as obtained from the shock tube ($t_d = 3.931$ ms). Figure 5.5 also shows a dashed line curve

Table 5.1 Shock tube blast parameters with corresponding TNT equivalents

Input values	Diaphragm type	Shock tube blast parameters		Equivalent TNT spherical charge		
		P_5 (MPa)	t_d (ms)	W (kg)	H (m)	Z (m/kg ^{1/3})
Test no.						
RD45 series: relative density of 45% with impedance^a of 177.82 kPa s/m						
RD45-1	4 mm–1 mm	1.547	3.931	54.15	5.75	1.520
RD45-2		1.549	3.949	54.99	5.78	1.520
RD45-3	5 mm–2 mm	1.428	4.161	60.51	6.12	1.559
RD45-4		1.371	3.865	44.61	5.60	1.579
RD45-5	2 mm–0.4 mm	0.755	2.951	11.3	4.30	1.916
RD45-6		0.745	3.343	16.61	4.90	1.920
RD45-7	5 mm–2 mm	1.389	3.980	50.74	5.82	1.572
RD73 series: relative density of 73% with impedance^a of 206.67 kPa s/m						
RD73-1	4 mm–1 mm	1.487	3.384	33.64	5.00	1.549
RD73-2		1.62	3.391	37.13	5.00	1.499
RD73-3	5 mm–2 mm	1.402	4.248	61.23	6.18	1.568
RD73-4		1.46	3.946	49.23	5.65	1.542
RD73-5	2 mm–0.4 mm	0.731	2.614	9.56	4.10	1.932
RD73-6		0.783	2.881	10.98	4.20	1.890
RD73-7	5 mm–2 mm	1.420	4.042	54.75	5.93	1.561

^aImpedance = product of density and wave velocity in the medium

which represents the blast wave profile obtained from the Kingery and Bulmash (1984) empirical charts, which correspond to an explosion of 54.15 kg of TNT at distance of 5.75 m. It should be noted that for this particular combination of Z and H , only the peak pressure and positive time duration match exactly, and the impulse generated by shock tube is found to be slightly higher than the values predicted by the empirical charts.

The above described procedure is repeated for various other test cases with different set of diaphragms (5 mm–2 mm and 2 mm–0.4 mm). The shock tube blast parameters along with their equivalent spherical TNT charge weights for different test cases are listed in Table 5.1. Further, it is to be noted that the peak-reflected overpressure value is influenced by the density of the target material. And hence, for the same test conditions, the Z value is found to be different for test case with sand specimens of RD45 and RD73.

5.3.3.2 Experimental Program

The shock tube experiments are performed on two types of sand deposits, loose (RD45) and dense (RD73) samples. Based on the intended measurements, experiments are carried out in three stages:

- (1) Propagation and attenuation of blast-induced stress waves are analysed using the signals recorded from pressure transducers; a total of 15 set of experiments were carried out for each density case (RD45 and RD73), and six test run data are identified for each specimen (RD45-1 to 6 and RD73-1 to 6) with similar repeatable conditions.
- (2) Vibration and particle motion are measured using embedded triaxial accelerometers; only two sets of data belonging to different scaled distance ranges are available for loose (RD45-1,2 and RD45-5,6) and dense (RD73-1,2 and RD73-5,6), and rest of the test results were failed to trigger the accelerometer, or the contact wire of the accelerometer was damaged during the impact.
- (3) The strain induced in loose and dense sand deposits is estimated using 2D-DIC system using two sets of experiments for each density case (RD45-7 and RD73-7).

It is seen from Table 5.1 that the scaled distance (Z) value of air-blast is different for loose and dense deposits. Hence, the experimental results are analysed by categorizing them into two groups based on the range of Z values, $Z = 1.52$ to 1.58 and $Z = 1.89$ to 1.93 .

5.4 Air-Blast Wave-Induced Stress Wave

This section presents the results of the experiments involving the measurement of stress (pressure) waves in sand medium. The summary of the test results recorded from the shock tube experiments is listed in Table 5.2.

Two typical waveforms are illustrated in Figs. 5.6 and 5.7 for loose (RD45-1,2) and dense (RD73-1,2) sand deposits, respectively. Two experimental test results are plotted to show the repeatability of signals achieved. The pressure–time history data are recorded from ‘in-sand’ pressure transducers (PT1–PT3). The figures also show pressure signal recorded ‘in-air’ by transducer S_2 , which is the closest port available from the sand surface, and the signal recorded on S_2 may be regarded as the applied blast loading.

Referring to pressure profiles in Figs. 5.6 and 5.7, the stress wave induced in the sand is characterized by the presence of instantaneous jump, and thereafter, the pressure is gradually increased to a peak value and then decreased immediately, which is followed by undular jumps reducing the pressure levels to atmospheric values. As mentioned earlier, the pressure transducers embedded in the sand deposit measure both the stress transferred through the solid particles and the static pressures in the gaseous phase. Upon blast wave impact, the energy is released in the sand medium as either a stress wave or a shock wave depending on the intensity of the blast and the impedance of the medium. During the passage of a stress wave, compression occurs, which causes a steep rise (jump) in pressure. The leading stress wave is followed by a turbulent gas flow. The gas permeates through the pores in sand medium, which is responsible for the gradual pressure rise to the peak and then decreases over a period

Table 5.2 Summary of the wave propagation results for loose and dense sand deposits

Output values	Peak pressure (in-sand), P_d			Propagation velocity
Test case	d_1 (MPa)	d_2 (MPa)	d_3 (MPa)	V_p (m/s)
<i>RD45 series: loose sand</i>				
RD45-1	9.83	4.21	1.44	168.30
RD45-2	9.82	4.12	1.39	166.90
RD45-3	9.56	3.73	1.28	153.40
RD45-4	10.04	3.75	1.79	155.50
RD45-5	5.26	2.58	0.78	125.80
RD45-6	5.48	2.67	1.04	118.10
<i>RD73 series: dense sand</i>				
RD73-1	7.48	2.88	1.78	200.90
RD73-2	7.12	2.95	1.15	215.40
RD73-3	6.7	2.28	1.09	159.50
RD73-4	6.37	2.48	1.29	156.00
RD73-5	3.22	1.63	0.75	140.10
RD73-6	3.09	1.75	0.79	124.00

of time. Hence, the characteristic feature of the stress wave induced in the sand is to be attributed to both, the effective stress transfer through particle–particle contact and turbulent gas filtration process.

For the same simulated air-blast loading, the peak pressure values measured in sand specimen of RD45 are found to be higher than the RD73 specimen. Further, it is observed that the pressure measured at PT1 (P_d) is amplified multiple times of the peak blast overpressure (P_5), and subsequently, pressure values are found to attenuate rapidly with depth. There exist similar as well as contrary outcomes in the previous studies. Akai et al. (1972) have reported immediate attenuation of the pressure upon blast wave interaction with the surface. That is, the non-dimensional peak pressure value (P_d/P_5) was found to be lower than 1. However, this is not always the case, as observed in the present study the pressure value might get amplified higher than the peak blast overpressure and then start to attenuate in the medium. Experimental evidence on stress enhancement are available when compressible foams (Cooper et al. 1991), porous textile layer (Hattingh and Skews 2001; Skews and Bugarin 2006) and sand deposits (Gelfand et al. 1989) were used as protective layer. The stress enhancement in cellular and porous material can occur when highly intensive blast pulse is applied over certain duration. The stress amplification in the medium is due to the formation of the shock wave due to sudden densification of the compressible medium (Li and Meng 2002). The jump responses in the stress wave trajectories are quite comparable to characteristic feature of a shock. The stress enhancement is significant in the loose sand specimen (RD45) which contributes to higher peak pressure, which is likely to undergo less densification when compared to the dense sand specimen (RD73).

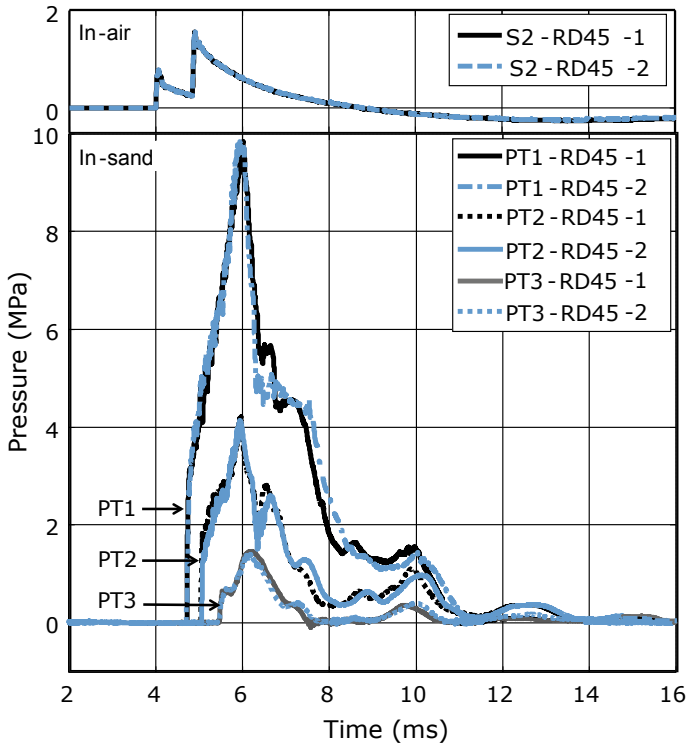


Fig. 5.6 Pressure-time histories recorded in loose sand deposit

As we observe the ‘in-sand’ pressure pulse, the rise time for the pressure wave to attain its peak intensity decreases with the depth. The ‘rise time’ is defined as the duration between the arrival time instances of the wave front to the time taken to attain the peak value. For example, for a typical case of RD45 specimen (refer Fig. 5.6), the rise time is measured to be 1.295, 0.893 and 0.666 ms, at a depth of 75, 135 and 200 mm from the impact surface. The passage of stress wave would have resulted in volumetric compressibility of the void space, thereby restricting the flow of the entrained gas along the depth of the sample. In a compressed stratified layer of sand, the intensity of stress wave decreases with depth and likewise the gas mass flow rate also varies along the depth. It is interesting to note that all the pressure values attain the peak at the same instance of time. This indicates that the flow has terminated, and the gas pressure steadily decreases until it encounters any reflected wave fronts. Similar results to those presented above are obtained for various other test cases having higher Z value. The maximum peak pressure values recorded from these tests are listed in ‘in-sand’ peak pressure columns of Table 5.2.

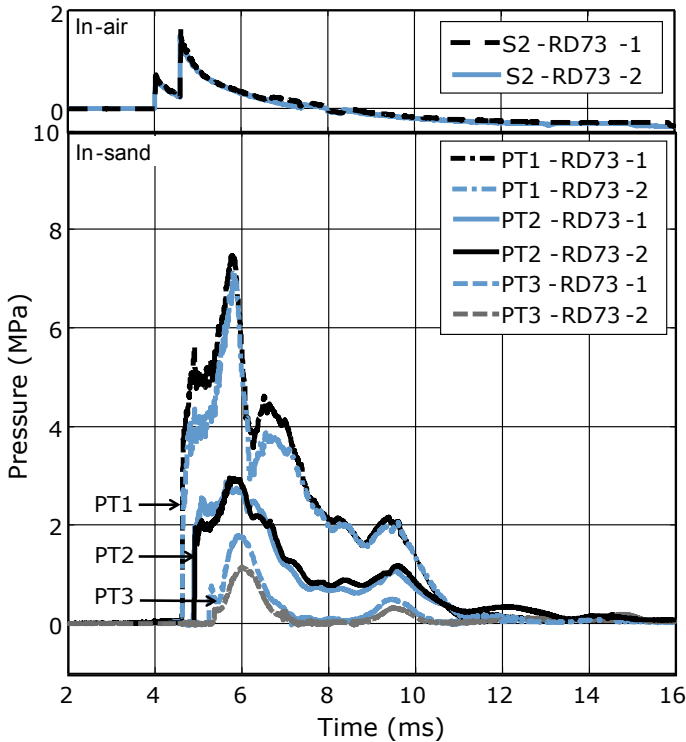


Fig. 5.7 Pressure–time histories recorded in dense sand deposit

5.5 Stress Wave Propagation and Attenuation

Upon the blast wave impact on the surface, the compressive stress wave with an instantaneous rise propagates through the sand medium. The arrival time of the wave front is determined by calculating the duration between the impact time and the rising point of the stress wave signal. Since no sensors are mounted on the surface, the impact time is indirectly measured from transducers mounted in the shock tube. The velocity of the incident shock front is obtained by dividing the distance between transducers (S_1 and S_2) by the differences in the arrival time of the incident shock wave. The impact time is calculated by knowing the offset distance of S_2 and the velocity of the incident shock wave. The plot of arrival time of stress wave versus depths for RD45 and RD73 sand sample is shown in Figs. 5.8 and 5.9, respectively.

The propagating stress wave velocities are obtained by a linear fit of dataset belonging to different category of scaled blast distance (Z); the slope of these linear lines gives us the propagating wave velocity in the medium. It is of interest to speculate the impact time by extrapolation of the lines towards zero value (depth and time). The results are satisfactory with all the lines pointing exactly towards the origin. The propagating velocity of stress wave in sand deposits for various test cases

Fig. 5.8 Plot showing arrival time of stress wave versus depths for loose sand deposits

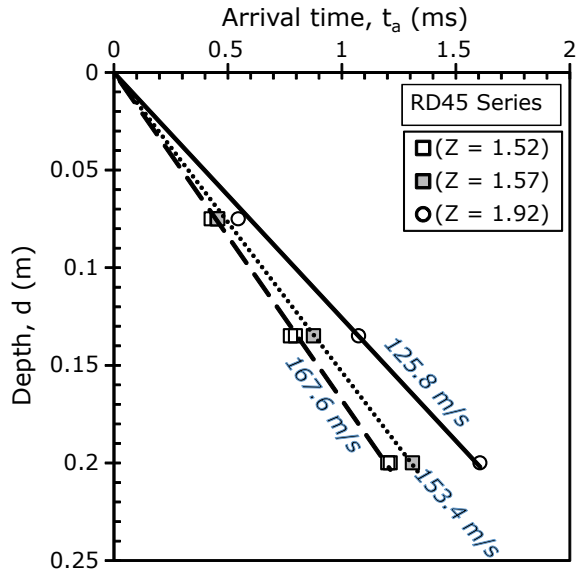


Fig. 5.9 Plot showing arrival time of stress wave versus depths for dense sand deposits

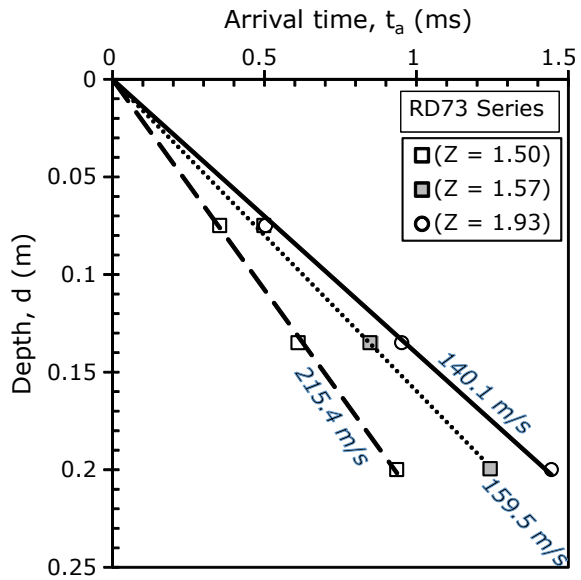
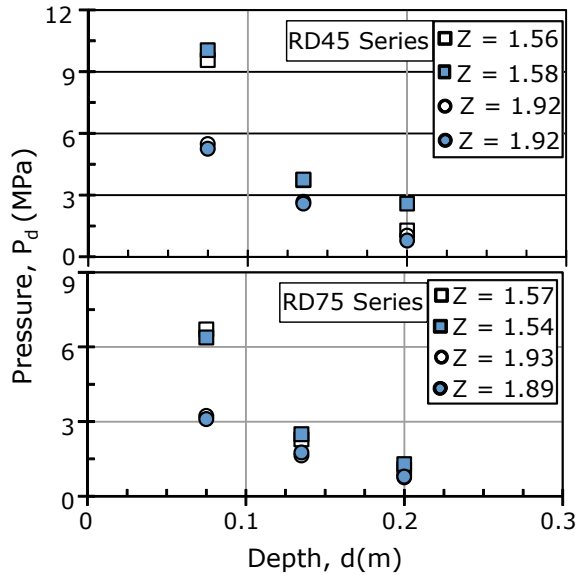


Fig. 5.10 Variation of in-sand peak pressure along the sample depth for loose and dense sand deposit

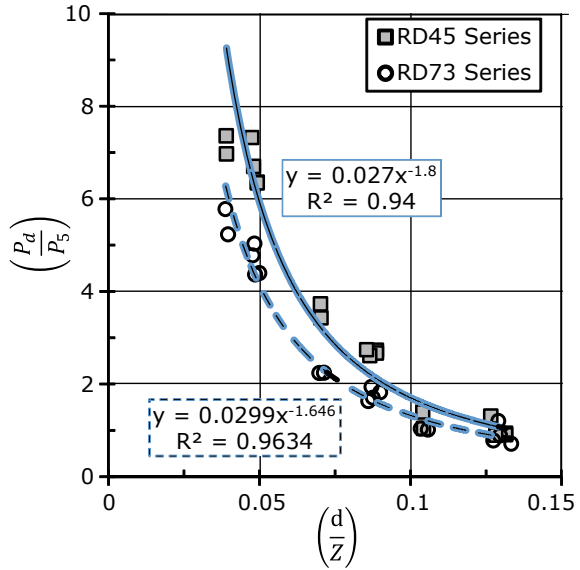


with different Z values is listed in Table 5.2. The propagation velocity of stress wave is found to decrease with the increase in the scaled blast distance (Z). The velocities with which these waves propagate depend on the explosive mass, blast location and the properties of propagating medium. It has been shown experimentally for a similar scaled distance value; the stress wave velocity is found to be propagating at higher velocity in the specimen having higher impedance value. This observation supports the experimental fact that waves travel faster in medium having higher elastic moduli.

Figure 5.10 shows the peak pressure data recorded from the three ‘in-sand’ pressure transducers for different air-blast condition with value of Z ranging from 1.54 to 1.93. The peak pressure value ranges from 10 to 1 MPa. Notably, irrespective of the initial relative density of the specimen, the peak pressure values are found to decrease sharply with depth. In order to get the non-dimensional form of the peak pressure (P_d) and distance (d), the former is divided by the peak overpressure (P_5) of the applied air-blast wave, and latter is divided by scaled distance (Z). The relationships between pressure, the equivalent TNT weight ‘ W ’ and blast location ‘ H ’ are investigated by plotting non-dimensional pressure versus distance, as shown in Fig. 5.11. The data points for the respective test series are provided with power-law regression fit, as most common expression (Eq. 6.1) for pressure attenuation with scaled distance is given by power law (Yankelevsky et al. 2011). The equation of the line and corresponding R^2 values are highlighted in the plot area, where R^2 value is the coefficient of determination and it indicates the goodness of the fit, with R^2 value of 1.0 is a perfect fit. The exponent term in the equation is commonly known as the attenuation coefficient (k), and the ‘ k ’ value for the loose sand and dense sand obtained in the present study for an air-blast is found to be 1.80 and 1.64, respectively.

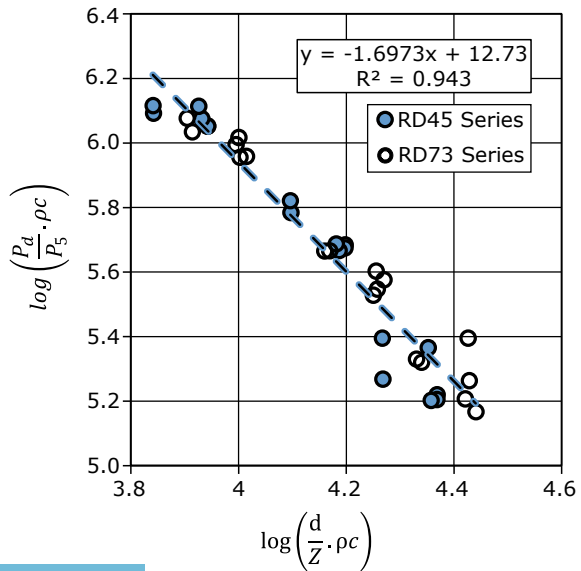
The purpose of this study is also to establish a relationship between scaled distances and peak pressure induced along the depth in loose and dense sand medium.

Fig. 5.11 Non-dimensional peak pressure attenuation in sand



Hence, a more explicit and generic expression is generated by multiplying the parameters (non-dimensional pressure and distance values) with the impedance value of the material and is converted to logarithm scale of base 10. Figure 5.12 shows all normalized pressure data points recorded from the test series RD45-1 to 6 and RD73-1 to 6. Consequently, a direct relationship is established by plotting a linear least-squares

Fig. 5.12 Plot showing normalized peak pressure parameter versus normalized depth parameter



regression line, as shown in Eq. (5.3).

$$\log\left(\frac{P_d}{P_5} \cdot \rho c\right) = -1.6973 \log\left(\frac{d}{Z} \cdot \rho c\right) + 12.73 \tag{5.3}$$

The scatter of the normalized data points shows a reasonable average prediction, with more than 90% of the data points are well within a band of $\pm 30\%$ offset value from the dotted line. It should be noted that the present study considers only limited number of scaled distances and the above equation is valid for prediction over a shallow depth of dry sand deposit (up to 200 mm).

5.6 Air-Blast Wave-Induced Vibration

Figure 5.13 shows a pictorial illustration of simulated air-blast event, as and when an explosive is detonated in air at an altitude ‘H’ from the target surface, the shock wave begins to propagate away from the source location. As discussed in the previous sections, when blast wave strikes the surface, high-intensity stress wave is induced in the sand medium, which is followed by rapidly expanding gas at high pressure. The passage of stress wave and gas flow will induce vibration in the sand deposits, which is composed of body waves and surface waves (Albert et al. 2013; Yasui et al. 2015). The effect and implication of compressional body waves alone are considered in the experimental investigation. The target being a deposit of sand grains, disturbance level will be significant in all the three-dimensional space. The triaxial accelerometers

Fig. 5.13 Pictorial representation of air-blast impact and the propagation of blast-induced body waves in sand deposits

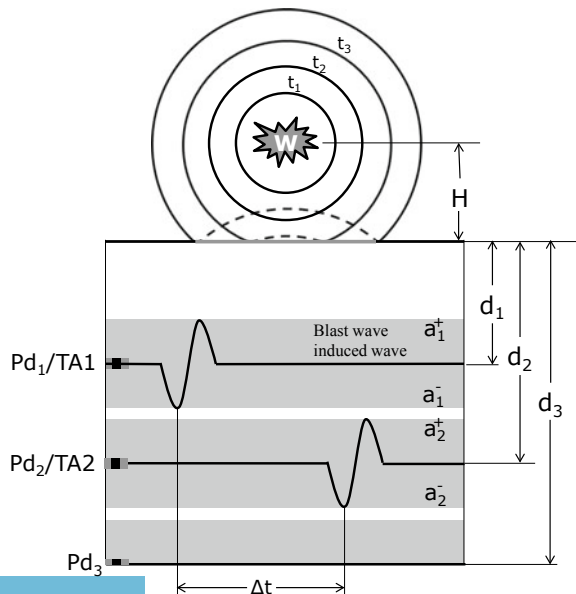


Table 5.3 Summary of the vibrational response results for loose and dense sand deposits

Output values	Scaled distance	Peak acceleration		PPV
Test case	Z (m/kg ^{1/3})	d ₁ (g)	d ₂ (g)	d ₁ (m/s)
<i>RD45 series: loose sand</i>				
RD45-1	1.520	747.85	688.40	2.199
RD45-2	1.520	737.70	668.70	2.178
RD45-5	1.916	406.05	356.11	1.421
RD45-6	1.920	417.25	320.83	1.403
<i>RD73 series: dense sand</i>				
RD73-1	1.549	581.81	513.41	1.507
RD73-2	1.499	554.88	490.05	1.452
RD73-5 ^a	1.932	333.15	–	1.087
RD73-6 ^a	1.890	316.63	–	1.075

^ad₂ signals failed to capture in some way

are used to measure the disturbance, and it is commonly expressed in peak particle acceleration (PPA) and peak particle velocity (PPV).

The energy transmitted in the form of vibrational waves is often denoted as PPV and has always been quantified with a meaningful relationship with the scaled distance (Z) of the explosion. PPV response analysis is categorized into two groups based on the range of 'Z' values, Z = 1.52–1.5 and Z = 1.89–1.93. As testing progressed for different cases, accelerometer located at TA2 became inoperative for certain cases (RD73-5,6). Only selected representative acceleration/velocity responses are presented herein; rest of the signals are shown in Table 5.3.

Figure 5.14 shows acceleration–time series waveforms recorded along the three coordinate axes for two similar simulated air-blast events (54.15 kg at distance of 5.75 m and 54.99 kg at distance of 5.78 m); the waveforms are obtained at depths of 75 mm (d₁) and 135 mm (d₂) from the blast wave impact surface of RD45-1,2 test case. Very good repeatability is shown in the recorded signals.

The vertical and horizontal acceleration signals shown in Fig. 5.14 are filtered using a low-pass Butterworth filter with a cut-off frequency of 1 kHz. The other higher-frequency components associated with the mechanical vibration associated with the shock tube operation are filtered out. Referring to left panel of Fig. 5.14 (signals from TA1), the maximum horizontal component is less than half the magnitude of the maximum amplitudes of vertical component of the acceleration. Comparing the signals of TA1 and TA2 vertical-Y component, there is slight reduction (about 10%) in the vibration amplitude with depth. However, significant amplification is observed in horizontal-x and z signals recorded at TA2. This behaviour is probably because of the excessive particle movements in the lateral direction (in x-z plane), caused due to the passage of stress waves in y-direction.

In order to get more insights into the vertical acceleration data, signals of TA1 and TA2 are plotted in the same graph over the test time period (time scale ranging

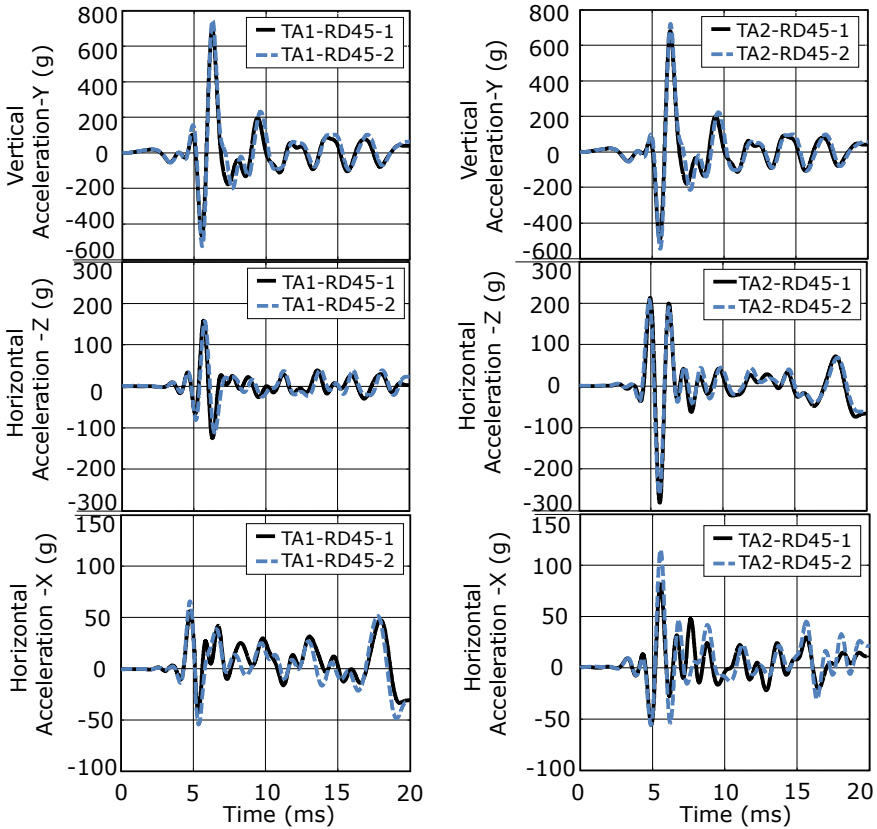


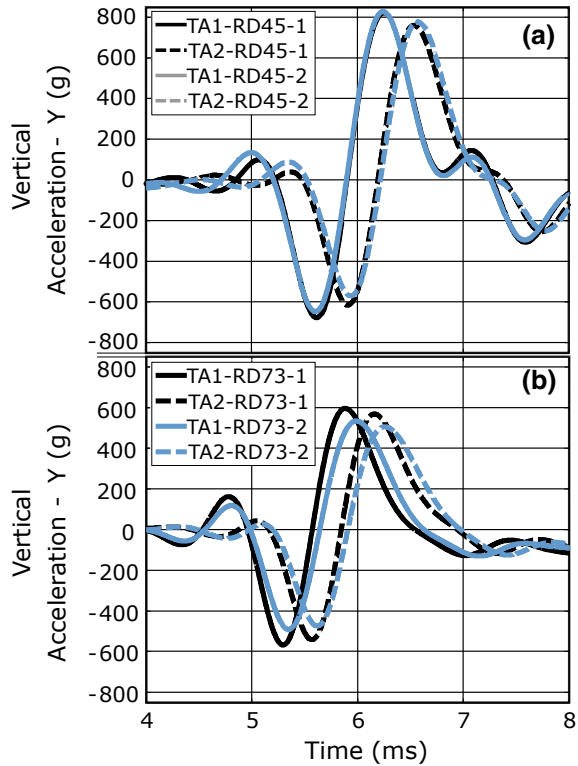
Fig. 5.14 Acceleration–time histories along x -, y - and z -directions in loose sand deposit (left panel: signal recorded at d_1 ; right panel: signal recorded at d_2)

from point of arrival to the time taken to complete the first full cycle of vibration). Figure 5.15 shows the vertical acceleration response for loose and dense sand samples. The amplitude of the acceleration is found to decrease with depth, and the peak amplitude is noticeably higher in the loose sample when compared to the dense sample (as shown in stress waves pressure profiles). For RD45-1, wave velocity of 173 m/s was obtained using the peak time in signals between accelerometers TA1 and TA2, and this value is found close to the propagating velocity of stress wave ($V_p = 168.3$ m/s).

The velocity–time profiles are obtained by integrating the corresponding acceleration signals using a MATLAB function. The velocity profiles generated in a loose sand deposit for different scaled distance ($Z = 1.52$ and $Z = 1.92$) are shown in Fig. 5.16. The velocity profiles generated in a dense sand deposit for different scaled distance ($Z = 1.55$; 1.50 and $Z = 1.89$; 1.93) are shown in Fig. 5.17. The velocity signal profiles shown in Figs. 5.16 and 5.17 for different cases correspond to



Fig. 5.15 Plot showing the y-axis acceleration–time history recorded at depth d_1 and d_2 : **a** loose sand and **b** dense sand



the acceleration response of Y -component of TA1 at location d_1 , which is relatively close to the blast–sand surface interaction. Positive and negative velocities describe the particle motion in opposite directions, and the average peak particle velocity (PPV) is determined for respective test cases (Thusyanthan and Madabhushi 2003).

Best-fit least-squares equations are developed for experimentally obtained PPV values in terms of scaled distance (Z), for the loose (RD45) and dense (RD73) sand specimens. The best-fit curve is shown in Fig. 5.18, and a generalized equation is obtained in the form as shown below:

$$PPV = K \cdot Z^{-b} \tag{5.4}$$

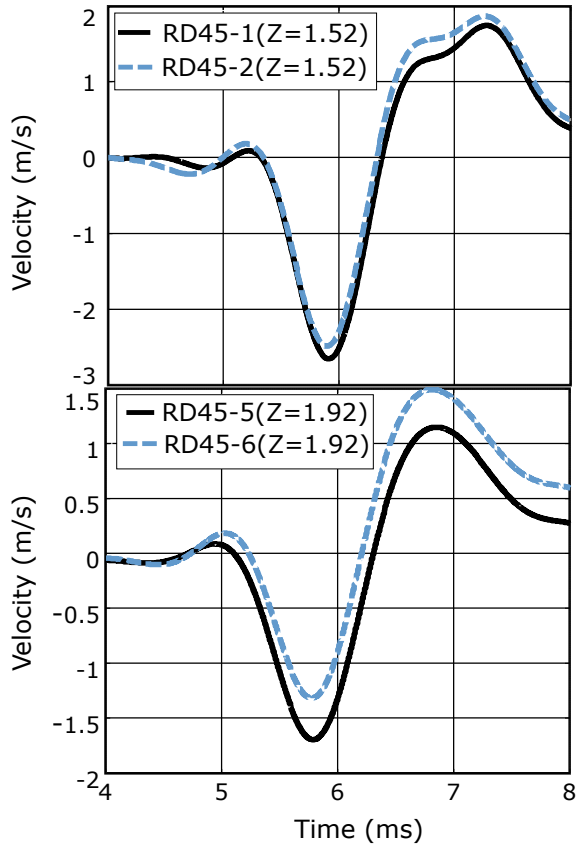
where the constant ‘ k ’ and ‘ b ’ are said to be depending on the material properties of the ground conditions (Kumar et al. 2013).

The generalized equation for the loose and dense sand deposits obtained from Fig. 5.18 is shown in Eqs. (5.5) and (5.6).

$$PPV = 4.80 \left(\frac{H}{W^{1/3}} \right)^{-1.88} \text{ m/s } \text{Loose sand} \tag{5.5}$$



Fig. 5.16 Velocity–time histories for different scaled blast distance in loose sand deposit: (top) $Z = 1.52$; (bottom) $Z = 1.92$



$$PPV = 2.61 \left(\frac{H}{W^{1/3}} \right)^{-1.36} \text{ m/s Dense sand} \quad (5.6)$$

The attenuation coefficient of PPV in loose and dense deposit is found to be 1.88 and 1.36, respectively. It is observed from the trend line shown in Fig. 5.18, the impedance value of the medium has a significant role on the vibrational effects of an air-blast explosion. A medium with a high relative density has a low PPV on the PPV-Z plane. Figure 5.18 also shows the experimental data of a similar air-blast experiment (Busch et al. 2015) performed on a cohesive soil medium. Attenuation trend lines described by Eq. (5.7) fit their experimental data points. The data points are found to be more scattered away from the present study values. The use of cohesive clay sample could be a possible reason; the cohesive resistance offered to the particle movement is higher in clay deposits when compared to sand. Moreover, the formula for estimating scaled distance (Z) in Busch et al. (2015) differs from the present study. Busch et al. (2015) have defined the altitude ‘ H ’ as the distance of the buried sensor to the blast source, i.e. it includes the air stand-off distance plus

Fig. 5.17 Velocity–time response for different scaled blast distance in dense sand deposit: (top) $Z = 1.50, Z = 1.55$; (bottom) $Z = 1.93, Z = 1.89$

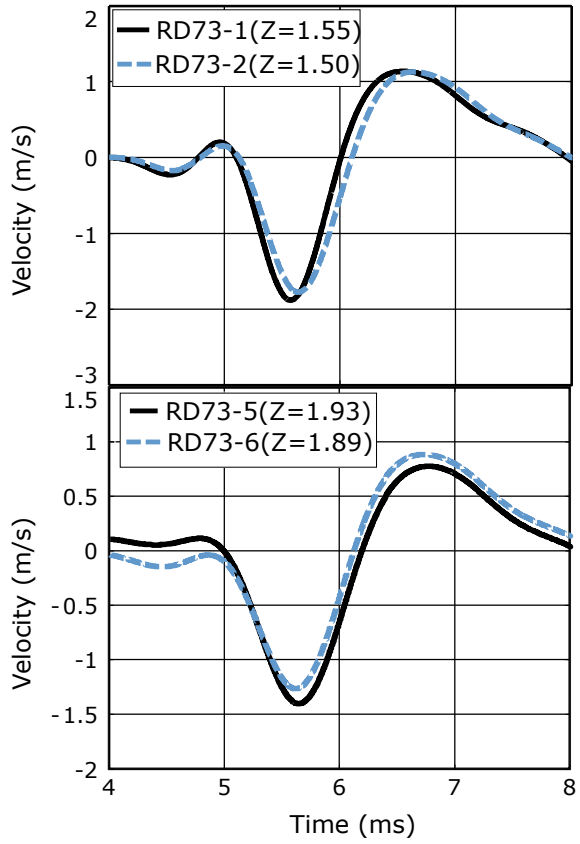
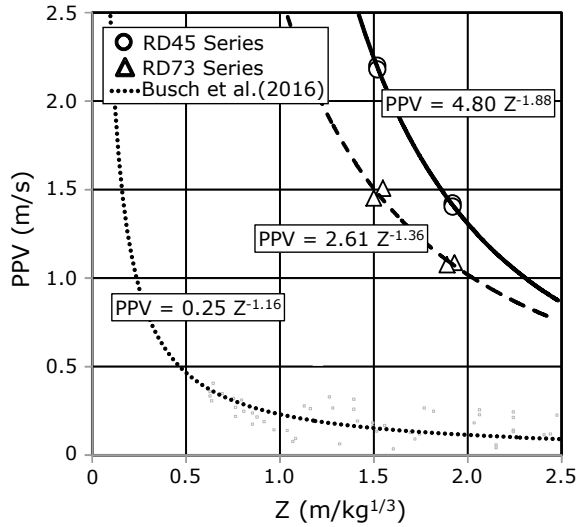


Fig. 5.18 Plot showing relationship between peak particle velocity and scaled distance



the depth of burial of the sensor. However, in the present study, the ‘ H ’ is defined as the distance from the surface of specimen to blast source. Nevertheless, we find that the simulated air-blast experiments are in meaningful agreement with the trends obtained from the experiments using real explosives (Busch et al. 2015)

$$PPV = 0.25 \left(\frac{H}{W^{1/3}} \right)^{-1.16} \text{ m/s Cohesive soil} \quad (5.7)$$

Mechanical densification of sand particles becomes increasingly cohesive with the applied pressure (Piccolroaz et al. 2006). Increase of density, ‘ ρ ’ and wave velocity, ‘ c ’ in the sand deposit has confirmed the increase of cohesive forces because of particle–particle interactions. With the increase in impedance ($\rho \cdot c$) value, the constants k and b are found to decrease, which ultimately reduces PPV value. An extended comparison between trend line of Busch et al. (2015) and the present study has concluded that the impedance value plays a significant role in estimation of blast response parameters in the target specimen.

5.7 Blast Wave-Induced Displacement and Strain Fields

This section discusses the results of digital image correlation (DIC) performed on the two test samples, loose and dense sand deposits (RD45-7 and RD73-7). A simulated air-blast loading corresponding to an explosion of 50.74 kg of TNT at 5.82 m is applied on the loose sand deposit and 54.75 kg of TNT at 5.93 m for the denser sand medium.

The downward and upward movements of the sand particle are evident through the window. Instant displacement and strain fields are obtained by analysing the high-speed images using DIC algorithms. Displacement contour fields generated for a loose sand deposit (RD45-7) are presented through a series of images in Fig. 5.19a. A snapshot of the original image considered for the DIC analysis is superimposed on one of the contour images ($t = 5.25$ ms). The displacement contours are computed at a time interval of 83.32 μs , and a maximum value is recorded in the image captured at 2.51 ms from the trigger event (at 4 ms). The peak pressure value of stress waves is observed around 6 ms (refer Fig. 5.6), which is 2 ms from the trigger point. This reveals that upon passage of the stress waves, the sand bed is susceptible to particle rearrangement. The particle displacements are observed to be predominant in the middle portion of the specimen, which are highlighted by blue density contours. The displacement of coordinate points (P_1 and P_2) is plotted over test time duration in Fig. 5.19b. The location of point P_1 and P_2 is the projection of the buried accelerometers. The data points highlighted in the red correspond to the images shown in Fig. 5.19a. The maximum displacement for the particle located at P_1 and P_2 is found to be -1.613 and -1.347 mm, respectively. The particle motions near the embedded accelerometers are described by acceleration–time series in Fig. 5.15a.

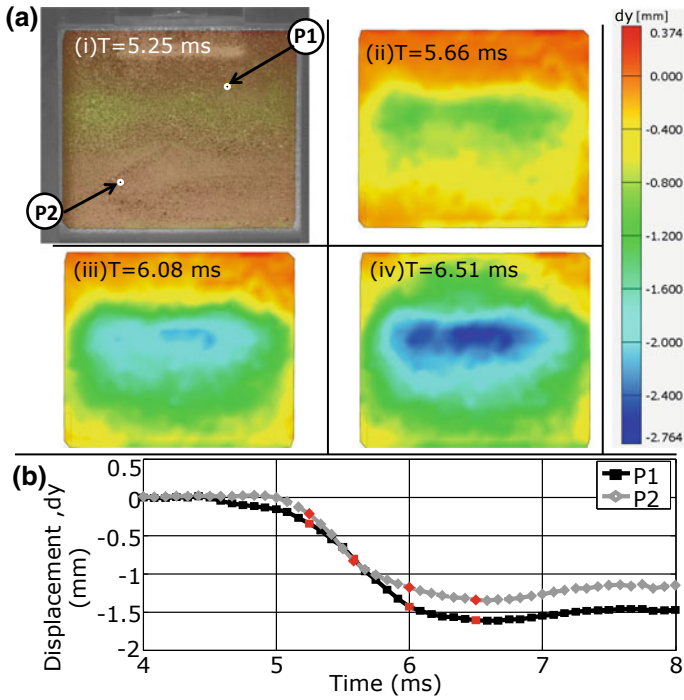


Fig. 5.19 DIC analysis results: **a** displacement contour at $t = 5.25$ ms, 5.66 ms, 6.08 ms and 6.51 ms; **b** displacement versus time for coordinate P_1 and P_2

The displacement value can be numerically determined by integrating twice the acceleration signal; this is often done when analysing the ground response during earthquake. The peak displacement for P_1 and P_2 by direct integration is found to be -1.587 and -1.457 mm, respectively, which is close to the values obtained through optical methods.

We further investigate the blast-induced strain in loose and dense sand specimens. The local strain is computed using DIC algorithm available in GOM-ARAMIS (GOM mbH 2009). The strain contours over the lateral surface area of the test specimen are shown in Figs. 5.20 and 5.21 for loose and dense sand deposits, respectively. The images of strain field shown for loose and dense sand specimens are captured at 2.51 ms and 2.55 ms, respectively, from the time of the trigger.

Plots in Figs. 5.20 and 5.21 also show the strain profile as a function of depth along the axis $Y'-Y'$. The sample can be divided into two parts, upper half where positive strain is observed and the lower half with predominantly negative strain, where a positive strain refers to a contraction and a negative strain refers to extension. Maximum strains are observed in the upper half portion of the sample, which is close to the surface of blast interaction. The regions immediately adjacent to the surface are highly compressed due to high impulsive pressure resulting from stress enhancement and gas filtration process. It is also noteworthy that the relatively large negative strains

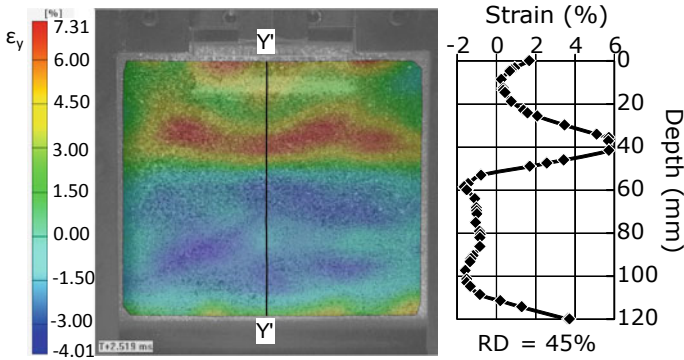


Fig. 5.20 DIC-computed strain contour for loose sand (plot shows variation of strain along $Y'-Y'$ section)

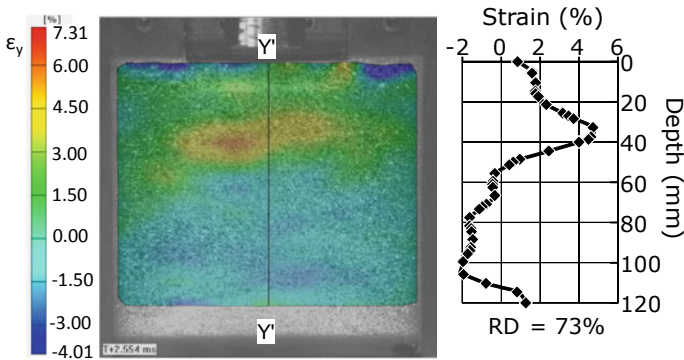


Fig. 5.21 DIC-computed strain contour for dense sand (plot shows variation of strain along $Y'-Y'$ section)

are formed in the lower half portion. The dilative strains are due to the passage of the stress waves. A similar dilative trend was observed in the accelerometer signals located at the lower half (acceleration along Z and X axes in Fig. 5.14). The magnitude of the strain is lower in RD73 when compared to RD45 specimen. The sand particles in RD73 specimen are packed closely prior to blast impact, restricting any further movement of the particles due to the compaction wave front. Thus, one can assume that there is minimum deformation in the denser sample.

5.8 Summary

The characteristic response of sand under impulsive air-blast loading is studied with the help of a shock tube. The experiments performed over dry loose and dense sand samples are presented in this chapter. The role of stress transfer through sand

particles and the expansion of high-pressure gas in the formation of stress waves are discussed in detail. Dimensionless parameters are identified to predict the peak pressure and PPV in loose and dense sands corresponding to the scaled distance range of 1.52–1.93 m/kg^{1/3}. Based on the experimental results, an empirical equation has been developed as a function of scaled distance to predict peak pressure and peak particle velocity in sands. The prediction of these parameters will help us to evaluate the potential of granular medium like sand in mitigating the air-blast effects and will certainly aid in the design of protective structures. Finally, digital image correlation technique is presented to obtain displacements and strains induced in the sand deposits. The general objective of this study is to observe the characteristic response of sand under impulsive air-blast loading, and it is demonstrated with the help of a shock tube. The shock tube simulates blast waves in a controlled laboratory environment; air-blast loading generated is characterized with TNT equivalent of an explosion. The experiments are performed over dry loose (RD = 45%) and dense (RD = 73%) sand specimens. Pressure transducers and accelerometers are positioned in the sand specimens to measure the intensity of pressure waves and vibrational amplitudes. Synchronized pressure and accelerometer measurements have enabled a thorough investigation of stress wave-induced vibrations. Finally, digital image correlation technique is used to obtain displacements and strains induced in the sand deposits.

Immediately after the blast wave strikes the sand surface, a high-intensity compressive stress wave is generated in the sand medium. The layer of sand just below the surface is abruptly compacted, which leads to stress enhancement, especially with the sample of low relative density. The stress transfer through sand particles and the expansion of high-pressure gas through sand media play an important role in the formation of stress waves. Peak stress wave pressure in sand and peak particle velocity (PPV) is observed to decrease with increase in the cube-root scaled distance of an air-blast. Dimensionless parameters are identified to predict the peak pressure and PPV in loose and dense sand corresponding to the scaled distance range of 1.52–1.93 m/kg^{1/3}. Incremental displacement of the sand deposit acquired through DIC showed that the displacement patterns are well comparable with the direct physical measurements. The strain field obtained from the image analysis has revealed large magnitude of compressive strains in the layers adjacent to the blast impact, whereas significant dilative strains are also observed in the layers extending farther away from the impact.

Based on the experimental results, an empirical equation has been developed as a function of scaled distance to predict peak pressure attenuation and peak particle velocity in sands. The prediction of these parameters will help us to evaluate the potential of granular medium like sand in mitigating the air-blast effects and will certainly aid in the design of protective structures. The experimental investigations presented in this chapter are limited to very small range of scaled blast distance; it is necessary to replicate the present study over a wide range of scaled distance. This can be achieved either by changing the shock tube configuration or by varying the thickness of the diaphragm. To further demonstrate the bonding and cohesion effects, additional experiments need to be carried out on fine-grained soils and cohesive clay samples.

References

- Akai K, Hori M, Ando N, Shimogami T (1972) Shock tube study on stress wave propagation in confined soils. *Proc Jpn Soc Civ Eng* 200:127–140
- Albert DG, Taherzadeh S, Attenborough K, Boulanger P, Decato SN (2013) Ground vibrations produced by surface and near-surface explosions. *Appl Acoust* 74(11):1279–1296
- Alekseenko VD, Rykov GV (1972) Experimental data on stress-wave parameters in the earth due to underground and surface explosions. *J Appl Mech Tech Phys* 9(4):409–411
- Ambrosini RD, Luccioni BM, Danesi RF, Riera JD, Rocha MM (2002) Size of craters produced by explosive charges on or above the ground surface. *Shock Waves* 12(1):69–78
- Baker WE (1973) Explosions in air. University of Texas Press, Austin
- Ben-Dor G, Britan A, Elperin T, Igra O, Jiang JP (1997) Experimental investigation of the interaction between weak shock waves and granular layers. *Exp Fluids* 22(5):432–443
- Busch CL, Aimone-Martin CT, Tarefder RA (2015) Experimental evaluation of cratering and ground vibration in clay soils subjected to explosive airblast loading. *J Test Eval* 43(2):20130296
- Cooper GJ, Townend DJ, Cater SR, Pearce BP (1991) The role of stress waves in thoracic visceral injury from blast loading: modification of stress transmission by foams and high-density materials. *J Biomech* 24(5):273–285
- Drake JL, Little CD (1983) Ground shock from penetrating conventional weapons. In: Proceedings of the symposium on the interaction of non-nuclear weapons with structures, Colorado Springs, USA
- Gelfand BE, Medvedev SP, Borisov AA, Polenov AN, Frolov SM, Tsyganov SA (1989) Shock loading of stratified dusty systems. *Arch Combust* 9:153–165
- GOM mbH (2009) Aramis user's manual. Braunschweig, Germany
- Hattingh TS, Skews BW (2001) Experimental investigation of the interaction of shock waves with textiles. *Shock Waves* 2:115–123
- Kingery CC, Bulmash G (1984) Air blast parameters from TNT spherical air burst and hemispherical surface burst. Defence technical information center, Ballistic Research Laboratory, Aberdeen proving ground, Maryland, USA, Report BRL, 02555
- Kinney GF, Graham KJ (1985) Explosive shocks in air. Springer, New York
- Kumar R, Choudhury D, Bhargava K (2013) Prediction of blast induced vibration parameters for soil sites. *Int J Geomech* 14(3):1–10
- Leong EC, Anand S, Cheong HK, Lim CH (2007) Re-examination of peak stress and scaled distance due to ground shock. *Int J Impact Eng* 34(9):1487–1499
- Li QM, Meng H (2002) Attenuation or enhancement—a one-dimensional analysis on shock transmission in the solid phase of a cellular material. *Int J Impact Eng* 27(10):1049–1065
- Piccolroaz A, Bigoni D, Gajo A (2006) An elastoplastic framework for granular materials becoming cohesive through mechanical densification. Part I—small strain formulation. *Eur J Mech A Solids* 25(2):334–357
- Rinehart EJ, Welch CR (1995) Material properties testing using high explosives. *Int J Impact Eng* 17(4–6):673–684
- Roy PP (1998) Characteristics of ground vibrations and structural response to surface and underground blasting. *Geotech Geol Eng* 16(2):151–166
- Scherbatiuk K, Rattanawangcharoen N (2011) A hybrid rigid-body rotation model with sliding for calculating the response of a temporary soil-filled wall subjected to blast loading. *Int J Impact* 37:11–26
- Shin J, Whittaker AS, Cormie D (2015) Incident and normally reflected overpressure and impulse for detonations of spherical high explosives in free air. *J Struct Eng* 14(12):04015057
- Skews BW, Bugarin S (2006) Blast pressure amplification due to textile coverings. *Text Res J* 76(4):328–335
- Smeulders DMJ, van Dongen MEH (1997) Wave propagation in porous media containing a dilute gas–liquid mixture: theory and experiments. *J Fluid Mech* 343:351–373

- Smith P (2010) Blast walls for structural protection against high explosive threats: a review. *Int J Prot Struct* 1(1):67–84
- Smith PD, Hetherington JG (1994) Blast and ballistic loading of structures. Butterworth-Heinemann, London
- Sniekers RWJM, Smeulders DMJ, van Dongen MEH, van der Kogel H (1989) Pressure wave propagation in a partially water-saturated porous medium. *J Appl Phys* 66(9):4522–4524
- Thusyanthan NI, Madabhushi SPG (2003) Experimental study of vibrations in underground structures. *Proc Inst Civ Eng Geotech Eng* 156(2):75–81
- TM5-855-1 (1986) Fundamentals of protective design for conventional weapons. US Department of the Army Technical Manual, USA Army Corps of Engineers
- van-der Grinten JGM, Van-Dongen MEH, van-der Kogel H (1985) A shock-tube technique for studying pore-pressure propagation in a dry and water-saturated porous medium. *J Appl Phys* 58(8):2937–2942
- Whitman R (1970) The response of soils to dynamic loadings; report 26, final report. Army Engineer Waterways Experiment Station, Mississippi, USA
- William RP, Robert CB (1975) Free-field ground motion induced by underground explosions. Sandia Laboratories, SAND740252, Albuquerque, New Mexico
- Wu C, Hao H, Lu Y, Sun S (2004) Numerical simulation of structural responses on a sand layer to blast induced ground excitations. *Comput Struct* 82(9–10):799–814
- Wu C, Lu Y, Hao H, Lim WK, Zhou Y, Seah CC (2003) Characterisation of underground blast-induced ground motions from large-scale field tests. *Shock Waves* 13(3):237–252
- Yankelevsky DZ, Karinski YS, Feldgun VR (2011) Re-examination of the shock wave's peak pressure attenuation in soils. *Int J Impact Eng* 38(11):864–881
- Yasui M, Matsumoto E, Arakawa M (2015) Experimental study on impact-induced seismic wave propagation through granular materials. *Icarus* 260:320–331

Chapter 6

Response of Embedded Structures in Granular Material to Air-Blast Wave Loading



6.1 Introduction

Understanding the response of embedded structures like tunnel, pipeline, etc. under impulsive loading induced by explosions has always been an important topic of discussion in the geotechnical research fraternity. In the present study, buried pipeline which is an embedded structure is considered as a potential target. A possible damage to the pipelines that carries crude oil and gas not only risk the lives of people in the vicinity but also brings about immediate transit interruptions resulting in economic loss. In order to inflict maximum damages to the target, the explosives are detonated at an altitude above the ground surface. As the blast wave front strikes the ground surface, shock waves get dissipated in the form of stress waves causing damage to the underground pipelines. The overburden soil above the buried structures plays an important role as sacrificial layers in mitigating the incoming shock waves. Hence, the knowledge of optimum depth of burial (DoB) with respect to an air-blast condition is crucial in the design of buried structures. The nature and extent of damage depend on a number of factors such as the intensity of blast wave, the properties of the sand, the stiffness and geometry of the embedded pipe structure. This study proposes a new shock tube-based small-scale experimental technique for testing buried pipelines. In the previous chapter, we have seen that shock tube was capable of generating air-blast loading, and it has been proven to be an efficient tool for testing materials under air-blast conditions (Aune et al. 2016; Kleinschmit 2011; Newman and Mollendorf 2010).

6.2 Previous Studies

Though the blast response of underground structures subjected to surface/air explosion has been studied by many researchers in the past using numerical simulations (Aune et al. 2016; Koneshwaran et al. 2015; Xu et al. 2013; Zhang et al. 2016), only a few researchers performed experiments on a real physical model. Surface explosion experiments performed by De and Zimmie (2007) on a reduced-scale (1:70 scales) model using a geotechnical centrifuge (De et al. 2016) lead to quantitative data on buried structures exposed to a surface blast. However, the cost and risk associated with full-scale field tests involving explosives and the complexity of the diagnostic measurements necessitate the need for an alternative testing method. The shock tube-based tests can be considered as a potential replacement to the conventional testing methods (Aune et al. 2016; Colombo et al. 2011, 2013).

The objective of the present study is to understand the attenuation behaviour of sand deposits and their role as sacrificial layers in protecting the buried structures like pipelines. This is achieved by recording the pressure–time histories at different depths of the sand deposit. In addition, dynamic strain measurements are used to capture the response of pipe.

6.3 Experimental Setup

6.3.1 Test Chamber and Instrumentation

Vertical shock tube (VST) is used in the present study to generate air-blast loading conditions. The shock tube blast experiments are performed on a reduced-scale model, and the rear end of the shock tube is attached to a 200 mm square test chamber. The test chamber mentioned in Sect. 5.3.1 is used in the present study with fine sand (Chap. 3) as infill deposit material. In the present study, sand pluviation technique is used to prepare the sand deposit with a relative density of 73% with an approximate density of 1606 kg/m³. An aluminium pipe of diameter of 25 mm (ID_{ai}), with a wall thickness (T_{ai}) of 1.25 mm, is clamped to the inside wall of the test chamber at specific depth. The distance from the crown of pipe to the top surface of the sand bed is denoted as depth of burial (DoB). The schematic diagram of the test chamber along with the embedded pipe is shown in Fig. 6.1a. The photograph of the embedded pipe and levelled surface after burying the pipe is shown in Fig. 6.1b, c, respectively. The geometrical and engineering properties of the pipe are mentioned in Chap. 3 (Sect. 3.4.4), and the specific details are also listed later in Table 6.2.

Two pressure transducers, S_1 and S_2 , mounted near the rear end of the vertical shock tube. The pressure transducers are of piezo-electric type and record the pressure profile and velocity of the shock wave. To capture the principal stresses in the sand deposit, three pressure transducers (PT1, PT2 and PT3) are embedded at different depths from the surface of the sand bed in the test chamber (Fig. 6.1). The pressure

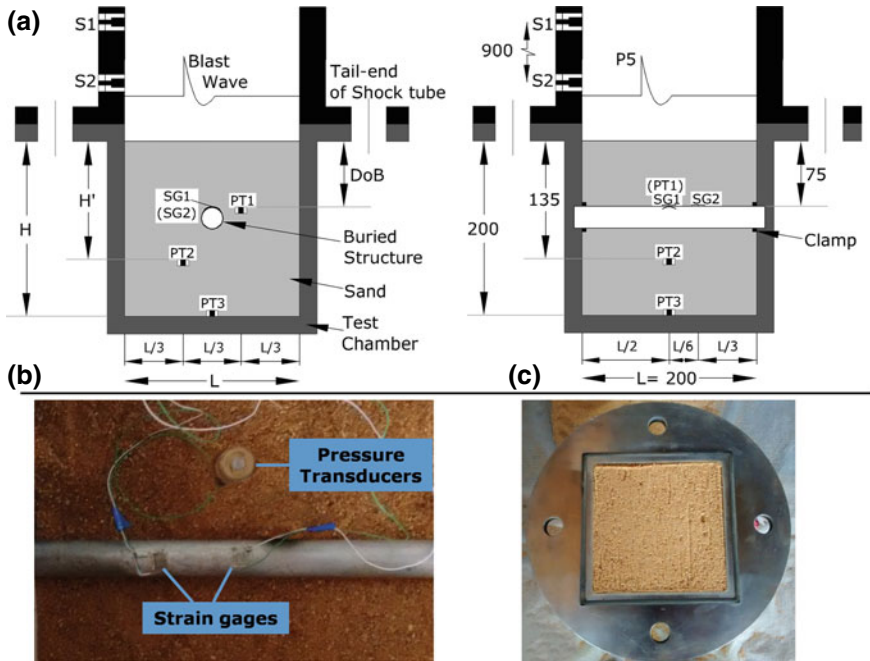


Fig. 6.1 a Schematic diagram of the cross-sectional view of the test chamber showing the position of the buried pipe and the sensors (all dimensions are in mm); b photograph of the top view of the buried pipe; and c photograph of the finished top surface of the sand deposit

sensors are connected to an oscilloscope through a PCB signal conditioner. The pressure profiles recorded by the embedded sensors indicate the possible pressure distribution around the buried pipe. To measure the strain response of the pipe in the axial direction, two strain gauges (SG1 and SG2) are installed on the top crown surface on the pipe. The strain gauge SG1 is mounted at the centre of the pipe crown and SG2 is located at one-third of the pipe span. The strain gauges are engaged in a quarter bridge Wheatstone configuration using DAQP-STG module of M/s Dewetron GmbH. Data acquisition from the strain gauges and pressure sensors is achieved using an oscilloscope (Yokogawa DL750) with a sampling rate of 500 kHz.

6.3.2 Blast Wave Characterization

Figure 6.2 shows pressure profile captured by the side-on pressure sensor located immediately above the surface of the sand deposit, when the shock tube is operated with a pressure ratio of 13 (ratio of driver pressure, $P_4 = 13$ bar to the pressure in the driven section, $P_1 = 1$ bar; $1 \text{ bar} = 10^5 \text{ N/m}^2$). The diaphragm used for this particular experiment is 2 mm thick with a groove of 0.4 mm, which yielded a rupture pressure

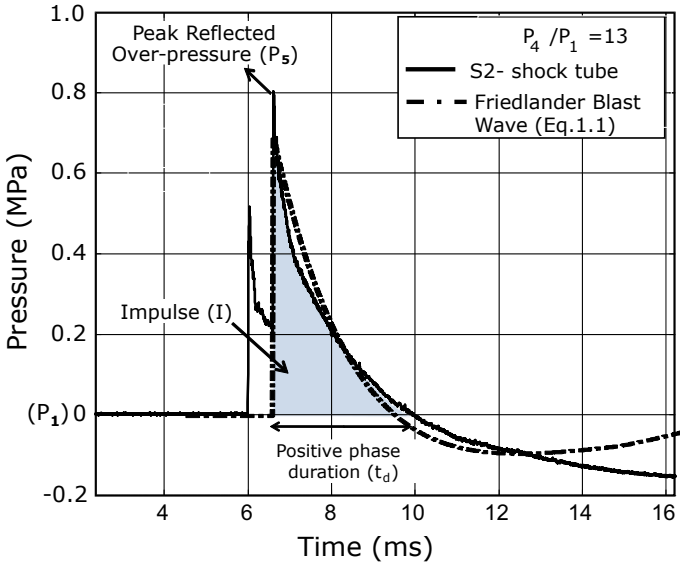


Fig. 6.2 Pressure–time history recorded at end of VST for a pressure ratio, $P_4/P_1 = 13$

of 1.3 MPa (P_4). The generated blast wave with an incident Mach number of 2.98 matches well with that of an ideal Friedlander wave (Eq. 1.1).

In all our experiments, it is presumed that the surface of the sand deposit sand surface is subjected to the constant reflected overpressures registered by pressure sensor S_2 . From the experiment, the blast parameters obtained include the peak-reflected overpressure (P_5) and positive phase duration (t_d); for a pressure ratio of 13, $P_5 = 0.8$ MPa and $t_d = 3.34$ ms are the blast parameters.

Tests were performed with VST for different pressure ratios ($P_4/P_1 = 5, 11, 13, 17, 28$ and 35) to assess its capability in generating different blast wave profiles. For the present set of experiments, VST has a 0.5 m long driver section and 4.5 m long driven section.

The present blast wave condition can be tailored for a range of TNT equivalent by changing the length of driver or driven sections, or by varying the driver gas or rupture pressure (P_4). For different pressure ratios (P_4/P_1), blast waves with different peak pressure profile and impulse are formed. Figure 6.3 depicts graphically the peak pressure and impulse values for a range of pressure ratios (P_4/P_1) obtained from the VST facility for the present test configuration. The values are also listed in Table 6.1.

Further, blast parameters obtained from the experiment can be associated with an equivalent spherical air-burst of TNT explosion (of weight ‘ W ’) taking place at an altitude of ‘ H ’ from the ground surface. Cube-root scaling law is the scaling law commonly used for blast wave that utilizes the scaled distance ‘ Z ’ as the dimensional parameter. Blast parameters for a wide range of detonation conditions can be effectively represented by the parameter, ‘ Z ’. The scaled distance, ‘ Z ’ is expressed as below,

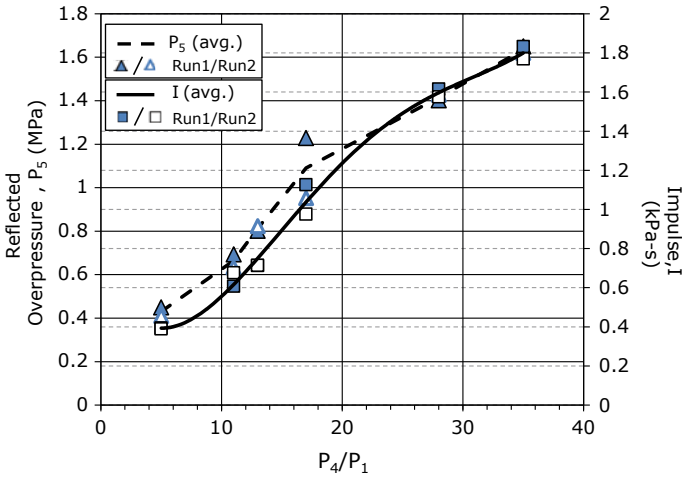


Fig. 6.3 Plot showing peak-reflected pressure and impulse values against the ratio of shock tube pressure

Table 6.1 Shock tube blast parameters corresponding to an equivalent TNT explosion at altitude, H

P_4/P_1	Shock tube blast parameters ^a			Equivalent TNT spherical charge		
	P_5 (MPa)	t_d (ms)	I (kPa s)	Z (m/kg ^{1/3})	W (kg)	H (m)
5	0.451	2.729	0.391	2.285	6.479	4.26
11	0.693	3.065	0.607	1.968	14.238	4.77
13	0.802	3.340	0.712	1.874	19.437	5.04
17	0.952	3.665	0.975	1.772	40.959	6.11
28	1.414	4.244	1.615	1.563	120.415	7.72
35	1.651	4.564	1.832	1.491	149.252	7.91

^aAverage values of the experiments results (minimum of two tests) are reported

$$Z = \frac{H}{W^{\frac{1}{3}}} \tag{6.1}$$

A similar procedure to the one mentioned in Sect. 5.3.3 is carried out in the present study as well. The parameter, Z , is computed using the higher-order polynomial coefficient (derived by Shin et al. (2014)) over the empirical relations (UFC 3-340-02 2008) that represents the experimental data of Kingery and Bulmash (1984). Thus, the TNT explosion equivalent of the blast wave generated in the VST is obtained from the Kingery and Bulmash (1984) chart. A comparison of the blast wave parameters obtained from the shock tube experiment with different mass of TNT detonating at various heights from the ground surface is given in Table 6.1. The pressure profile, shown in Fig. 6.2, recorded by sensor S_2 (helium) is equivalent to the pressure

measured at the ground surface, during a 20 kg TNT detonating at 5 m from the ground surface. The buried pipe experiments reported in the present study are conducted for this specific blast wave condition.

6.4 Experimental Results

6.4.1 Response of Sand Deposits and Buried Pipe

As observed in the previous chapter, as the shock front hits the surface of the sand deposit, two major events take place, firstly, effective stress transfer happens via particle–particle contact and secondly, infiltration of the residual gas (following the shock front) occurs along with the sand deposit in the test chamber. These two phenomena have deteriorated the air-blast wave into stress wave/compression wave in the sand deposit. Figure 6.4 shows the compression stress wave signals recorded by sensors (PT1, PT2 and PT3) for the shock tube experiment having pressure ratio (P_4/P_1) of 13. The compression stress wave is characterized by the appearance of sharp jump with a constant rise to a maximum pressure value accompanied by a gentle drop in the magnitude. The travelling stress wave is planar and rapidly attenuates as it penetrates the sand bed; pressure reduction induced is about 60% of the maximum value measured by the preceding pressure sensor. This quantification serves as an index of the pressure experienced by the pipeline systems buried at different depths from the sand surface.

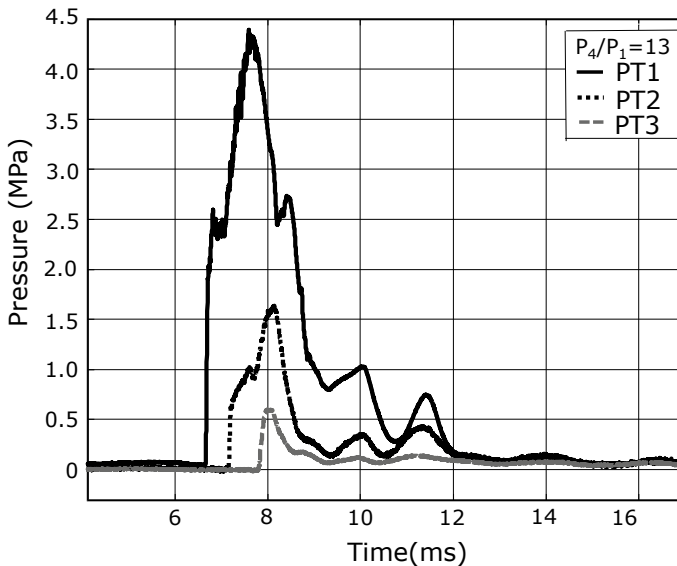


Fig. 6.4 Pressure–time histories recorded inside sand deposits at different depths

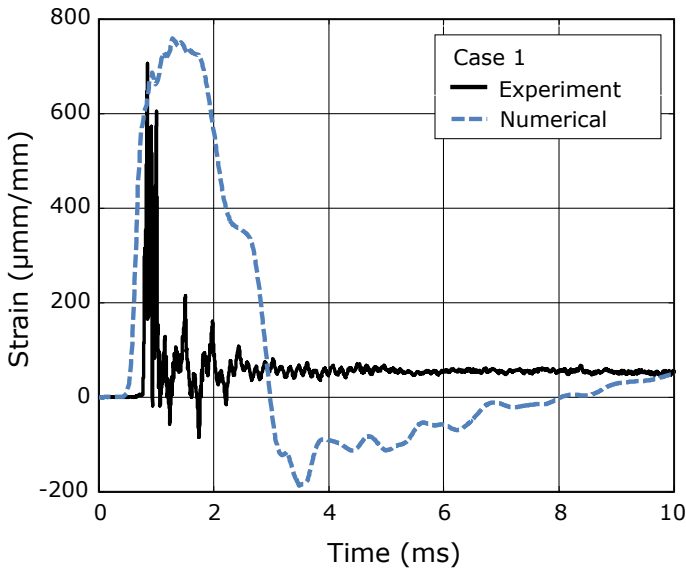


Fig. 6.5 Strain–time history recorded at one-third span of the pipe for case 1

The physical damage of the pipe and nature of the strain signals indicate the blast effect on the pipe. Figure 6.5 shows the strain recorded during the experiment at one-third of the pipe span. From this figure, it is evident that the maximum axial strain caused at this location is about 700 micro-strain. Due to the high-pressure impact of the compression wave, the strain gauge placed at the centre of the pipe crown was damaged and thus failed to record strain signals on multiple test runs. However, after the experiment, the physical (permanent) of the pipe is determined, and it is tangible at the centre of the pipe crown (SG1). It is noticed that the pipe section along the crown is axially compressed whereas the invert section of the pipe experiences tension (Koneshwaran et al. (2015) observed identical behaviour in their numerical study). The peak deflection in the transverse direction (δ_{\max}) at the pipe crown is believed to bounce back as the compression waves move past the pipe. However, this is accompanied by a residual deflection, which is permanent (plastic deflection, δ).

At the end of the experiment, the residual/plastic deformation at the centre of the pipe crown is determined with a height gauge. For test runs 1 and 2, the deflection value is found to be 1.2 mm and 1.1 mm, respectively; an average deflection value is taken for the dimensional analysis.

6.5 Dimensional Analysis

Experiments performed using shock tube for the buried pipeline application are small scale compared to those of the real site conditions. It is important to overcome this scaling issue. In order to link the parameters of the small-scale laboratory experiments with the large-scale real site conditions, dimensional analysis is performed

using Buckingham π -theorems (Zhao et al. 2013). The variables associated with the experiment are listed in Table 6.2; the variables are denoted in the fundamental dimensional units of mass $[M]$, length $[L]$ and time $[T]$. Three (j) recurring variables have been chosen from 11 (n) major dominating variables; the chosen variables include density of the sand bed (ρ_s), elastic modulus of the sand (E_s) and equivalent weight of TNT (W). The case is now limited to a function of 8 ($k = n - j$) dimensionless variables. The governing function 'f' of the integrated system is given by,

$$f(\text{Dob}, EI, E_s, \rho_s, \varphi, W, R, t_d, P_5, \delta, \varepsilon) = 0 \quad (6.2)$$

The dimensionless parameters (π_1 to π_8) can be identified in the function 'g',

$$g(\pi_1, \pi_2, \pi_3, \pi_4, \pi_5, \pi_6, \pi_7, \pi_8) = 0 \quad (6.3)$$

Table 6.2 Input and output variables considered for dimensional analysis

Parameters	Dimension [MLT]	Experimental case 1	Scaling factor	Predicted case 2 ($\lambda = 2$)
<i>Input variables</i>				
Depth of burial, DoB	$M^0 L^1 T^0$	75 mm	Λ	150 mm
Flexural stiffness of pipe, EI	$M^1 L^3 T^{-2}$	613.6 N m ²	λ^4	9818.3 Nm ²
Elastic modulus of sand, E_s	$M^1 L^{-1} T^{-2}$	15 MPa	1	15 MPa
Dry density of sand, ρ_s	$M^1 L^{-3} T^0$	1606 kg/m ³	1	1606 kg/m ³
Friction angle of sand, φ	–	35°	1	35°
Weight of equivalent TNT, W	$M^1 L^0 T^0$	20 kg	λ^3	160 kg
Altitude of explosion, H	$M^0 L^1 T^0$	5 m	λ	10 m
<i>Output variables</i>				
Positive phase duration, t_d	$M^0 L^0 T^1$	3.34 ms	λ	6.68 ms
Peak-reflected overpressure, P_5	$M^1 L^{-1} T^{-2}$	0.8 MPa	1	0.8 MPa
Residual deflection of pipe at the crown (@L/2), δ	$L^1 M^0 T^0$	1.15 mm	λ	2.3 mm
Peak strain at crown (@L/3), ε	$M^0 L^0 T^0$	700 μ mm/mm	1	700 μ mm/mm

$$g \left(\text{Dob} \cdot \sqrt[3]{\frac{\rho_s}{W}}, \frac{EI}{E_s} \cdot \sqrt[3]{\frac{\rho_s^4}{W^4}}, \varphi, R \cdot \sqrt[3]{\frac{\rho_s}{W}}, t_d \cdot \frac{\sqrt{E_s}}{\sqrt[3]{W\rho_s^{1/3}}}, P_5, \delta \cdot \sqrt[3]{\frac{\rho_s}{W}}, \varepsilon \right) = 0 \quad (6.4)$$

Let us consider an output dimensionless parameter, say the deflection term (π_7):

$$\pi_7 = h(\pi_1, \pi_2, \pi_3, \pi_4) \quad (6.5)$$

$$\delta \sqrt[3]{\frac{\rho_s}{W}} = h(\pi_1, \pi_2, \pi_3, \pi_4) \quad (6.6)$$

The ratio of deflection parameter of the prototype to the model (where subscripts 'm' and 'p' mean model and prototype, respectively) yields,

$$\frac{\frac{\delta_p}{\left(\sqrt[3]{\frac{W}{\rho_s}}\right)_p}}{\frac{\delta_m}{\left(\sqrt[3]{\frac{W}{\rho_s}}\right)_m}} = \frac{h((\pi_1)_p, (\pi_2)_p, (\pi_3)_p, (\pi_4)_p)}{h((\pi_1)_m, (\pi_2)_m, (\pi_3)_m, (\pi_4)_m)} \quad (6.7)$$

The case of all the π -parameters (shown in Eq. 6.6) being identical for the model (when scaled) and the prototype implies that the model and the prototype are actually the same. This condition satisfies the RHS of Eq. (6.7) to be unity. In addition, it is necessary that material properties (E_s and ρ_s) of the sand deposit should be the same for both the model and the prototype.

Also, it is important to maintain same material properties (E_s and ρ_s) for the sand deposit in the model to that of an actual condition (prototype).

Rearranging Eq. (6.7),

$$\delta_p = \frac{\left(\sqrt[3]{\frac{W}{\rho_s}}\right)_p}{\left(\sqrt[3]{\frac{W}{\rho_s}}\right)_m} \delta_m = \frac{\sqrt[3]{(W)_p}}{\sqrt[3]{(W)_m}} \delta_m; \quad (6.8)$$

when $(E_s)_p = (E_s)_m$ and $(\rho_s)_p = (\rho_s)_m$.

Finally, scaling coefficient λ is deduced,

$$\delta_p = \lambda \delta_m; \quad \text{where } \lambda = \sqrt[3]{\frac{(W)_p}{(W)_m}} \quad (6.9)$$

The same procedure is carried out for the other variables and the suitable scaling factors are obtained for the input and output variables. The representative values for scaled model along with their scaling factor are mentioned in Table 6.2

The aluminium pipe model along with the definitive set of variables serves as a means to address the phenomenon of air-blast wave. In general, based on the system requirements, inner diameter of the oil pipelines (ID) may vary from 50 mm

to 300 m and the depth of the overburden cover may vary as small as 150 mm to some metres (Kennedy 1993). The pipes for oil pipelines are normally manufactured using steel or cast iron. To match a prototype with a scale factor λ , the model's input parameters are totally scaled using scaling factor. It is again highlighted that the necessary condition of the sand deposit in the model and the prototype having identical material properties is maintained. To get the dimensions of the pipe, scaling law for the flexural stiffness parameter is employed by the prototype and model by elastic modulus. The relation between aluminium pipe (model) and cast iron pipe (prototype) is $E_{p(\text{Cast iron})} = 2E_{m(\text{Al})}$, adequate condition.

$$(EI)_p = \lambda^4 (EI)_m; \quad (6.10)$$

$$\begin{aligned} E_{\text{C.iron}} \frac{\pi}{64} \{(\text{ID} + T)_{\text{C.iron}}^4 - (\text{ID})_{\text{C.iron}}^4\} \\ = \lambda^4 \cdot E_{\text{Al}} \frac{\pi}{64} \{(\text{ID} + T)_{\text{Al}}^4 - (\text{ID})_{\text{Al}}^4\} \end{aligned} \quad (6.11)$$

Similarly, blast parameters are computed by multiplying the peak pressure and positive phase duration with scaled factor of 1 and λ , respectively. This method of dimensional analysis is validated by Hopkinson–Cranz scaling law (Chap. 3, Sect. 3.3). This law states that during scaling, variables with dimension of pressure and weighted positive phase ($t_d/W^{1/3}$) remain the same if the value of Z is the same (Baker 1973). The outcome of the dimensional analysis satisfies this law. From Table 6.2, it is evident that the blast parameters, peak overpressure, P_5 is the same for both the cases and positive phase duration is multiplied by λ . The scaled factor λ is the ratio between cube root of TNT weights of the prototype and the model.

For instance, prototype case 2 (Table 6.2) with scaled factor (λ) of 2 corresponds to the test scenario of 160 kg TNT exploding at a height of 10 m above the surface of the ground.

For this case, a blast wave with P_5 of 0.8 MPa and t_d of 6.68 ms will be generated. This blast wave hits the ground surface, where the cast iron pipe ($\text{ID}_{\text{C.iron}} = 47.5$ mm, $\text{OD}_{\text{C.iron}} = 50$ mm) is buried at a depth of 150 mm. From Table 6.2, it can be seen that the pipe crown deflection (permanent) for the cast iron pipe is estimated to be 2.3 mm. By this procedure, we can predict the material response of the buried structure by performing a reduced shock tube experiment with appropriate scaling functions.

Since factors like prototype diameter, stiffness ratio and weight of the TNT explosive influence the scaling function, finding the scaling function is not straightforward. To reproduce an explosion of certain charge at a specific altitude, the scaled blast wave is generated in the laboratory with suitable configuration of shock tube. However, this takes a series of pilot runs that involves varying the bursting pressure P_4 , changing the length of the driven and driver section of the shock tube to achieve the blast wave parameters.

Vertical shock tube, the test facility used in the present study is capable of simulating air-blast wave condition with scaled blast distance, Z value spanning from 1.49 to 2.29 m/kg^{1/3} and peak overpressure varying between 0.4 and 1.6 MPa (Fig. 6.3).

With the help of scaling laws, shock tube-based experimental setup is a potential tool for studying broad range of blast wave conditions.

6.6 Numerical Simulation and Discussion

Numerical simulations are performed to understand in great detail, the impact of the air-blast wave on the buried pipe. The numerically computed results are in turn used to verify the dimensional analysis data obtained from the reduced-scale experiment using shock tube. Numerical simulations are carried out for two pipe models; the pipe diameter, the burial depth and the spherical air-blast wave test condition differ from one case to the other. However, the material properties of the both the models are the same.

The two pipe models are chosen such that the test case 1 corresponds to the variables from the shock tube experiment, whereas the test case 2 represents the dimensional analysis parameters for the scaling factor, $\lambda = 2$. Table 6.2 lists the input variables that comprise the dimension of the pipe, material properties of the pipe and the sand, relative density of the sand deposit, height of the explosion from the surface and weight of the equivalent TNT explosive.

The numerical simulation is performed using the commercially available finite element code, Abaqus/Explicit 6.12 (Abaqus 2009). A three-dimensional mesh is generated using 3-noded linear triangular shell element (Abaqus S3R) to model the pipe and 8-noded hexahedral linear brick elements (Abaqus C3D8R) are used for modelling the sand deposit. Figure 6.6 shows the three-dimensional mesh model of the buried pipe and the surrounding sand deposit. To model the sand medium as close as possible to the experiment, elastic perfectly plastic Mohr–Coulomb material model is chosen. On the other hand, an elastic–plastic material constitutive law is employed to model the pipe.

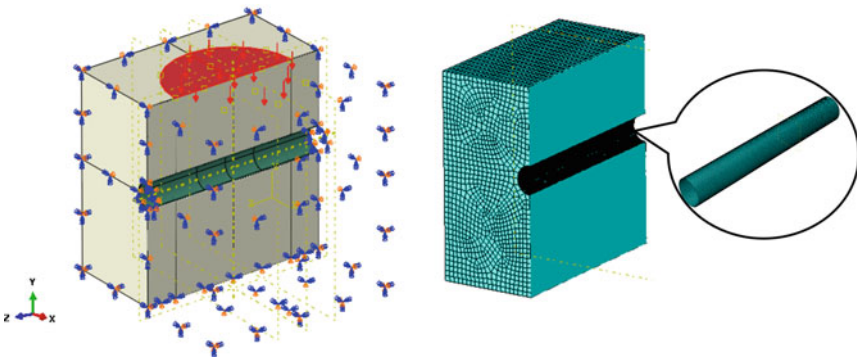


Fig. 6.6 Abaqus model showing mesh details of the sand deposit and the buried pipe

The sides of the sand deposit in the test chamber are imitated in the numerical simulation by roller support boundary conditions. The pipe ends are marked with fixed end boundary condition. To model the interface between the sand and the pipe, surface–surface contact approach is used, and to model the frictional interface between the sand and the outer surface of the pipe, the Coulomb friction model ($\phi' = 17^\circ$) is utilized. The material properties of the pipe (aluminium) and sand deposit are obtained from simple laboratory tests. The sand used in the present study has Young's modulus, E of 15 MPa, Poisson's ratio, ν of 0.3, cohesion, c of 0 kPa. The friction and dilation angle of the sand sample are 35° and 24° , respectively. A tensile test performed on the aluminium pipe used in the study revealed an elastic modulus, E_{al} of 68.9 MPa and Poisson's ratio, ν of 0.33. For the aluminium pipe, the yield stress is computed to be 40 MPa, proportional to 0.2% strain. Similarly, pipe of test case 2 is made of cast iron ($E_{ci} = 140$ MPa) and has an inner diameter of 47.5 mm and an outer diameter of 50 mm. The cast iron pipe has a flexural rigidity, EI of 29,818.3 N m². The material properties of cast iron used in computing the flexural rigidity are taken from Liu (2009).

The blast loading conditions are simulated in Abaqus by using the empirical equations based on the experimental data of Kingery and Bulmash (1984). ConWep (Conventional Weapons effects), a blast function code in Abaqus, incorporates a set of equations, which estimates the air-blast variables from spherical airbursts. Earlier, the results obtained from simulations using ConWep have been in good agreement with the experimental results from the field involving explosives (Henchie et al. 2014; Hyde 1988; Spranghers et al. 2013). Furthermore, the shock tube blast parameters (in Sect. 6.3.2) determined by the higher-order polynomial coefficient (Shin et al. 2014) are derived by comparing with the empirical data of Kingery and Bulmash (1984). For the simulation, equivalent mass of TNT for spherical airbursts and the altitude of explosion from the ground surface are given as inputs for the ConWep function. For case 1 and 2, the TNT mass equivalents are 20 and 160 kg, and stand-off distances from the detonating source to the ground surface are 5 m and 10 m, respectively.

Figure 6.7 shows the displacement–time response of the pipe crown for test case 1 and 2. From the figure, it can be seen that the pipe initially encounters a maximum deflection and then undergoes permanent plastic deformation. For test case 1 and 2, the peak deflection of the pipe crown is determined to be 1.58 mm 3.34 mm, respectively. Similarly, the permanent plastic deflection at the centre of the pipe crown is estimated to be 1.18 mm for test case 1 and 2.41 mm for test case 2. It is highlighted that the numerically simulated residual displacement values agree well with the values obtained from the experiment and predicted through dimensional analysis (dashed line in Fig. 6.7). The maximum axial strain is observed through numerical simulation at $L/3$ on the crown is 751 micro-strain for the test case 1. These values compare very well with the experimental results and hence prove the adequacy of numerical simulation (Fig. 6.5). The numerically generated displacement contours of the pipe for test case 1 and test case 2 are depicted in Fig. 6.8; in the figure, the contours indicate the permanent plastic deformation that the pipe underwent during the blast.

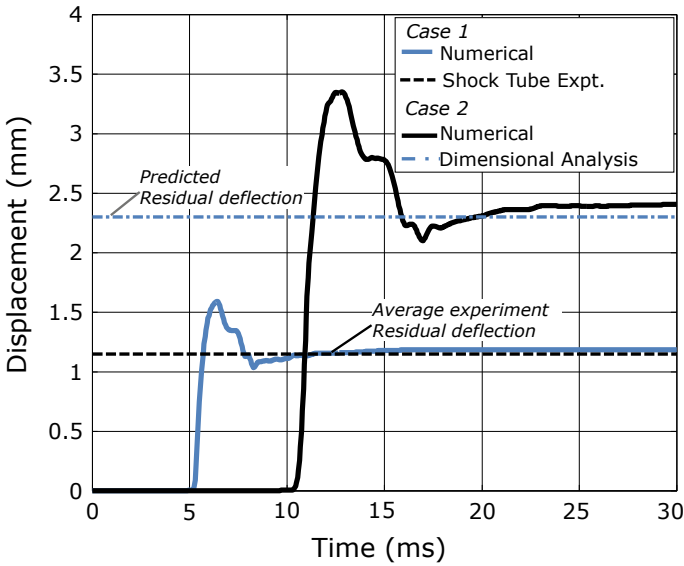


Fig. 6.7 Displacement–time history captured at the crown centre of the pipe for case 1 and case 2

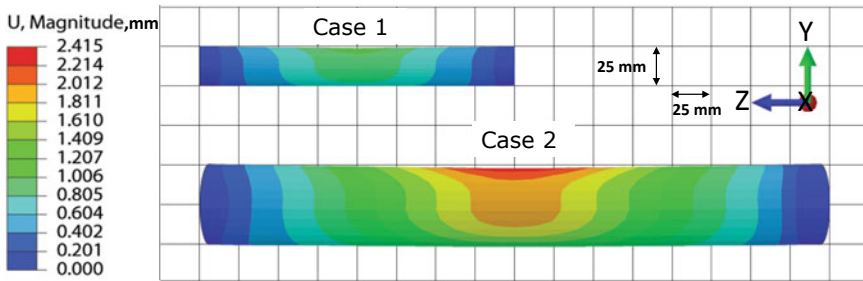


Fig. 6.8 Displacement contours of aluminium and cast iron pipe of test case 1 and 2, respectively

The numerical simulations evidently show that for studying the buried structures subjected to air-blast, shock tube-based experimental technique is a potential alternative tool. Moreover, the laboratory-scale method is safe compared to the filed experiments involving explosive. The shock tube employed in the current study can generate blast wave of medium intensity having maximum overpressure less than 2 MPa and for a scaled distance ranging from 1.49 to 2.29 m/kg^{1/3}.

6.7 Limitation

The shock tube-based experimental technique faces a serious limitation as it does not reproduce the thermal radiation effects that accompany the explosion. Hence, this method does not account for the influence of after-effects that include fragmentation and/or fusing of sand particles. In addition, crater formation is a characteristic phenomenon associated with the actual large-scale explosions and influences the destruction imparted to the structures beneath the ground surface. It is to be noted that such after blast effects are not considered in the present study. Therefore, for studying the response of buried structures exposed to low to moderate air-blast conditions, the small-scale shock tube-based experimental technique presented in the study is an effective method.

6.8 Summary

The work presented in this chapter uses dimensional analysis method in establishing the shock tube-based experimental facility for understanding the effects of spherical air-blast loads on buried structures. The outcome of this experimental work has illustrated the ability of the shock tube-based facility in generating blast waves. Since shock tube does not involve any explosives in producing blast waves, it is a safe and dependable method for studying the blast wave interactions with buried pipelines. An important experimental observation is that the buried pipe specimen subjected to blast wave impact suffered permanent residual deflection. In addition, finite element simulations are carried out to further understand the phenomena of air-blast loading on buried pipelines.

The residual deformation of the pipe determined from the experimental study agrees well with that obtained from the numerical simulations. Also, the data obtained from the numerical simulations for the scaled model match well with the data estimated through dimensional analysis method. Further, using the stress and strain values of the pipe obtained from the shock tube experiment, depth of burial of the structure can be determined and this is a valuable input for designing buried structures against blast loading conditions.

References

- Abaqus (2009) Abaqus/explicit users manual. Simulia Corp, Providence, RI, USA
Aune V, Fagerholt E, Langseth M, Borvik T (2016) A shock tube facility to generate blast loading on structures. *Int J Prot Struct* 7(3):340–366
Baker WE (1973) Explosions in air. University of Texas Press, Austin
Colombo M, di Prisco M, Martinelli P (2011) A new shock tube facility for tunnel safety. *Exp Mech* 51(7):1143–1154

- Colombo M, Martinelli P, di Prisco M (2013) Layered high-performance concrete plates interacting with granular soil under blast loads: an experimental investigation. *Eur J Environ Civ Eng* 17(10):1002–1025
- De A, Zimmie TF (2007) Centrifuge modeling of surface blast effects on underground structures. *Geotech Test J* 30(5):100656
- De A, Morgante AN, Zimmie TF (2016) Numerical and physical modeling of geofoam barriers as protection against effects of surface blast on underground tunnels. *Geotext Geomembr* 44(1):1–12
- Henchie TF, Chung Kim Yuen S, Nurick GN, Ranwaha N, Balden VH (2014) The response of circular plates to repeated uniform blast loads: an experimental and numerical study. *Int J Impact Eng* 74:36–45
- Hyde D (1988) User's guide for microcomputer programs ConWep and FunPro, applications of TM 5-855-1. Fundamentals of protective design for conventional weapons. Springfield, Virginia
- Kennedy J (1993) Oil and gas pipeline fundamentals. Pennwell Books, Oklahoma
- Kingery CC, Bulmash G (1984) Air blast parameters from TNT spherical air burst and hemispherical surface burst. Defence technical information center, Ballistic Research Laboratory, Aberdeen proving ground, Maryland, USA, Report BRL, 02555
- Kleinschmit N (2011) A shock tube technique for blast wave simulation and studies of flow structure interactions in shock tube blast experiments. Ph.D. thesis, University of Nebraska-Lincoln, Lincoln, USA
- Koneshwaran S, Thambiratnam DP, Gallage C (2015) Response of segmented bored transit tunnels to surface blast. *Adv Eng Softw* 89:77–89
- Liu H (2009) Dynamic analysis of subway structures under blast loading. *Geotech Geol Eng* 27(6):699–711
- Newman AJ, Mollendorf JC (2010) The peak overpressure field resulting from shocks emerging from circular shock tubes. *J Fluids Eng Am Soc Mech Eng* 132(8):081204
- Shin J, Whittaker AS, Amjad A, Aref AJ, Cormie D (2014) Air-blast effects on civil structures. State University of New York at Buffalo, Report, MCEER-14-0006
- Spranghers K, Vasilakos I, Lecompte D, Sol H, Vantomme J (2013) Numerical simulation and experimental validation of the dynamic response of aluminum plates under free air explosions. *Int J Impact Eng* 54:83–95
- UFC 3-340-02 (2008) Structures to resist the effects of accidental explosions. US Department of Defence. Washington, DC, USA
- Xu GF, Deng ZD, Deng FF, Liu G Bin (2013) Numerical simulation on the dynamic response of buried pipelines subjected to blast loads. *Adv Mater Res* 671–674:519–522
- Zhang L, Liang Z, Zhang J (2016) Mechanical response of a buried pipeline to explosion loading. *J Fail Anal Prev* 16(4):576–582
- Zhao X, Tiwari V, Sutton MA, Deng X, Fournery WL, Leiste U (2013) Scaling of the deformation histories for clamped circular plates subjected to blast loading by buried charges. *Int J Impact Eng* 54:31–50

Chapter 7

Granular Materials Responses to Buried-Blast Loading



7.1 Introduction and Previous Studies

For over a century, landmines are widely used to target armoured fighting vehicle and personnel from entering the enemy's jurisdiction. Serious injuries are caused to the leg, and in many cases, lives are lost due to the impact generated by landmine explosion. Researchers have been investigating the problem for a deeper understanding by performing a full-scale buried-blast test (Bergeron et al. 1998; Fourney et al. 2005; Taylor et al. 2005). However, physical test involving full-scale blasts is very expensive and is not feasible to have a visualization study because of the hazy environment around the explosion zone (Fox et al. 2011; Pickering et al. 2013). Numerous authors (Fox et al. 2011; Hlady 2004; Neuberger et al. 2007) have also performed simulated buried-blast and surrogate mine experiments using scaled explosive charges. The investigation primarily includes the effect of depth of burial (DoB), soil type, moisture content on the target placed at different stand-off distances (SoD) (Anderson et al. 2010; Pickering et al. 2013). However, very few authors have investigated soil behaviour during buried-blast loading. Roger (2015) has performed series of field experiments by using TNT explosives below the ground surface to understand the behaviour of dry and saturated soil. Bergeron et al. (1998) have performed experiments by using scaled C_4 explosive charges, the pressure and arrival time of air-shock (above the surface) and ground-shock (below the surface) were recorded over a range of stand-off distances. The shock wave propagation was found to be significant near the source of explosion and found to decelerate with distance. Karinski et al. (2012) and Tan et al. (2014) carried out numerical simulations predicting the attenuation of stress waves in soil upon a buried explosion.

The output from the buried-blast event, peak pressure and impulse is measured by using various techniques. Braid (2001) has used pitot tubes to measure the stagnation pressure at close proximity of the air-blast. Anderson et al. (2010) have used cable-pull potentiometer in their mine blast experiments, the total impulse transferred to the flat plate and V-shaped plate is determined from the maximum height

achieved. Pressure transducers (or multiple spike gauges) were also used to measure the peak pressure and impulse (An et al. 2011; Foedinger 2005). McShane et al. (2013) conducted series of experiments using Kolsky bar; the initial peak pressure and transient phase were measured from the recorded strain gauge data. Clarke et al. (2015a) developed a reaction frame with Hopkinson pressure bars. The pressure—time response generated from the large-scale (1/4 scale) experiment has been used to generate spatial and temporal loading of an explosion event. A most popular and accurate mode of impulse measurement is carried out using vertical pendulum apparatus (Bergeron et al. 1998; Clarke et al. 2015b; Ehr Gott et al. 2011; Pickering et al. 2013). Impulse value can be identified as a potential index for the damage associated with the buried-blast.

In general, most of the available literature on the buried-blast focuses on the impulse imparted by the sand, but many fail to address the complex dynamics involved during the sand outburst.

Bergeron et al. (1998) studied in detail the ejecta flow characteristics by using a high-speed X-ray photography. The process involved in the various stages of the buried explosion is outlined below (Bergeron et al. 1998; Deshpande et al. 2009):

- (i) *Blast interaction phase*: Upon blast explosion, shock wave is transmitted into the surrounding medium which generates stress waves (compressive) in the soil.
- (ii) *Bubble expansion phase*: When the compressive wave reaches the surface, it reflects back as tensile wave (rarefaction wave). This tensile wave combines with detonation products and breaks open the surface of the soil, leading to a bubble formation with a hemispherical shaped soil cap.
- (iii) *Soil ejecta phase*: The soil cap eventually collapses followed by the expansion of the soil ejecta in the shape of an inverted cone.

In a more recent study, as an alternate to conventional experiments using explosive charge, McShane et al. (2013) developed a scaled buried charge simulator (BCS). The BCS was found to be successful in generating the second and third phase of buried-blast, which involves dynamic flow of the sand. However, it is uncertain as to whether the first phase was considered in the simulator. The simulator was operated by a sudden release of the compressed nitrogen gas from a large cylindrical chamber (80 mm long) to a smaller chamber (20 mm long) and then to the sand layer. A CFD analysis (using Ansys-Fluent) was performed for the above-mentioned test configuration. It was found that neither shock wave nor blast wave was formed at the exit of smaller chamber. Hence, the blast simulator would ideally generate high-pressure gas flow, without a shock front. This exhaust gas flow disperses the buried sand and forms sand scatter over the surface. BCS has failed to incorporate the interaction of a blast wave with the sand deposit. Also, experiments performed by McShane et al. (2013) were considered very close to the sand surface (DoB = 15 to 30 mm).

The research work presented in the subsequent section aims at developing a similar test facility by accommodating a shock tube in the test assembly. The shock tube is capable of generating wide range of blast waves, representing a near-ideal explosion

(Courtney et al. 2014). The sand ejecta phenomenon is analysed over large burial depths, by providing qualitative and quantitative insights of the sand ejecta mechanism. The study also aims at examining the wave propagation in and around the blast source, which would reveal the attenuation behaviour of the sand and its influence over crater formation. Peak pressure measurements are obtained using fast-response pressure transducers, while the impulse is measured using a vertical impulse pendulum. A parametric study is carried out by varying the depth of burial ($DoB = 32$ to 64 mm) to assess the target response (pressure and impulse) over a range of stand-off distances (SoD).

7.2 Experimental Setup

A schematic diagram of the developed shock-driven sand test facility (SSTF) is shown in Fig. 7.1. The major components of the test facility include: (1) table-mount shock tube, (2) cylindrical test chamber and (3) instrumentation (pressure transducers and impulse measurement device).

The complete assembly of the test facility is shown in Fig. 7.2. A detailed description of TST has been already mentioned in Sect. 3.2.3; however for completeness, some specific details of TST are discussed here. The TST is mounted vertically such that the driven section is facing upwards and into the sand test chamber of the test facility. The shock tube (TST) is provided with two diaphragm mounting sections, primary diaphragm separating the driver and driven sections and the secondary diaphragm separating the driven section and the sand test chamber. Mylar[®] sheet is used as the primary diaphragm and a tracing paper (60–65 GSM) is used as the secondary diaphragm. The thickness of paper diaphragm is chosen such that it has minimum effect on the blast wave profile and the paper also must withstand the overburden pressure exerted by the sand. In order to record the generated blast wave, the open end of the driven section of TST is closed by a flange with an embedded piezoelectric pressure sensor, P_5 . When the TST is mounted in the test facility containing sand test chamber, end flange is removed and replaced by a paper diaphragm, and sensors P'_5 are mounted immediately after the paper diaphragm. A typical blast wave signal recorded from the P_5 and P'_5 pressure sensors are shown in Fig. 7.3.

A blast wave with a spherical shock front is expected to radially emanate from the open end of the shock tube (TST) into the sand bed, driving the sand particles out of the sand chamber. Shadowgraph technique is used for the visualization of the emanating blast wave. Figure 7.4 shows the shadowgraph image of the blast wave emerging from the open end of the shock tube (without overburden sand). A leading hemispherical shaped shock front is followed by a turbulent plume of compressed gas mixture (driver and driven gas) along with the ruptured pieces of the paper diaphragm. The speed of the blast wave in the open atmosphere is observed to be supersonic, travelling at a velocity of 375 m/s. The hemispherical blast wave profile closely resembles that of any open field explosion on a semi-infinite medium (earth). However, the blast wave generated is considered to be of low-moderate strength, with relatively low driving pressure (behind shock front).

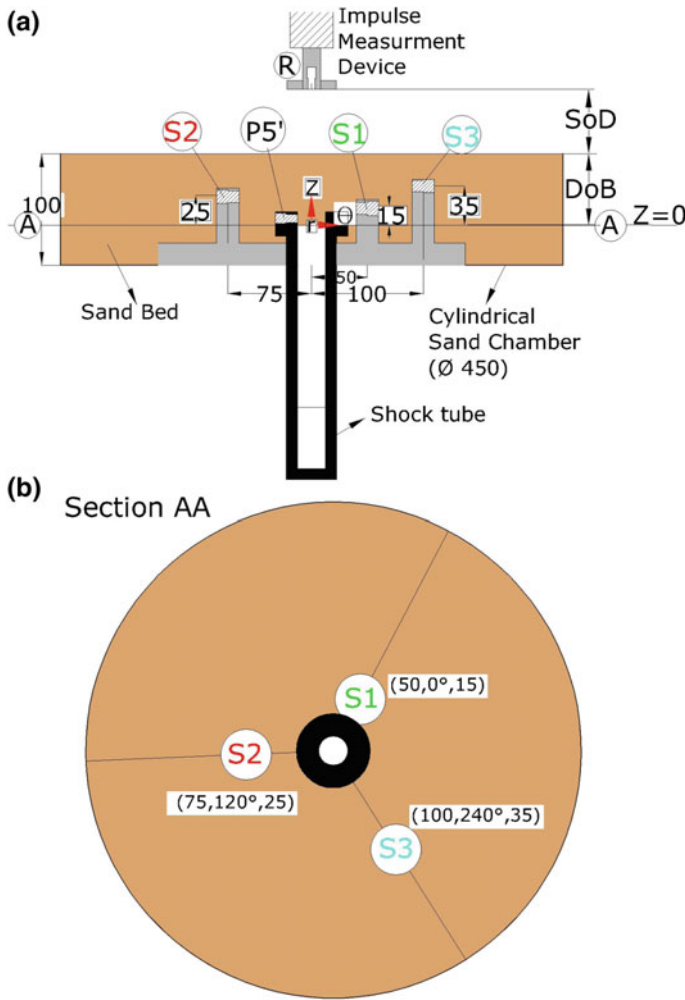


Fig. 7.1 A schematic overview of the shock-driven sand test facility: **a** cross-sectional view of the simulator, showing the position of the buried sensors for DoB 64 mm and **b** plan view of section AA (all dimensions given are in mm)

7.2.1 Test Chamber and Sample Preparation

The cylindrical sand test chamber has a capacity to prepare a sand bed of depth of 100 mm and 450 mm of diameter. A larger diameter of the test bed is chosen such that the boundaries had no influence on the wave propagation and the crater width. The shock tube (TST) assembly is connected underneath the sand chamber, such that the blast wave exits into the sand chamber. Different DoB cases are constructed by using appropriate spacer bars to position the shock tube opening end.

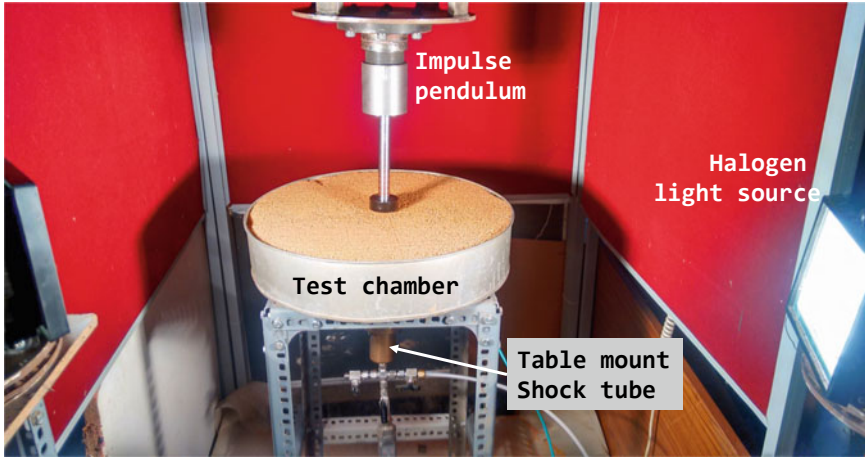


Fig. 7.2 The complete assembly of shock-driven sand test facility

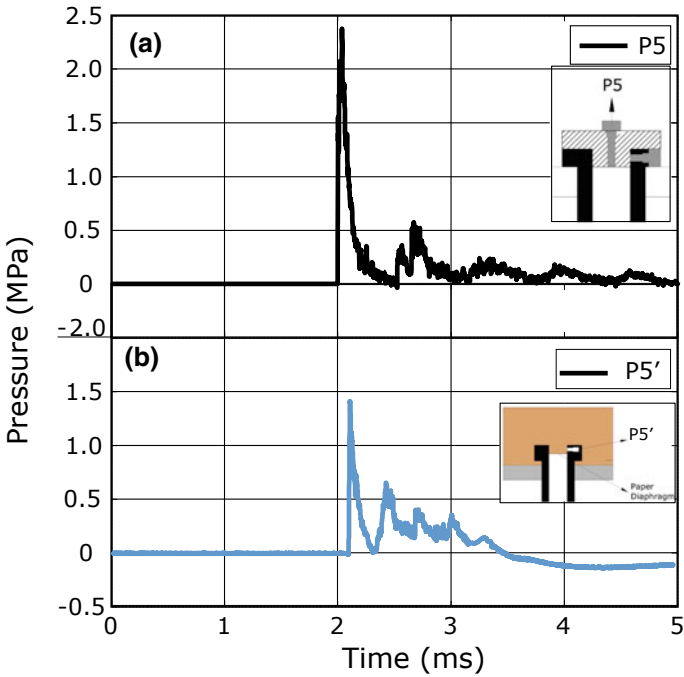
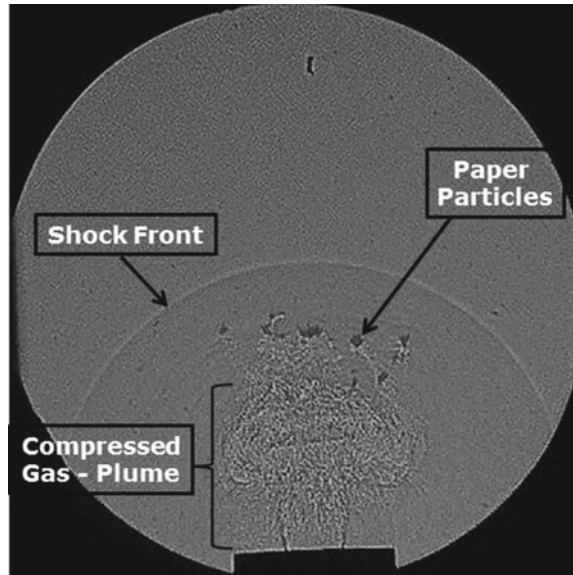


Fig. 7.3 Typical pressure signal recorded from TST: **a** P_5 sensor of blank test; **b** P'_5 sensor during buried-blast experiment

Fig. 7.4 Shadowgraph image at the open end of the shock tube (TST)



Same fine sand is reported in Chap. 5 is considered in this study. The gradation property of the sand and the grain size distribution curve is already shown in Chap. 3. Prior to each experiment, a sand bed of 100 mm depth is prepared by using sand pluviation technique. This method helps us in delivering repeatable sand layer deposits over a large area. In the present study, the sand bed is prepared with an approximate relative density of 45% which corresponds to dry density of 1566 kg/m^3 .

7.2.2 Instrumentation

7.2.2.1 Embedded Pressure Transducers

In order to measure the pressure–time response around the blast, three piezoelectric pressure transducers are embedded inside the sand bed. The three transducers are spaced apart 120° to each other and radially increasing at an offset of 25 mm in radius from the ID of the shock tube. All the pressure signal data are captured with a sampling rate of 500 kHz using a DL750 Yokogawa scope recorder. In addition, pressure signal is also measured at the exit of the shock tube (P'_5). The schematic diagram displaying the position of the transducers, S_1 , S_2 , S_3 and P'_5 is shown in the overview diagram of the shock-driven sand test facility (Fig. 7.1). A photograph of embedded transducers in the sand chamber is shown in Fig. 7.5a. The transducers arrangement is ensured to record the spherical outward movement of the blast wave.

In order to measure the peak pressure of the sand discharge ejecting out, a transducer 'R' is mounted on a rigid target frame, which is connected to a vertical actuator.

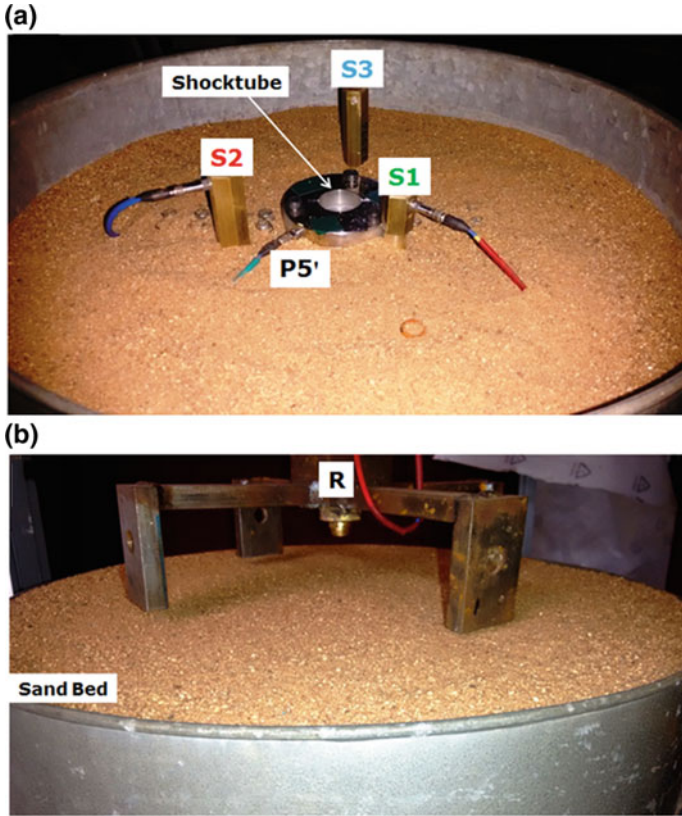


Fig. 7.5 A photograph of the sand bedchamber showing the positioned pressure transducers: **a** buried sensors, **b** overhead sensor

The target frame is placed at varying SoDs and aligned such that the sensor is pointing towards the axis of the buried shock tube. The pressure measured by sole transducer ‘R’ is expected to be highly localized and includes the pressure exerted by both the gas cloud and the particle impact. However, this peak pressure value will give an indication of total pressure imparted to the targets upon buried-blast loading.

$$I = \int_0^{t_d} P(t)dt \tag{7.1}$$

Subsequently, impulse imparted to the fixed target is calculated from the pressure–time data recorded by transducer R, using Eq. (7.1), where t_d is the positive pressure phase duration. The photograph of the rigid frame along with the transducer ‘R’ is shown in Fig. 7.5b. Measuring impulse from the localized pressure data

might not be accurate enough. In order to obtain more reliable data, the impulse measurements are also carried out using a simple impulse pendulum.

7.2.2.2 Vertical Impulse Pendulum

The vertical pendulum is made up of two components, linear bearing and a piston. The linear bearing is fixed firmly into the solid cylindrical block which is in turn bolted to the rigid target plate. The linear bearing is provided with anti-friction stainless steel ball bushings. The cylindrical shaft of the piston is inserted into the linear bearing, such that the circuit balls in the bearing comes in rolling contact with the shaft. The shaft is made up of hardened steel (SS 440), coated with ceramic aluminium alloy, making it an ideal surface finish with least coefficient of friction. The shaft travels axially back and forth along the bearing. The upper end of the shaft is clamped with a *c*-clip and the bottom end is connected to cylindrical piston head. For ensuring repeatability, all the experiments are carried out with two different piston mass, 0.634 and 0.534 kg. The height of the target frame is varied axially with the help of a vertical actuator (with an accuracy of 1 mm). The pendulum assembly is aligned and centrally placed along the axis of the shock tube with the piston head placed at a SoD from the top surface of the sand bed. The details of the vertical impulse pendulum are shown in Fig. 7.6.

When the sand ejecta strikes the piston head, the momentum is transferred to the piston head. The piston accelerates upward attaining a maximum height and then decelerates due to gravity. The maximum vertical displacement (h_a) of the pendulum is captured using a high-speed camera (Phantom V310 with Nikon 70–210 mm lens; images are captured with an exposure of 90 μ s at 11,000 frames per second). The

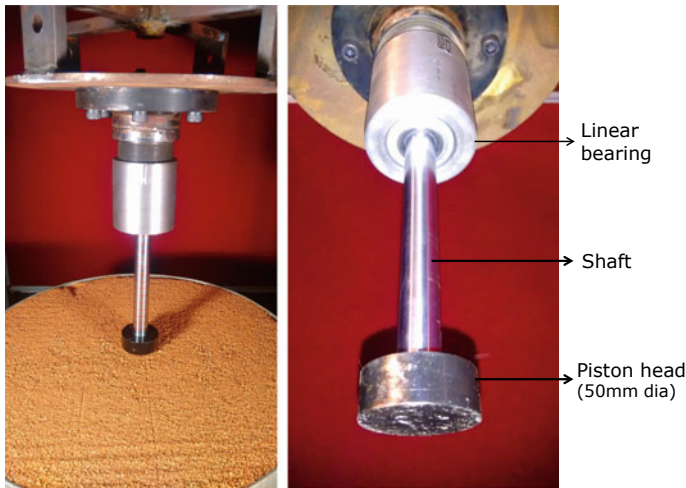


Fig. 7.6 A photograph of the vertical impulse pendulum

maximum impulse (I_{\max}) imparted to the pendulum is calculated from Eqs. (7.2) and (7.3), where V_j is the velocity of the piston, g is the gravitational constant (9.8 m/s^2) and m_p is the total mass of the piston head plus shaft.

$$V_j = \sqrt{2gh_a} \quad (7.2)$$

$$I_{\max} = V_j * m_p \quad (7.3)$$

7.2.3 Experimental Program

The experimental test series can be classified into three sections based on the objectives: (1) blast wave-sand interaction phenomenon is studied for three DoB cases (32 mm, 48 mm and 64 mm), (2) dynamics of sand ejecta is analysed for the mentioned DoB cases. (3) impulse and pressure measurements are carried out by varying SoDs (40 mm, 80 mm, 120 mm, up to 240 mm) for different burial depths (DoBs).

As outlined in the previous section, the components of the SSTF are assembled together and placed on a level ground surface. The primary diaphragm (Mylar[®]) and the secondary diaphragm (paper) are held in position with the help of the fasteners, ensuring leak proof conditions. The sand bed is prepared, and surface is levelled using a flat edge. The experimental setup is illuminated using four high-powered halogen lamps (1000 W), which serve as light source for the high-speed camera. The shock tube is operated by rupturing the Mylar[®] diaphragm using high-pressure helium gas in driver section. A blast wave is formed at the exit of the shock tube and travels further into the sand deposit by rupturing the paper diaphragm. Subsequently, the camera and pressure transducers are triggered (by P'_5 signal); the visual and voltage measurements are recorded. Similar experimental procedure is carried out for different combinations of DoBs and SoDs. It is to be noted that, for the experiments involved with the diagnosis of sand ejecta, the embedded sensors (S_1 – S_3) are removed and all the experiments are performed minimum twice to ensure test repeatability.

7.3 Experimental Results

7.3.1 Pressure–Time History Around Blast-Sand Interaction

The pressure (stress) variation recorded by the buried transducers, P'_5 , S_1 , S_2 and S_3 for three DoB cases is shown in Fig. 7.7. The P'_5 signal corresponds to the in-sand pressure measurement; a peak overpressure of about 1.4 MPa with a positive phase duration of 1.5 ms is recorded immediately at the exit of shock tube. Though the peak pressure amplitudes obtained are significantly lower when compared to

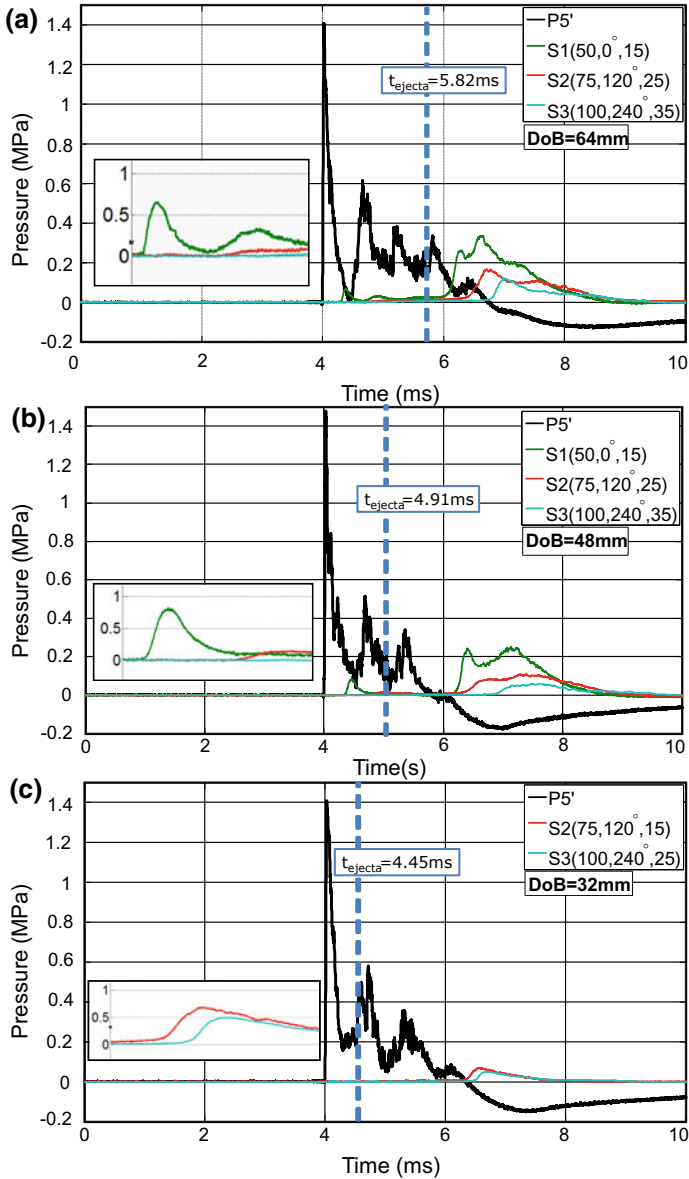


Fig. 7.7 Pressure–time histories recorded at of gauges P'_5 , S_1 , S_2 and S_3 for three different cases: **a** DoB = 64 mm; **b** DoB = 48 mm; **c** DoB = 32 mm (inset figure: enlarged portion of the initial peaks)

Bergeron et al. (1998), the blast wave features of P'_5 descriptively match well with their ground shock pressure profile.

The energy released from the blast wave-sand interaction is transmitted either as shock wave or stress wave into the surrounding sand medium. The formation of shock wave or stress waves in the medium depends on the intensity of the blast wave (energy released) and the acoustic impedance of the medium (for propagation). For all three DoB cases in Fig. 7.7, a well-defined shock front is identified very close to the shock tube exit (P'_5). As the shock front propagates through the sand, it attenuates with distance and reduces to low intensity stress wave. Referring to Fig. 7.7a, b, two distinctive events are observed over a period of 6 ms, the first event includes the passage of the stress wave, marked by the presence of initial pressure peak (see S_1 signal in inset Fig. 7.7, S_1 adapter is below the burial depth for 32 mm case). Under these conditions, the stress wave further traverses vertically and disturbs the surface of the sand bed. This event is captured using high-speed camera and the time of initiation of surface disturbance is displayed as a dotted line (t_{ejecta}) in Fig. 7.7. The radially attenuating stress wave has diminished across transducers S_2 and S_3 . Meanwhile, the second event begins with the expansion of the compressed gaseous product (mixture of helium and air). Three distinctive peaks of S_1 , S_2 and S_3 are observed with gradual rise to the peak and decreasing over a long period (termination of the event). The pressure amplitude of the second event is found to be larger than those associated during the first event (similar trends were numerically observed by Tan et al. (2014)). Further observing the initial period of the signal, there is no trace of the rarefaction wave from the surface. It is believed either the intensity of the wave is too low or the wave effect is suppressed by the outgoing gaseous expansion.

7.3.2 Sand Ejecta

The images of the sand ejecta captured using high-speed camera are shown in Figs. 7.8, 7.9 and 7.10. Each figure shows nine photographs of the event captured at different time intervals. The important parameters which influence the pattern of the ejecta are the confinement effect and the depth of burial. The sand discharge experiments are carried out for three different DoB cases, 32, 48 and 64 mm. Figure 7.8 corresponds to a test case when DoB is equal to 32 mm, Figs. 7.9 and 7.10 correspond to test case of 48 mm and 64 mm DoB cases, respectively. Referring to 32 mm DoB case (Fig. 7.8), an expanding gas sphere accelerating outwards from the surface is observed at 2.5 ms (termed as ‘bubble expansion’ by Bergeron et al. (1998)). Further, the bubble slowly begins to collapse giving way to the sand particles. The inherent cohesion between the particles is lost with the increase in ordinate length and the sand particles emerge out in a radial pattern (termed as ‘expanding inverted cone’ by McShane et al. (2013)). In addition, dome-cap like formation is observed from $t = 10.1$ to 15.3 ms, which has traversed all along the axis of the chamber. It is this portion of the sand ejecta, placed immediately above shock tube that carries the maximum momentum. The sand density around the dome-cap is considerably

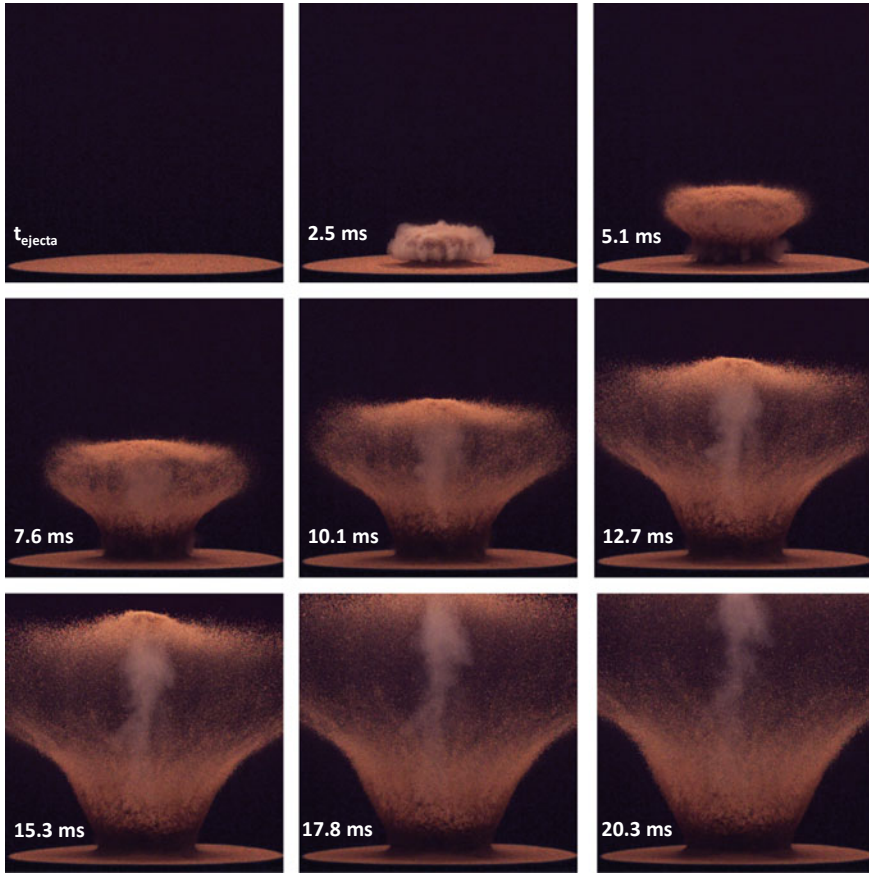


Fig. 7.8 Evolution of sand ejecta for 32 mm depth of burial (DoB) captured at different time intervals

higher compared to the other region of the radial cone. After a certain period ($t > 20$ ms), as the driving pressure gradually drops, sand dispersion reduces with time and eventually falls down due to gravity. The amount of sand ejected out of the sand chamber leads to the formation of a crater. A 183 mm circular disk-shaped crater is formed, which has perfectly centred itself to the opening of the shock tube.

The projection contours of the sand outburst are also plotted for each test case. The contour plots are generated by using image processing technique available in MATLAB. Sobel edge detection algorithm is used with a threshold value of 0.1. If the pixel gradient value is lower than this threshold, it is considered to have broken edges or noises (Efford and Nick 2000). The abscissa of the contour plot represents the diameter of the top surface of sand bed and the ordinate shows the vertical position of the dispersed sand particles. The projection contours of the sand outburst for 32 mm test case are shown in Fig. 7.11.

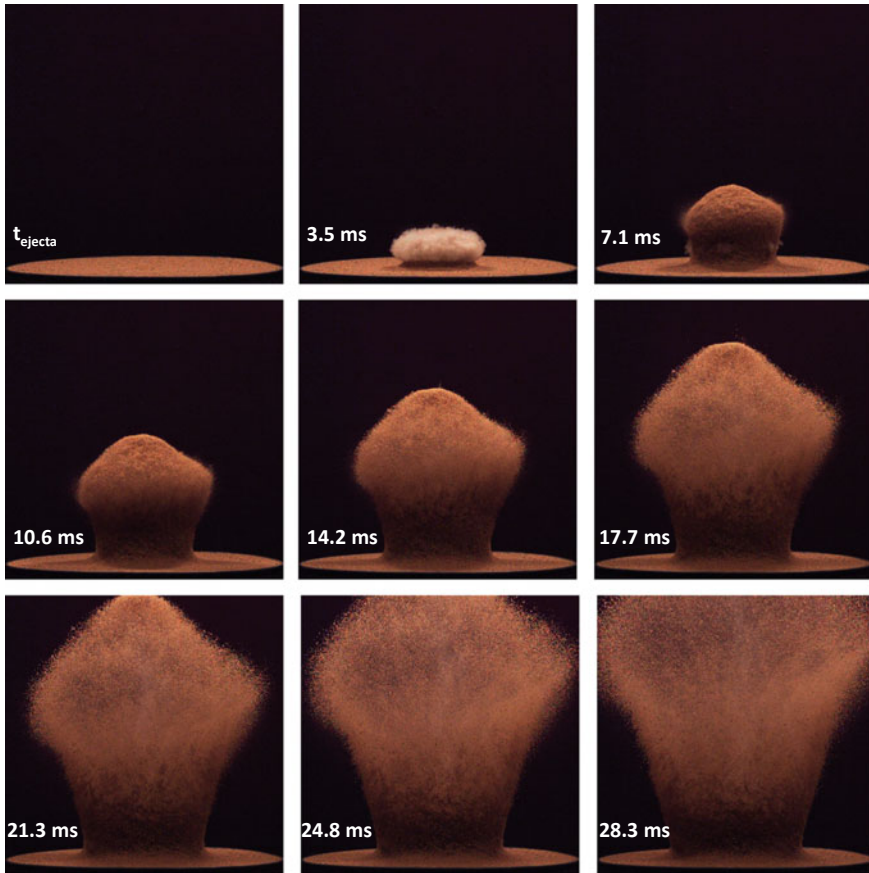


Fig. 7.9 Evolution of sand ejecta for 48 mm depth of burial (DoB) captured at different time intervals

Similar contour plots are generated from the images shown in Figs. 7.10 and 7.11 for the DoB cases of 48 mm and 64 mm case, respectively. The same initial test conditions are reproduced for all the test cases. The projection contours of the sand outburst for 48 mm and 64 mm test case are shown in Figs. 7.12 and 7.13, respectively.

By comparing the contours plots in Figs. 7.12 and 7.13 with Fig. 7.11, there are significant changes in the pattern of the sand ejecta. For instance, the presence of the inverted cone-like structure is replaced with a cylindrical column of sand. The increase in the confinement has restrained the sand from expanding radially; instead, the sand is directed vertically upwards. Noticeably, there is well-defined dome-cap ejecting out of the cylindrical formation. However, unlike in 32 mm DoB case, the dome-cap is attached to the ejecta formation in both 48 mm and 64 mm case. As the DoB increases, zone of influence of the outgoing pressure disturbance encompasses

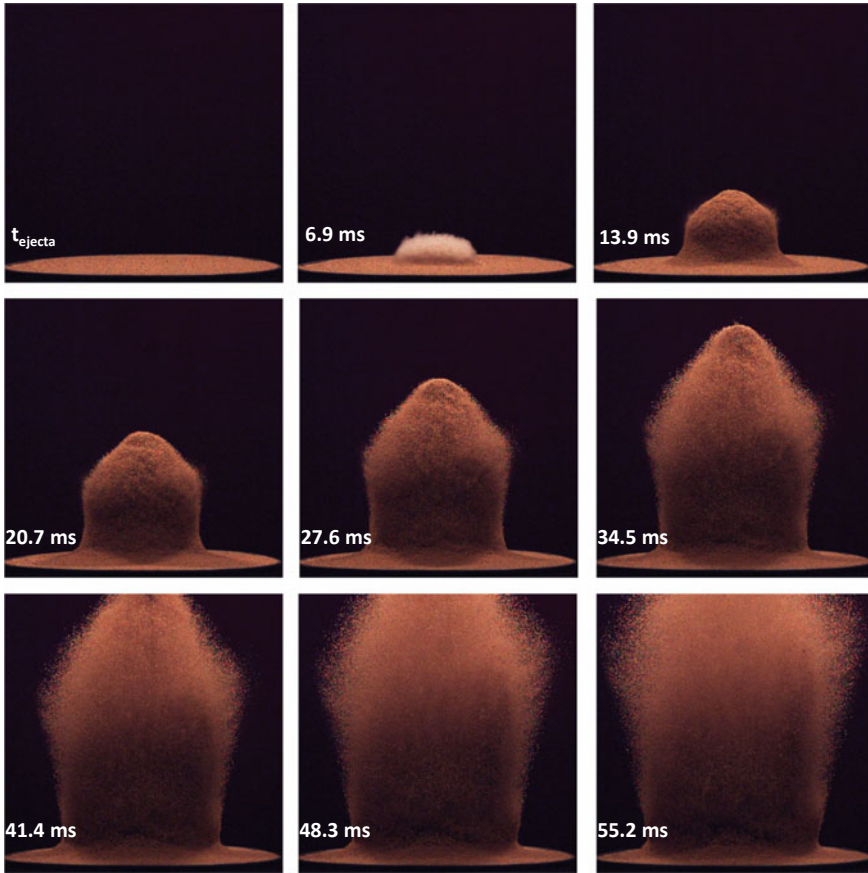


Fig. 7.10 Evolution of sand ejecta for 64 mm depth of burial (DoB) captured at different time intervals

large volume of the sand, resulting in higher sand mass flow out of the test bed. However, the driving pressure of the gaseous products being constant limits the flow rate of the sand. As a result, a dense annular region is formed at the base of the cylindrical column and large amount of the sand is dispersed out leaving behind huge cavity. The crater dimension for 48 mm and 64 mm DoB is 235 mm and 310 mm, respectively, and the crater slope is found to be steeper compared to 32 mm DoB.

The velocity of the ejecta is calculated from the contour plots. Successive high-speed images captured at an interval of 90 μ s are compared by measuring the distance traversed by the apex of the dome-cap. The velocity of the ejecta is found to increase from the bubble expansion phase to the dispersion phase. The greater part of the momentum is considered to be transferred from the bubble expansion to the dome-cap of the ejecta. In all the three cases, a clear well-defined dome is formed between Y-intercept of 100 and 200 mm. As a reference, the velocity measurements are made

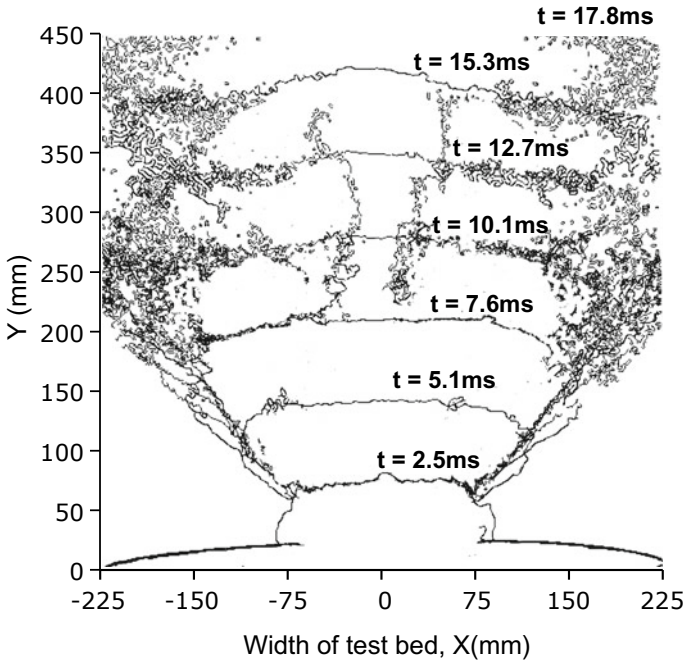


Fig. 7.11 A contour profile of the sand ejecta at different time instance for 32 mm DoB case

between Y -intercept of 125 and 425 mm. Interestingly, for DoB of 32 mm, the velocity is found to be almost constant (mean velocity, $v_x = 26.32$ m/s with standard deviation, $\sigma_x = 0.144$). The 48 mm DoB test resulted in velocity ranging from 18.07 to 21.31 m/s ($v_x = 19.71$ m/s, $\sigma_x = 1.06$) and lastly, the velocity range for 64 mm DoB is from 7.94 to 11.33 m/s ($v_x = 9.94$ m/s, $\sigma_x = 1.3$). From the trend of the velocity data, it is evident that there is clear reduction in the velocity as the DoB is increased. These data also infer, for burial depth close to the top sand surface (32 mm), the dome-cap isolates itself from the rest of the sand ejecta and travels at a constant velocity.

7.3.3 Pressure and Impulse Measurement

7.3.3.1 From Pressure Transducers on Rigid Target

The pressure measurements recorded from the overhead transducer ‘ R ’ for the 32 mm DoB case are shown in Fig. 7.14. By keeping the DoB constant, the height of rigid target frame is increased with an incremental SoD of 40 mm. The pressure–time history for different SoD shows similar distinctive spike-like structures. The spikes are attributed to the impact loading by the dome-cap. The signals are characterized

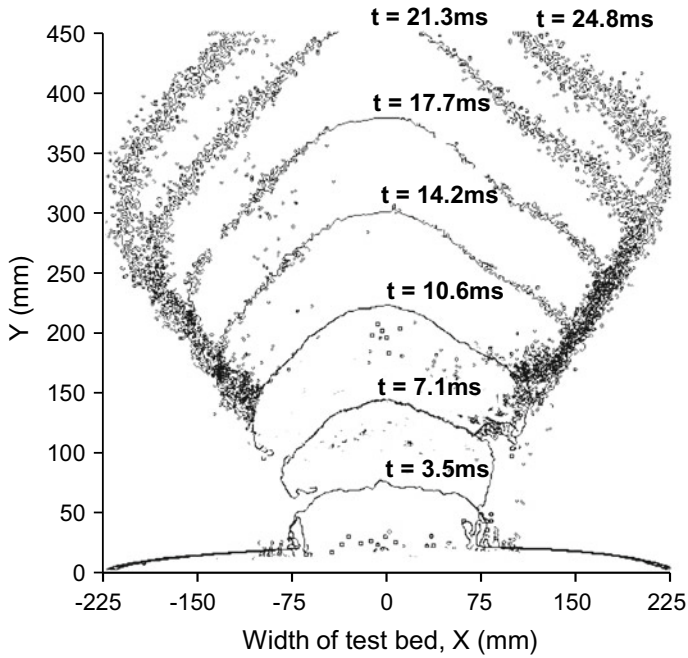


Fig. 7.12 A contour profile of the sand ejecta at different time instance for 48 mm DoB case

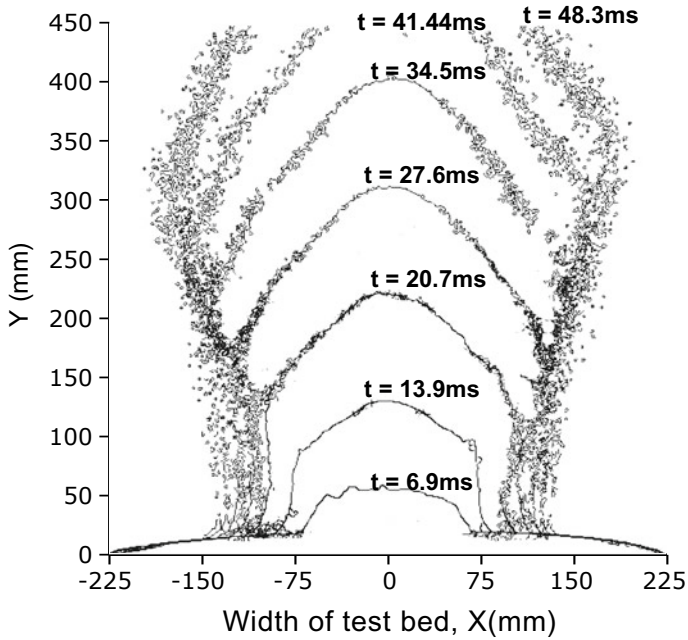


Fig. 7.13 A contour profile of the sand ejecta at different time instance for 64 mm DoB case

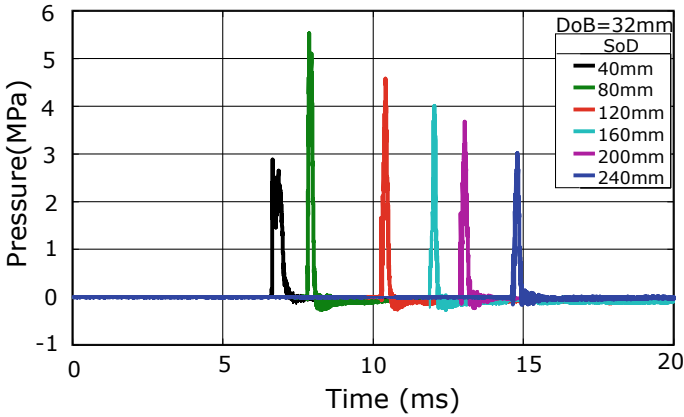


Fig. 7.14 Pressure–time histories recorded at overhead sensor *R* for SoDs varying from 40 to 240 mm

by a sharp rise, followed by a sudden drop. The maximum peak pressure is observed at SoD of 80 mm. At lower SoD (40 mm), the peak pressure is found to be lower and drops off at a steady rate with increase in the positive phase duration. The partial formation of the dome-cap with relatively low impact velocity can be accounted for to the low-pressure value. For the test cases with SoD greater than 80 mm, the peak pressure is found to decrease linearly with increase in the SoD.

The impulse calculated from the recorded pressure signals for the 32 mm DoB case is shown in Fig. 7.15. Two repeated test data are plotted, and a trend line is drawn by taking an average between them. There is a gradual decrease in the impulse

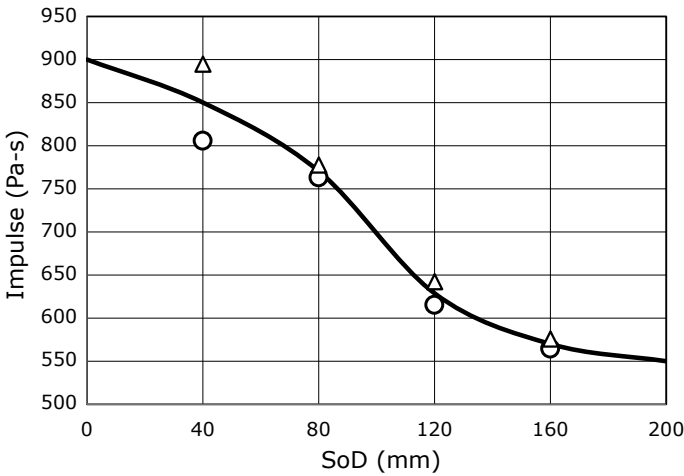


Fig. 7.15 Variation of the impulse with the SoD for 32 mm DoB case



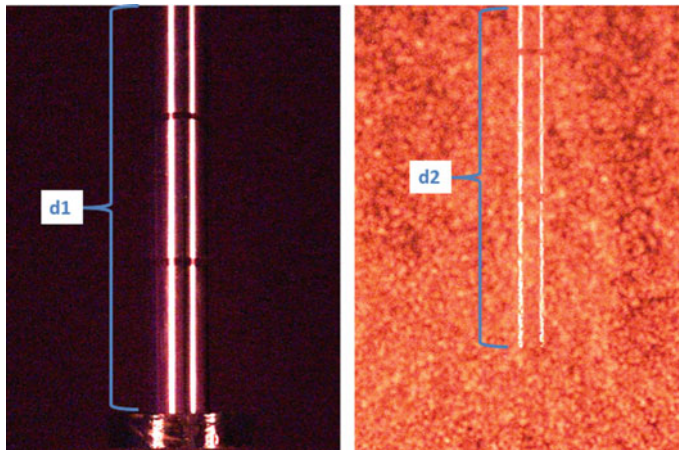


Fig. 7.16 Images of the shaft and piston of the pendulum captured (left) before and (right) after sand ejecta

value with the increase in SoD. Similar pressure and impulse trend were observed by McShane et al. (2013) for smaller depth of burial conditions. However, a single transducer placed at the target may not accurately predict the imparted impulse.

7.3.3.2 From Vertical Pendulum

The vertical impulse pendulum is used to measure the impulse imparted to the target. The typical images captured before and after the sand ejecta are shown in Fig. 7.16. The reflection of light from the shaft of the pendulum acts as the reference for calculating the height of travel by the piston. The impulse transferred to the target includes the effect due to the dome-cap, the gaseous mixture and the sand debris of the ejecta. Figure 7.17 is provided with the impulse data for all the three DoB cases, with increasing SoD (40–120 mm). For SoD larger than 120 mm, the sand debris completely masks the pendulum (shaft), obstructing the field of view of the camera. The impulse value is averaged between the two experimental test results of different piston mass. As expected, the impulse measured from the pendulum is found to be notably lower than the measurement made using the transducers.

The impulse imparted to the pendulum is observed to decrease with the increase in the stand-off distance (as observed in the transducer method for 32 mm DoB). Further, maximum impulse is observed when the target is closer to the sand surface, perhaps because of the presence of the ‘bubble expansion’ cloud. For a target placed at a SoD of 80 mm, the maximum impulse is observed for the DoB of 32 mm, and similarly for a target placed at 120 mm, the maximum impulse is found when the DoB is 48 mm. It is interesting to note that the maximum impulse transfer for a specific SoD is observed when SoD/DoB value is equal to 2.5. It seems reasonable to state

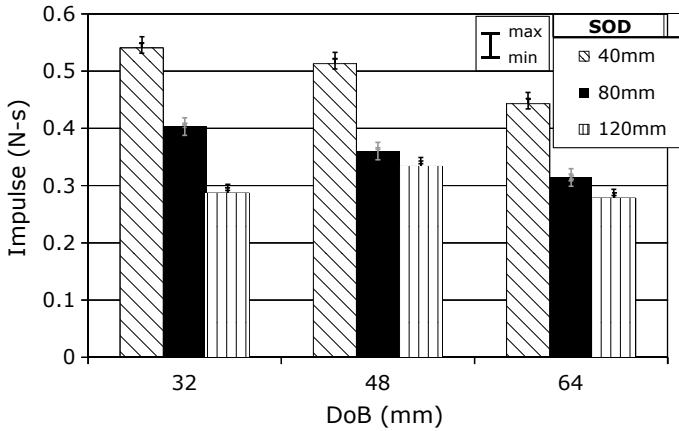


Fig. 7.17 Variation of the impulse with the SoD for different DoB (max. and min. values are shown within the standard bars)

the following hypothesis. When the ratio of SoD to DoB equals 2.5, the ejecta has consumed optimum crater volume to create a well-defined dome-cap. This dome-cap is coerced with utmost velocity (by gaseous products) to impart maximum impulse to the target. Further, experiments show a decrease in the momentum with increase in the overburden sand depth (>50 mm). This effect is termed as camoufler condition (Bergeron et al. 1998), where the blast wave and the gaseous products are completely contained by the sand.

7.4 Discussion and Limitation

A compressed gas-driven shock tube is used to generate blast wave in the sand deposit. In this section, the experimental results (peak overpressure) are compared with the available data in the existing literature on the buried landmine experiments (operated by using explosives). However, a direct comparison of experimental efficacy is not possible, due to the variability in the different parameters of the test conditions. Bergeron et al. (1998) and Roger (2015) performed buried explosion study using 100 g of C₄ explosive; subsequently, peak pressure data were recorded both below (in-sand) and above (in-air) the sand surface. The pressure measurements above the surface were done all along the centre of the buried charge, while the buried sensors were located deep below the source of detonation (Refer Bergeron et al. (1998) and Roger (2015) for exact location). Although the recording of the buried sensors of Bergeron et al. (1998) and Roger (2015) was not captured around the buried charge, their data can provide quantitative information on the pressure levels in sand and the stress waves generated by the detonation.

Figure 7.18 compares the results from the literature to the pressure data recorded



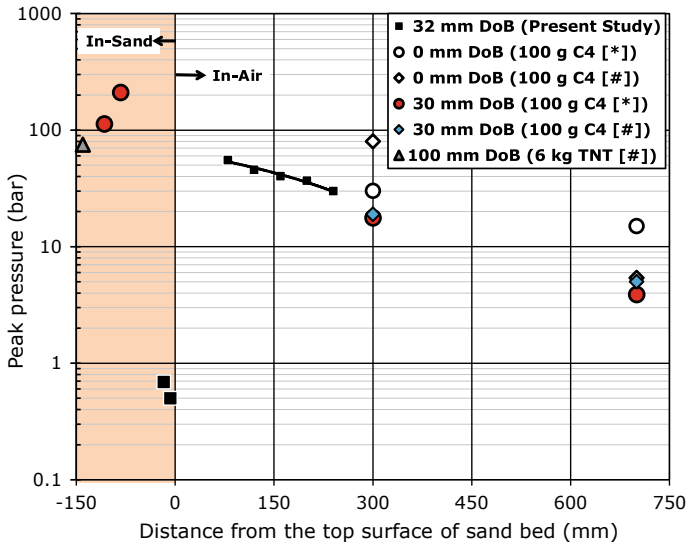


Fig. 7.18 Comparison of the test results from the present work with the results of experiments performed using explosives (*Bergeron et al. (1998), #Roger (2015)). The pressure values are shown in units of bars for easy comparison ($1 \text{ bar} = 10^5 \text{ N/m}^2$)

in the present study. When analysing the peak pressure values with the existing data, the pressure measurements made above the sand surface are observed to have a similar range and show a consistent trend with the increase in the SoD, confirming the validity of the present experiment. On the contrary, the peak pressure values in the sand are found to be significantly lower when compared to the tests performed using explosives. In fact, the present experimental values are off by an order of magnitude. Further, the velocities of cloud expansion are much lower than those found in the case of Bergeron et al. (1998). As a consequence, it is believed that pneumatically generated blast pressure is insufficient to create the effects of actual buried explosion in sand. The effects include the presence of shock front in the sand medium, high compression followed by rapid decompression, particle breakage and crushing, and the thermal radiation resulting from the detonation. However, examining the sand ejecta characterization results confirms that shock tube-based tool enables us to study later stages of buried explosion, the physical sand ejecta impact on the overlying targets. Hence, the present study is limited to the study of the dynamics involved during sand ejecta and assesses the resulting impulse transfer, induced by relatively low driving pressure of the blast wave.

The aim of this study is not to compare with real explosion, but to develop a laboratory environment for studying buried impact or blast loading mechanism. The study has attempted to experimentally characterize the different phases involved in the sand ejecta, during the interaction of blast wave with sand, followed by expansion of the driving compressed gas. Since the conditions in the shock-driven sand facility

are well-controlled and are equipped with advanced monitoring and diagnostic techniques, this would enable us in qualitative understanding of the behaviour of sand during buried-blast loading. Further, studies are needed to conclusively demonstrate the shock tube-based tool in simulating actual buried-blast explosions.

The buried-blast loading performed in the present study is limited to qualitative comparison with the landmines, the reason being relatively low driving pressure of the blast wave. The high pressure can be achieved by replacing the compressed gas-driven shock tube by a detonation-driven shock tube. The details of detonation shock tube are available in Janardhanraj and Jagadeesh (2016).

7.5 Summary

A shock tube-based facility is developed to generate buried-blast loading conditions. Since the facility is well-controlled and is equipped with advanced monitoring and diagnostic techniques, it has enabled us in qualitative understanding of the behaviour of sand during buried-blast loading. The experimental results are reported for blast loading imparted at three different burial depths (DoB), 32, 48 and 64 mm. The experiments are primarily focused to investigate the sand ejecta kinematics during blast wave interaction with the sand media and also to assess the variability of the imparted impulse transferred to the surface targets.

Dynamic wave propagation and the pressure distribution around the blast source have also been considered. Stress waves were found to attenuate significantly in the sand deposit and the peak pressure induced by the stress wave is much smaller than the rise in pressure generated by the gaseous products (mixture of compressed gases). The sand ejecta patterns are analysed in detail for various DoB cases. The peak pressure and impulse imparted to the targets are analysed from the measurements made using transducers and vertical pendulum, respectively, at varying SoDs. The depth of burial was found to have a greater influence on the amount of impulse transmitted to the target. The results obtained in this chapter also indicate that the crater dimensions (radius and the slope) increase with the increase in DoB.

References

- An J, Tuan CY, Cheeseman BA, Gazonas GA (2011) Simulation of soil behavior under blast loading. *Int J Geomech* 11(4):323–334
- Anderson CE, Behner T, Weiss CE, Chocron S, Bigger RP (2010) Mine blast loading: experiments and simulations. Southwest Research Institute, Report 18.12544/011
- Bergeron DM, Walker R, Coffey C (1998) Detonation of 100-gram anti-personnel mine surrogate charges in sand—a test case for computer code validation. Ralston, Alberta
- Braid MP (2001) Experimental investigation and analysis of the effects of antipersonnel landmine blasts. Defence Research Establishment Suffield, DRES SSSP 2001-188, Canada

- Clarke SD, Fay SD, Warren JA, Tyas A, Rigby SE, Elgy I (2015a) A large scale experimental approach to the measurement of spatially and temporally localised loading from the detonation of shallow-buried explosives. *Meas Sci Technol* 26(1):015001
- Clarke SD, Fay SD, Warren JA, Tyas A, Rigby SE, Reay JJ, Livesey R, Elgy I (2015b) Geotechnical causes for variations in output measured from shallow buried charges. *Int J Impact Eng* 86:274–283
- Courtney E, Courtney A, Courtney M (2014) Shock tube design for high intensity blast waves for laboratory testing of armor and combat materiel. *Def Technol* 10(2):245–250
- Deshpande VS, McMeeking RM, Wadley HNG, Evans AG (2009) Constitutive model for predicting dynamic interactions between soil ejecta and structural panels. *J Mech Phys Solids* 57(8):1139–1164
- Efford N, Nick (2000) *Digital image processing*. Addison-Wesley, Boston
- Ehrgott JQ Jr, Akers SA, Windham JE, Rickman DD, Danielson KT (2011) The influence of soil parameters on the impulse and airblast overpressure loading above surface-laid and shallow-buried explosives. *Shock Vib* 18(6):857–874
- Foedinger J (2005) Methodology for improved characterization of landmine explosions, SBIR phase-II plus program, Technical Interchange Meeting. Material Science Corporation
- Fourney W, Leiste U, Bonenberger R, Goodings D (2005) Explosive impulse on plates. *Fragblast* 9(1):1–17
- Fox DM, Huang X, Jung D, Fourney WL, Leiste U, Lee JS (2011) The response of small scale rigid targets to shallow buried explosive detonations. *Int J Impact Eng* 38(11):882–891
- Hlady SL (2004) Effect of soil parameters on land mine blast. In: 18th military aspects of blast and shock (MABS) conference, Bad Reichenhall, Germany
- Janardhanraj S, Jagadeesh G (2016) Development of a novel miniature detonation driven shock tube assembly that uses in situ generated oxyhydrogen mixture. *Rev Sci Instrum* 87(8):085114
- Karinski YS, Feldgun VR, Yankelevsky DZ (2012) Shock waves interaction with a single inclusion buried in soil. *Int J Impact Eng* 45:60–73
- McShane GJ, Deshpande VS, Fleck NA (2013) A laboratory-scale buried charge simulator. *Int J Impact Eng* 62:210–218
- Neuberger A, Peles S, Rittel D (2007) Scaling the response of circular plates subjected to large and close-range spherical explosions. Part II: buried charges. *Int J Impact Eng* 34(5):874–882
- Pickering EG, Chung Kim Yuen S, Nurick GN (2013) The influence of the height of burial of buried charges—some experimental observations. *Int J Impact Eng* 58:76–83
- Roger E (2015) Mines buried in dry and saturated soils: blast experiments, soil modeling and simulations. Ph.D. thesis, Université Grenoble Alpes
- Tan Z, Zhang W, Cho C, Han X (2014) Failure mechanisms of concrete slab-soil double-layer structure subjected to underground explosion. *Shock Waves* 24(5):545–551
- Taylor L, Skaggs R, Gault W (2005) Vertical impulse measurements of mines buried in saturated sand. *Fragblast* 9(1):19–28

Chapter 8

Role of Shock Waves in Geotechnical Applications



8.1 Introduction

The shock induced damage and transformation process finds many applications. Some of the general applications are listed in Jagadeesh (2008). Application pertaining to Geotechnical Engineering includes dynamic compaction, shock densification, mining, laser cutting and drilling of rocks, hydraulic fracturing, rejuvenation of depleted borewell, impact craters, etc. This chapter highlights some of the studies carried in the view of addressing a geotechnical problem with the help of shock waves. In addition to the specific problems mentioned in the previous chapters, some of the other important applications in Geotechnical Engineering are addressed in this chapter, namely: (1) shock fracking—alternative to hydraulic fracturing (2) prediction of shock induced brittle rock damage, (3) shock-wave-assisted pile-driving system and (4) increasing yield of a depleted borewell using shock waves. Some of the works on the above topic are still in conceptual stage and detailed results are not available at this time.

8.2 Alternative to Hydraulic Fracturing

The yield of the oil depends on the size and length of the fracture, which acts as carrying channel towards the wellbore. These existing fractures are often not sufficient enough for a good yield. In the present study, a new technique is proposed here to induce fractures in the shale rocks with the application of shock waves and thereby increasing yield of an oil well.

Hydraulic fracture technique comprises of a 'base fluid' which is mixed with sand or tiny ceramic spheres (called proppants) and with some chemical additives (Thallak 1991; Thallak et al. 1991). The mixture is then pumped into the well which leads to gas-bearing formations. The wells are generally drilled horizontally in a formation

to increase the length of the well casing that can drain gas from the formation. The fluid pressure is increased until the formation rock is hydraulically fractured. Once the rock is fractured and the proppants are delivered into the fractures (to allow the fractures to stay open), the fluid pressure in the well is reduced so that gas in the rock can flow through the newly formed fractures and into the well casing. The volume of fluids used in a fracking job might be as much as 2–8 million gallons per well with water and sand typically constituting about 99.5% of the fracking fluids.

8.2.1 Problems Involved with Hydraulic Fracturing

Hydro-fracturing is one of the popular techniques which are practiced in the defunct sites. However, this method is considered to be highly tedious process and has many environmental implications. Some of them are listed below:

- Huge amounts of water are used to break up gas-bearing rock formation.
- Huge amounts of polluted water are returned (flow back) to the surface after the process is complete. This water is polluted with chemicals, salts and even mild radioactivity. The polluted water contaminates the groundwater aquifer and also surface water resources.
- Because of the nature of the formation (Shale), water becomes incompatibility. Fracking fluid starts reacting with the minerals present in the formation and gets trapped in the reservoir, impeding the flow of gas into the well.
- On field resources employed for hydraulic fracture are huge. A large number of high-speed pumps, blender, storage tanks for water, etc.
- Fracking process has caused small earth tremors. Two small earthquakes of 1.5 and 2.2 magnitude hit the Blackpool area (UK) in 2011 following fracking.

8.2.2 Shock Wave Fracking

Shock wave fracking is technology based on the compressible flow nature of gases. Shock waves are essentially nonlinear waves that propagate at supersonic speeds. Across a shock wave, the static pressure, temperature and gas density increase almost instantaneously. Shock waves are efficient mechanisms of energy dissipation. These features of shock waves play a vital role in the fracking of reservoir rocks. Reservoir deposits like Shale are formed of smectite mineral. Because of the swelling property of smectite, use of water for fracking is ruled out considering the complication involved. Shock wave fracking has clear advantage in such situation, which does not allow the clay mineral to swell.

To generate strong shocks, the driver gas should have low density and low specific heat, considering these properties Helium and Nitrogen can be used as the base fluid. Since compressibility is inversely proportional to the viscosity of the fluid, for having

a stronger shock the base fluid chosen should have considerably low viscosity. Initial experiments were carried out using a vertical shock tube (VST), where the open end of driven section is connected to a triaxial confining chamber. The confining chamber is made of screw jack system, which is intended to apply low confining pressure on the test samples. A photograph of the experimental test setup is shown in Fig. 8.1.

The shock wave travelling at supersonic speed is impinging upon rock samples. High-impulse multiple-repetitive shock waves are targeted upon the shale rock to initiate fractures. In this region, stress wave generated by the shock wave impact exceeds the dynamic shear strength of rock sample, thereby several radial cracks are

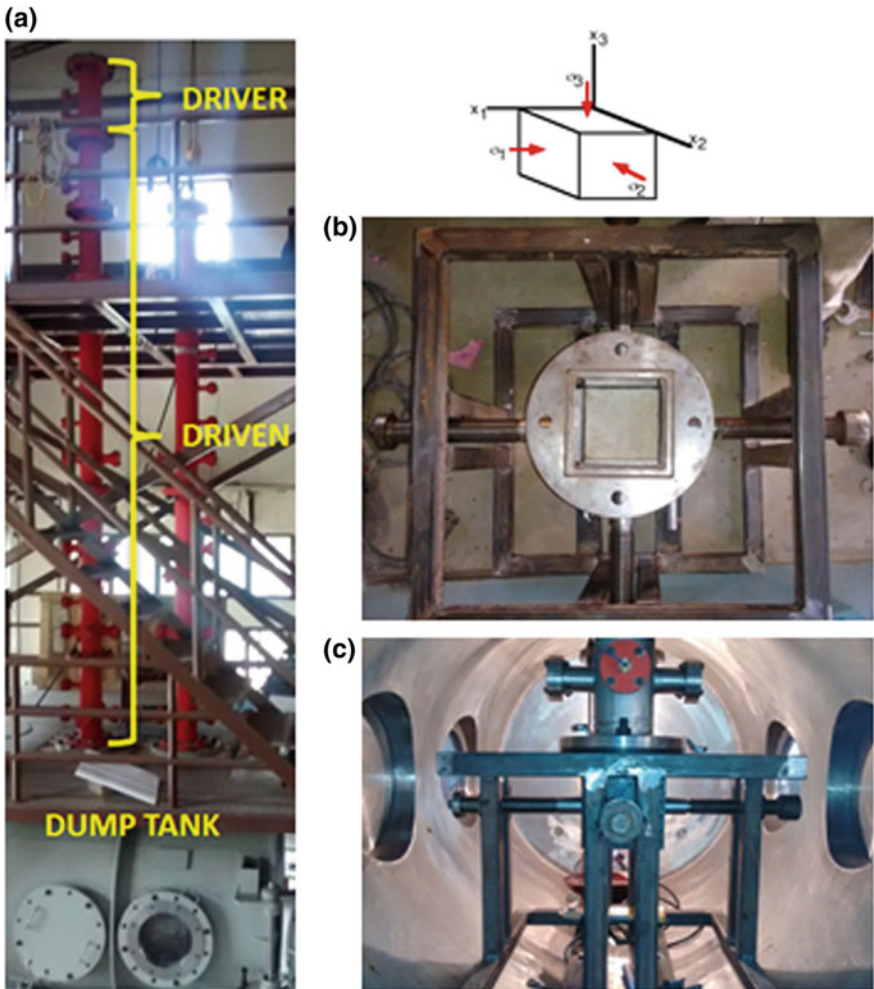


Fig. 8.1 a Vertical shock tube facility, b top view of the confining pressure chamber, c a side of the screw jack operated confining pressure chamber

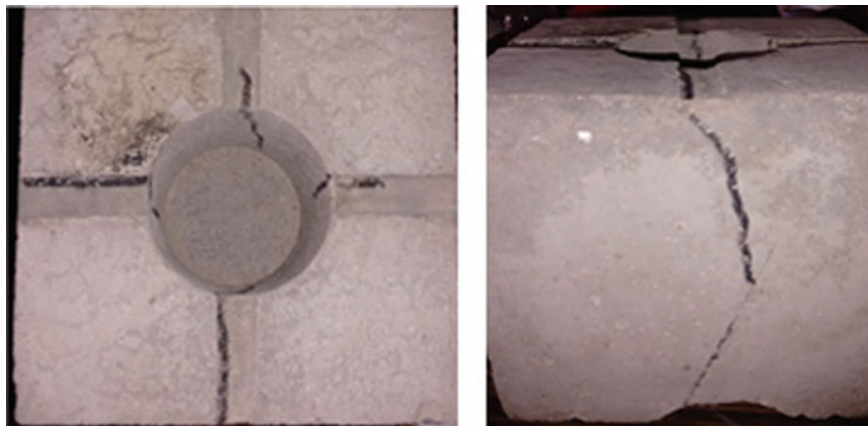


Fig. 8.2 Radial cracks generated in the test sample upon shock wave impact

proceeded towards the interior surface. These fractures provide high permeability flow conduits thus facilitating higher yield. At micro-level, nucleation and growth of voids also takes place, which further increases the permeability of the rocks. The cracks are generated inside the well bore and get propagated to the outer surface. The cracks observed in the preliminary investigation are shown in Fig. 8.2.

8.3 Shock-Wave-Assisted Pile Driving

Conventional pile-driving techniques using hammers in a marine and offshore environment are extremely large and cumbersome to handle. In such hostile climate, the existing technology can be very dangerous and involves lot of machinery to be mobilized. The piles are driven in the deep ground using either impact or vibratory hammers. Deep foundation is very expensive and laborious. Hence, new installation methods and associated machinery are being developed in order to minimize the efforts of mechanical operation and increase the efficiency of the pile-driving system. Massive amounts of energy can be generated by detonating explosions.

The explosion-driven pile-driving systems are also common in practise. In the present research, we intend to use the key components generated using an explosion, SHOCK WAVES. The overall of this study is to provide an alternative technology for pile-driving system by using shock wave energy. The new technique aims to improve the efficiency of pile-driving systems and can be considered as an economical alternative compared to the conventional hammer-driven pile techniques. The proposed research project is designed such that experiments carried out using the samll laboratory scale equipments generate enormous impact energy. The safety of persons working in offshore and inland infrastructures projects is of high priority. The logistics and machineries for operation in the proposed technology will be minimal.

8.3.1 Development of Laboratory-Scale Shock-Pile-Driving System

An alternative to conventional method of using explosives is by generating a shock waves in a controlled condition. As mentioned earlier, the shock tube is made up of two sections, driver section and driven section, which are separated by a diaphragm. On rupturing the diaphragm, series of compressive waves gets generated which further gets coalesced to form a single front called shock wave. It has been previously observed by many researchers that the major impact of the impact is due to the positive phase duration. In order to generate a positive phase blast profile using a shock tube, the plateau region in the shock wave profile has to be brought to zero-pulse duration. This can be achieved by changing the driver length of the shock tube or by changing the driver gas used in the driver section.

A small-scale shock tube is designed and built in the laboratory of soil mechanics, Department of Civil Engineering, Indian Institute of Science. This facility is operated at pressure up to 50 bar. Higher operating pressure is obtained by increasing the thickness of the diaphragm. The shock tube has been designed such that it can generate both shock wave and blast wave profiles. In order to do that, two different driver sections are fabricated—the smaller driver section (60 mm) is used for blast wave profile and longer section (120 mm) is used for generated shock wave kind of profile at the exit of the driven section. The photograph of the different parts of the shock tube used in the present study is shown in Fig. 8.3.

The small-scale shock tube is held vertical using a *c*-clamp connecting system, and two horizontal ribs are provided to avoid the rebound of the shock tube upon diaphragm rupture. Exhaust valve is provided at the driver section and three sensors (provided by SEGS) are mounted at the driven section. The complete assembly of the setup is shown in Fig. 8.4. A pile model is inserted inside the sand deposit and made to project outwards such that the pile is aligned along the shock tube axis. While the driven pressure is kept at atmosphere conditions, i.e., 1 bar and the rupture

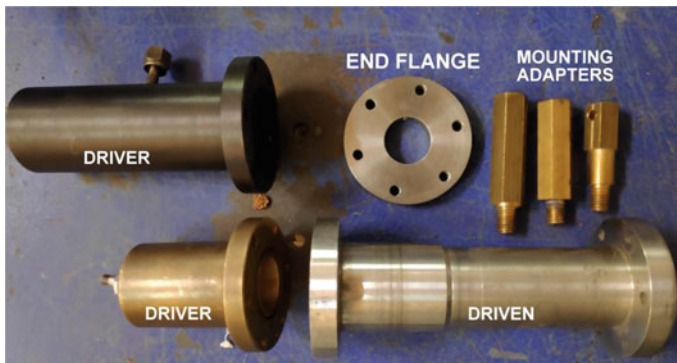


Fig. 8.3 Components of the shock tube fabricated to operate in shock and blast wave mode



Fig. 8.4 Small-scale vertical shock tube facility for pile driving, left: complete assembly of the setup; top right: instrumentation; bottom right: compressed nitrogen is injected into the driver section

pressure were recorded to be 10 bar of pressure. From the initial experiments, it was found that the pile had driven into the sand deposit for depth of 1.5 cm, upon three successive shots (Fig. 8.5).

8.4 Increasing Yield of a Depleted Borewell

An interesting experiment has been carried out by the authors and Prof. KPJ Reddy (Retd. Professor of Department of Aerospace Engineering, Indian Institute of Science, Bangalore) to increase the yield of a depleted borewell by using shock waves. The high pressure behind the shock wave travelling into the borewell acts normal to the walls of the borewell and helps in clearing the clogged-up water channels (fissures, fractures, etc.) present in rock formations and thereby allowing the water to flow easily into the well.

The borewells often either get dried out or yield poorly because the fractures present are either blocked or they are not well connected to the nearby water bodies.

Fig. 8.5 Photograph of the scaled pile model before and after impact of shock wave (shot-1)



The efficiency of the wells gets reduced over time by indicating a low specific capacity or yield. It is economically not feasible and practically impossible to abandon them and start with a new borewell. Clogging up of the fissures in the rock bringing the water due to many reasons which include coagulation of minerals and salts, deposition of dissolved solids, bacterial activity forming an impermeable layer, size of fissure/cracks available, presence of sand or silt in fractures.

8.4.1 Methodology and Preliminary Field Trials

In the present technique, shock wave is produced by sudden rupture of a diaphragm separating the driver and driven sections of the shock tube, thereby creating a shock wave which travels into the driven section. The strong shock wave travelling in the driven tube is directed into the borewell using a 90° bend. As the normal planar shock waves travels through the borewell, the high-pressure gas behind the primary shock wave acts on the inner walls of the borewell uniformly. The pressure pulse behind the shock wave gets amplified after the shock wave enters the water present in the borewell and thus the amplified pressure acts on the inner walls of the borewell containing the water column. This amplified pressure will flush the clogging of the fissures thus enhancing the water flow through these channels thus increasing the yield of the borewell. The high pressure may also enhance the narrow fissures by repeated application of shock waves. Prior to testing, the location and nature of the



Fig. 8.6 A photograph of fully assembled shock tube connected to the borewell



Fig. 8.7 A series of shock waves applied into the borewell (clockwise from top left: shot-1, shot-2, shot-3 and shot-4)

rock formation are observed using a borewell camera, which is designed to give maximum accessibility in the borehole with clear images.

Preliminary tests were carried out on a depleted borewell in the Indian Institute of Science Bangalore campus. Figure 8.6 shows a shock tube assembled in the field and connected to a borewell. The peak overpressure generated from the shock tube test at the end of the driven section is estimated to be around 50 bar pressure. Four repeated shots were performed on the borewell walls. Figure 8.7 shows the picture after a series of shock waves imparted into the borewell. The clogging due to the soil deposits seems to be eroded because of the high-pressure gas flow. This is visible in the borewell camera images captured at 70 ft below the ground surface, as shown in Fig. 8.8.

8.5 Summary

The application of shock waves in different geotechnical problems is discussed in this chapter. Shock waves generated by compressible gas are considered to be promising alternative methods to the conventional hydro-fracking using water. The rock mass

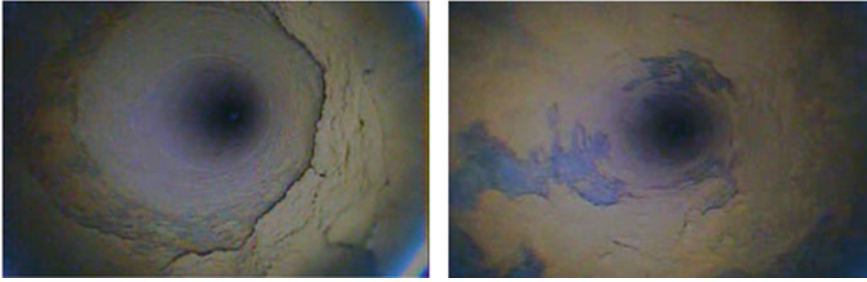


Fig. 8.8 Picture of the borewell taken using a borewell camera at depths of 75 ft (left: before shock wave impact; right: after shock wave impact)

damage parameters are determined from shock tube experiments for various impact load conditions. The fracture pressure for representative brittle rocks is determined from the peak-reflected pressure against the brittle sample. The shock induced damage was assessed by representing the vibration characteristics and crack propagation velocity in terms of incident shock Mach number and peak pressure value. The effect of shock waves on the fractures present in the walls of borewell is investigated using a shock tube. Promising results were observed in the borewell camera, where clogging present in the cracks/fissures were observed to erode.

References

- Jagadeesh G (2008) Fascinating world of shock waves. *Resonance* 13(8):752–767
- Thallak GS (1991) Numerical simulation of hydraulic fracturing in granular media. University of Waterloo
- Thallak GS, Rothenburg L, Dusseault M (1991) Simulation of multiple hydraulic fractures in a discrete element system. American Rock Mechanics Association